NASA/TP–20210000024

Analytical and Numerical Modeling of Sensor Port Acoustics

M.J. Casiano
Marshall Space Flight Center, Huntsville, Alabama

S.R. Fischbach, Editor
Marshall Space Flight Center, Huntsville, Alabama

May 2021

The NASA STI Program…in Profile

Since its founding, NASA has been dedicated to the advancement of aeronautics and space science. The NASA Scientific and Technical Information (STI) Program Office plays a key part in helping NASA maintain this important role.

The NASA STI Program Office is operated by Langley Research Center, the lead center for NASA's scientific and technical information. The NASA STI Program Office provides access to the NASA STI Database, the largest collection of aeronautical and space science STI in the world. The Program Office is also NASA's institutional mechanism for disseminating the results of its research and development activities. These results are published by NASA in the NASA STI Report Series, which includes the following report types:

- TECHNICAL PUBLICATION. Reports of completed research or a major significant phase of research that present the results of NASA programs and include extensive data or theoretical analysis. Includes compilations of significant scientific and technical data and information deemed to be of continuing reference value. NASA's counterpart of peer-reviewed formal professional papers but has less stringent limitations on manuscript length and extent of graphic presentations.

- TECHNICAL MEMORANDUM. Scientific and technical findings that are preliminary or of specialized interest, e.g., quick release reports, working papers, and bibliographies that contain minimal annotation. Does not contain extensive analysis.

- CONTRACTOR REPORT. Scientific and technical findings by NASA-sponsored contractors and grantees.

- CONFERENCE PUBLICATION. Collected papers from scientific and technical conferences, symposia, seminars, or other meetings sponsored or cosponsored by NASA.

- SPECIAL PUBLICATION. Scientific, technical, or historical information from NASA programs, projects, and mission, often concerned with subjects having substantial public interest.

- TECHNICAL TRANSLATION. English-language translations of foreign scientific and technical material pertinent to NASA's mission.

Specialized services that complement the STI Program Office's diverse offerings include creating custom thesauri, building customized databases, organizing and publishing research results…even providing videos.

For more information about the NASA STI Program Office, see the following:

- Access the NASA STI program home page at <http://www.sti.nasa.gov>

- E-mail your question via the Internet to <help@sti.nasa.gov>

- Phone the NASA STI Help Desk at 757–864–9658

- Write to:
  NASA STI Information Desk
  Mail Stop 148
  NASA Langley Research Center
  Hampton, VA 23681–2199, USA

NASA/TP–20210000024

Analytical and Numerical Modeling of Sensor Port Acoustics

M.J. Casiano
Marshall Space Flight Center, Huntsville, Alabama

S.R. Fischbach, Editor
Marshall Space Flight Center, Huntsville, Alabama

National Aeronautics and
Space Administration

Marshall Space Flight Center • Huntsville, Alabama 35812

May 2021

Acknowledgments

I would like to acknowledge my mentors Tom Nesman and Tom Zoladz for encouraging me to study this problem and provide very useful technical insight. My colleague, Sean Fischbach, was also very helpful in reviewing the ideas and providing important insight. He also served as the primary technical peer reviewer of this Technical Publication (TP). Jess Jones, Thein Shi, and Jen-Yi Jong from AI Signal Research, Inc have been very helpful in understanding the signal processing aspects in this TP. I would also like to thank the TP document editor, Susan Burrer, for her effort and attention to detail.

TRADEMARKS

Available from:

NASA STI Information Desk
Mail Stop 148
NASA Langley Research Center
Hampton, VA 23681–2199, USA
757–864–9658

This report is also available in electronic form at
<http://www.sti.nasa.gov>

PREFACE

Acquiring data in rocket engines that are representative of the actual dynamic environment can often be difficult due to a multitude of influences. One source of contamination that is often not considered entirely is the response associated with the acoustic cavity created by a sensor offset. It is common to offset a sensor due to various reasons such as for mounting accessibility, thermal isolation, shock reduction, or prevention of debris impingement. While estimating the natural frequency of the acoustic cavity is straightforward, limited analysis has been described on the determination of the overall frequency response. The sensor port design approach usually attempts to ensure the port is short enough such that the acoustic response is negligible near the frequency of interest, but this requires knowledge of the frequency response and simple rules of thumb are not always guaranteed. Data correction and/or data interpretation are also often desired to account for an unsatisfactory response. The limited response analysis in the literature only offers approximations or neglects important contributions.

A new approach is devised theoretically and computationally that captures the true acoustic response of a sensor port. This Technical Publication (TP) summarizes the acoustics background, the port response theoretical development, and provides comparisons of a port acoustic response using an analytical model and computational acoustics. The effects of nonlinear acoustics and acoustic propagation in liquids are also examined. Additionally, this TP describes the design of a specialized filter using the predicted sensor port response that can be applied to data for correction.

In the author's mind, the work in and of itself is not groundbreaking. However, with an acoustics background and some applied mathematics, practical solutions to engineering problems can be obtained. It seemed appropriate to start the TP out with the usual sensor port design philosophy. The TP provides an added twist to the usual sensor port design approach and develops a variation that is more direct and practical. Following the design methodology, a sensor port frequency response theoretical model is developed. The analytical theory simply comes down to appropriately merging three principal features necessary to explain the physics of acoustics in sensor ports: the acoustic framework, the thermoviscous acoustics, and the radiation acoustics. Next, a simple yet powerful methodology that takes advantage of the deterministic nature of numerical simulations is described. At the simplest view, the numerical analysis compares an acoustic analysis with a sensor port to an acoustic analysis without a port. The additional value of the numerical model is also that it can be extended in any number of ways to incorporate more complex physics such as flow or nonlinear effects. Lastly, while an analyst or engineer must be judicious when considering correcting data contaminated by a sensor port resonance, the procedure and examples, that are not quite readily available in literature, are described in this TP. The TP provides all the necessary means to solve and understand sensor port problems.

The work presented in this TP started as a personal project merely to help understand a seemingly simple problem—how to determine the influence of sensor ports on dynamic pressure data. It began when it was observed that the classic lumped acoustic element approach compared very poorly to observations in data. The problem was not revisited again until after the changes made to the Space Launch System launch pad exhaust deflector were examined: a large cavity under the deflector could produce a resonance and affect the hold-down acoustics environment. To understand the overall effect of a large cavity with a large opening, it was necessary to account for radiation acoustics. After this analysis, a comprehensive sensor port theory began to be pieced together, which benefited from the exhaust deflector work. While it was impossible to provide long periods of focused attention to this problem with various other projects and priorities, the work had grown to include a complete acoustic theory and some intensive computational simulations of canonical problems.

TABLE OF CONTENTS

TABLE OF CONTENTS (Continued)

LIST OF FIGURES

LIST OF FIGURES (Continued)

LIST OF FIGURES (Continued)

LIST OF TABLES

LIST OF ACRONYMS

BDF	backward differentiation formula (solver)
BL	boundary layer
CFD	computational fluid dynamics
EE	English Engineering Units
FFT	fast Fourier transform
IF	instantaneous frequency
PML	perfectly matched layer
PSD	power spectral density
SDOF	single degree of freedom
TF	transfer function
TP	Technical Publication

NOMENCLATURE

A	area; cross-sectional area at opening; cross-sectional area of piston; amplitude
a	acceleration, variable
a_i	imaginary part of $\vec{a}$
a_r	real part of $\vec{a}$
$\vec{a}$	complex vector
B/A	parameter of nonlinearity
b	variable
b_i	imaginary part of $\vec{b}$
b_r	real part of $\vec{b}$
$\vec{b}$	complex vector
C	compliance
C_p	specific heat at constant pressure
C'	compliance per unit length
c_{eff}	effective phase speed
c_p	phase speed
$c_{p,\mathrm{BL}}$	phase speed for thermoviscous boundary layer absorption (exact)
$c_{p,\mathrm{BL,series}}$	phase speed for thermoviscous boundary layer absorption (exact with first-order series approximation)
$c_{p,c}$	phase speed (classical form)
$c_{p,\mathrm{rad}}$	phase speed for the radiation mechanism

NOMENCLATURE (Continued)

$c_{p,\mathrm{th}}$	phase speed for intrinsic thermal absorption
$c_{p,\mathrm{v}}$	phase speed for intrinsic viscous absorption
$c_{p,\mu\kappa}$	phase speed for thermoviscous boundary layer absorption (traditional)
$\overline{c}$	ambient speed of sound
D	gain for an undamped single-degree-of-freedom system
D_{est}	gain estimate
D_{true}	true gain
d	coordinate transformation of spatial coordinate, $d = L - x$
F	body force per unit mass (volume force)
f	frequency
f_c	center frequency
f_h	higher frequency for mesh parameter
f_i	frequency of interest
f_l	lower frequency for mesh parameter
f_n	natural frequency
$\hat{f}$	complex force
f'	oscillatory force
f'_p	externally applied force
f'_r	reaction force
g_c	constant of proportionality
H	pressure transfer function; specific enthalpy

NOMENCLATURE (Continued)

H_1	first-order Struve function
h	first layer element thickness
h_h	first layer element thickness for higher frequency
h_l	first layer element thickness for lower frequency
$\mathbf{I}$	identity tensor
I_{den}	imaginary part of the radicand in the denominator of $\hat{k}_{\mathrm{BL}}$
i	imaginary unit; $-1 = i^2$
$\Im$	imaginary part
J_1	first-order Bessel function of the first kind
k	wave number; thermal conductivity
$\hat{k}$	complex wave number
$\hat{k}_{\mathrm{BL}}$	complex wave number for thermoviscous boundary layer absorption (exact)
$\hat{k}_{\mathrm{BL,series}}$	complex wave number for the thermoviscous boundary layer absorption (exact with first-order series approximation)
L	length; total cylinder length; characteristic length; inertance
L_{BL}	length of boundary layer mesh
$L_{h,\mathrm{BL}}$	length of boundary layer mesh for higher frequency
L_i	design length
$L_{l,\mathrm{BL}}$	length of boundary layer mesh for lower frequency
L_T	total geometric length
L'	effective length; inertance per unit length
l	length (lowercase to distinguish from inertance)

NOMENCLATURE (Continued)

M	frequency multiplication factor
m	diaphragm mass
m_{eff}	effective mass
m_{rad}	radiation mass; added mass (in piston model)
$\dot{m}$	mass flow rate
$\dot{m}'$	unsteady mass flow rate
n	number of line segments; number of layer elements
n_h	number of layer elements for higher frequency
n_l	number of layer elements for lower frequency
P_0	ambient pressure (COMSOL)
Pr	Prandtl number
$\bar{P}$	pressure amplitude
$\bar{P}_+$	outgoing wave pressure amplitude
$\bar{P}_-$	incoming wave pressure amplitude
$\bar{P}_{L+}$	incident wave pressure amplitude
$\bar{P}_{L-}$	reflected wave pressure amplitude
p	pressure; unsteady pressure (COMSOL)
p_D	downstream pressure
p_U	upstream pressure
$\hat{p}$	complex total acoustic pressure
$\hat{p}_{\text{back}}$	complex total acoustic pressure at port back (COMSOL)

NOMENCLATURE (Continued)

$\hat{p}_D$	downstream complex pressure
$\hat{p}_{\text{in}}$	input complex pressure
$\hat{p}_{\text{inlet}}$	complex total acoustic pressure at port inlet (COMSOL)
$\hat{p}_{\text{out}}$	output complex pressure
$\hat{p}_U$	upstream complex pressure
p'	acoustic pressure (oscillatory pressure)
$\tilde{p}$	spatial component of acoustic pressure
Q	internal heat generation
Q_p	thermoviscous pressure work
$\bar{Q}$	volume velocity amplitude
$\bar{Q}_+$	outgoing wave volume velocity amplitude
$\bar{Q}_-$	incoming wave volume velocity amplitude
q	conductive heat flux
q_D	downstream volume velocity
q_U	upstream volume velocity
$\hat{q}$	complex volume velocity
q'	oscillatory volume velocity
$\tilde{q}$	spatial component of volume velocity
R	radius at opening; port radius; piston radius; resistance
R_1	piston resistance function
R_{den}	real part of the radicand in the denominator of $\hat{k}_{\text{BL}}$

NOMENCLATURE (Continued)

$R_{L,p/\dot{m}}$	linearized resistance in pressure-mass flow rate form
$R_{L,p/q}$	linearized acoustic resistance (pressure-volume velocity form)
$R_{L,p/u}$	linearized resistance in pressure-velocity form
R'	resistance per unit length
$\breve{R}_m$	diaphragm mechanical resistance
$\breve{R}_{\mathrm{rad}}$	radiation resistance
$\Re$	real part
S	surface; layer stretching factor
S_h	layer stretching factor for higher frequency
S_l	layer stretching factor for lower frequency
s	diaphragm stiffness
T	temperature; transpose notation
T_0	ambient temperature (COMSOL)
t	time
U	specific internal energy
u	velocity
u_m	velocity magnitude
$\bar{u}_{\mathrm{piston}}$	piston velocity amplitude
u_x	normal component of velocity
$\hat{u}$	complex velocity
u'	particle velocity (oscillatory velocity)

NOMENCLATURE (Continued)

u'_x	normal component of particle velocity
$\overline{u}_x$	normal component of mean velocity
v	value; specific volume
v_{approx}	approximate value
v_{exact}	exact value
X	pressure amplification factor; infinite series term
X_1	piston reactance function
$\widehat{X}$	amplification factor of the inverse transfer function
$\breve{X}_{\text{rad}}$	radiation reactance
x	spatial coordinate; variable
$\hat{x}$	complex variable
y	variable
Z	acoustic impedance
Z_C	characteristic impedance
Z_D	downstream acoustic impedance
Z_{in}	input impedance
Z_R	general termination impedance
Z_U	upstream acoustic impedance
$\breve{Z}$	mechanical impedance
$\breve{Z}_{\text{rad}}$	radiation impedance
z	specific acoustic impedance; radicand in denominator of $\hat{k}_{\text{BL}}$; variable

NOMENCLATURE (Continued)

α	spatial absorption coefficient
α_{BL}	spatial absorption coefficient for thermoviscous boundary layer absorption (exact)
α_c	classical absorption coefficient
α_{eff}	effective spatial absorption coefficient
α_p	isobaric coefficient of volumetric thermal expansion
α_{port}	port effective spatial absorption coefficient
α_{rad}	spatial absorption coefficient for the radiation mechanism
α_{th}	spatial absorption coefficient for intrinsic thermal absorption
α_{v}	spatial absorption coefficient for intrinsic viscous absorption
α_κ	spatial absorption coefficient for thermal boundary layer absorption
α_μ	spatial absorption coefficient for viscous boundary layer absorption
$\alpha_{\mu\kappa}$	spatial absorption coefficient for thermoviscous boundary layer absorption (traditional)
β	phase shift parameter
β_{BL}	phase shift parameter for thermoviscous boundary layer absorption (exact)
$\beta_{\text{BL,series}}$	phase shift parameter for thermoviscous boundary layer absorption (exact with first-order series expansion)
$\tilde{\beta}$	temporal absorption coefficient
$\tilde{\beta}_{\text{rad}}$	temporal absorption coefficient for the radiation mechanism
Γ	gamma function
γ	specific heat ratio; coefficient defined as $1 + B/A$
$\hat{\gamma}$	propagation constant
$\hat{\gamma}_{\text{BL}}$	propagation constant for thermoviscous boundary layer absorption (exact)

NOMENCLATURE (Continued)

$\hat{\gamma}_{\mathrm{BL,series}}$	propagation constant for thermoviscous boundary layer absorption (exact with first-order series approximation)
$\hat{\gamma}_{\mathrm{eff}}$	effective propagation constant
$\hat{\gamma}_{\mathrm{heuristic}}$	propagation constant for thermoviscous boundary layer absorption (heuristic)
$\hat{\gamma}_{\mathrm{rad}}$	propagation constant for the radiation mechanism
$\hat{\gamma}_{\mu\kappa}$	propagation constant for thermoviscous boundary layer absorption (traditional)
ΔL	end correction; effective height
Δx	lumped element length
δ	acoustic boundary layer thickness; percent relative error
δ_h	acoustic boundary layer thickness for higher frequency
δ_l	acoustic boundary layer thickness for lower frequency
δ_{R_1}	percent relative error for piston resistance function
δ_{X_1}	percent relative error for piston reactance function
δ_κ	acoustic thermal boundary layer thickness
δ_μ	acoustic viscous boundary layer thickness
ε	relative error
θ	variable
λ	wavelength
μ	dynamic viscosity
μ_B	bulk viscosity
ρ	density

NOMENCLATURE (Continued)

$\bar{\rho}$	ambient density
$\boldsymbol{\sigma}$	total stress tensor
τ	dummy variable; relaxation time
$\overline{\overline{\boldsymbol{\tau}}}$	viscous stress tensor
ϕ	relative phase; viscous dissipation function; variable
$\widehat{\phi}$	relative phase of the inverse transfer function
ω	angular frequency
ζ	damping ratio

TECHNICAL PUBLICATION

ANALYTICAL AND NUMERICAL MODELING OF SENSOR PORT ACOUSTICS

1. INTRODUCTION

1.1 Background

Acquiring data that are representative of an environment can often be difficult due to a multitude of influences. Unwanted responses can be caused by every component in the measurement system such as those due to the acquisition system electronics, transducer sensing components, and cables. Mains electrical noise may often taint data in a poorly grounded system. Moreover, the sensor transducer component, such as piezoelectric crystals, have a sensitivity to other environments that can also corrupt the data, such as the thermal and vibratory influence on a dynamic pressure device. Careful design of the measurement system is always prudent prior to data collection.

There is another source of contamination that is often not considered entirely, particularly for dynamic pressure sensors. It may not always be possible to install a dynamic pressure sensor so that it is mounted flush with the environment of interest. In addition, it is common to offset the sensor due to various reasons such as for mounting accessibility, thermal isolation, shock reduction, or prevention of debris impingement. This offset, or standoff, creates an acoustic cavity with the sensing device in the back of the cavity. The acoustic cavity is referred to as a sensor port. The sensor port is part of the system being measured, but it is not part of the system that is intended to be measured. While the sensor port may be small, its contribution to the collected data may be very significant. Figure 1 shows generic sensor mounting schemes in the desired configuration and in an offset configuration that produces a sensor port.

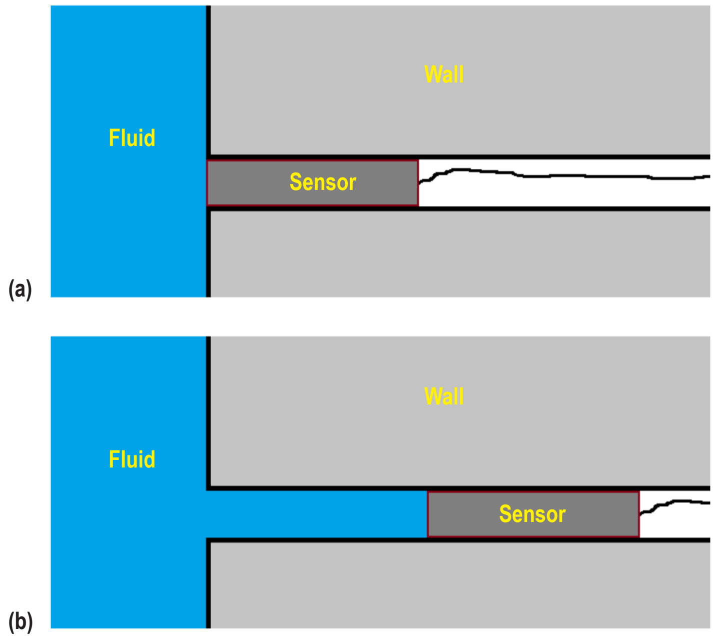

Figure 1. Generic sensor mounting schemes: (a) Desired configuration and (b) offset configuration with sensor port.

While estimating the natural frequency of the acoustic cavity is straightforward, limited analysis has been described on the determination of the overall frequency response. The acoustic resonance within the sensor port produces a frequency-dependent amplification and phase deviation that directly affects the data collected as shown in figure 2. The desired port configuration is usually flush mounted, but acceptable configurations can be close coupled such that frequencies of interest are negligibly affected by the influence of the port.

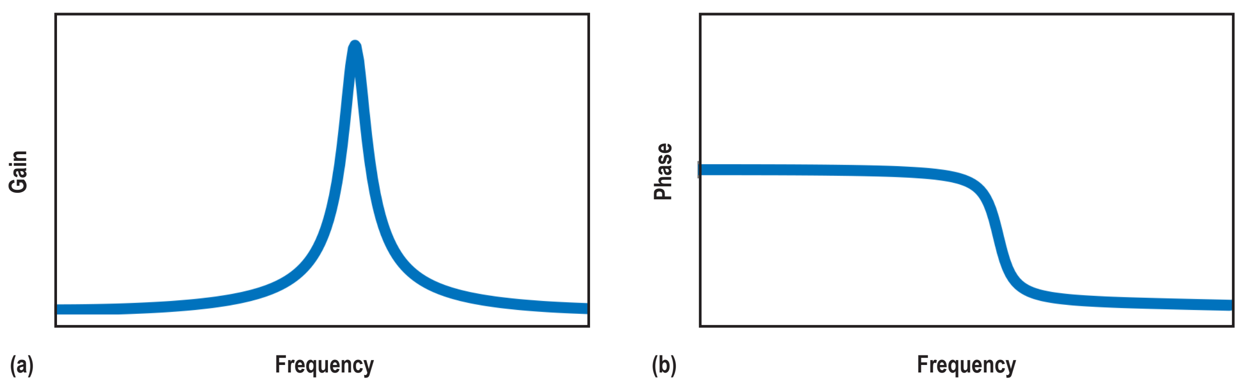

Figure 2. Sensor port acoustic frequency response function: (a) Gain and (b) phase.

The sensor port design approach usually attempts to ensure the port is short enough such that the acoustic response is negligible near the frequency of interest, but this requires knowledge of the frequency response and simple rules of thumb are not always guaranteed. The design estimate using simple calculations may also be very conservative, e.g., where a longer port may be adequate in a configuration with a mounting limitation. Furthermore, it is often desired to understand the frequency response in situations where an undesirable sensor port exists for data correction and/or data interpretation.

The purpose of this Technical Publication (TP) is to provide background, relevant theory, and examples for acoustic response analysis of a sensor port. The goal is to be able to predict the sensor port response and understand what effect the port has on the collected data.

2. ANALYTICAL MODELING

2.1 Background

The primary purpose of analytical modeling is to obtain an accurate solution in an efficient manner. An analytical framework allows for development of tractable solutions that can be applied quickly. Analytical models are true mathematical models because a system is described using mathematical concepts, but are often referred to as engineering models because of their practical usage in brief design cycles. It is very important to understand the constraints and assumptions that are used in the development of an analytical model so that the model is not used outside of the intended scope.

The following sections provide simple guidelines for sensor port design (sec. 2.2), develop an analytical frequency response framework (sec. 2.3), and describe relevant dissipation mechanisms (secs. 2.4 and 2.5).

2.2 Sensor Port Design Guideline

A simplified analysis is normally performed to estimate a frequency range where the sensor port response is considered negligible. This section develops practical forms of the design length that can be determined either by traditional frequency multiplication factors, e.g., 3× to 5× lower than the fundamental natural frequency, or by specification of a flat, useable bandwidth, e.g., no greater than 5% amplification through a frequency of interest.

A sensor port can be approximated as a cylindrical acoustic waveguide with a single effective diameter and a total length.[1, chp. 12; 2, chp. 9] The wave equation can be solved in this domain with appropriate boundary conditions. At the rigid boundaries, a closed condition is applied where the normal component of particle velocity is zero. This applies everywhere except at the sensor port opening. At the sensor port opening, the simplest approach is to apply a pressure release boundary condition which constrains the pressure oscillation to zero.[1, pp. 134–137] For a cylindrical cavity, the natural frequency and shape of the mode can then be predicted. The longitudinal modes are the relevant modes that produce amplification on the pressure sensor diaphragm. The fundamental longitudinal mode shape is that of a quarter wave and the natural frequency is given as equation (1):

$$f_n = \frac{\overline{c}}{4L} \ , \tag{1}$$

where f_n is the natural frequency, $\overline{c}$ is the speed of sound, and L is the total cylinder length.[1, pp. 34, 137; 3, p. 343]

A correction is made because the open boundary condition is not truly a pressure release boundary. A general impedance exists at this boundary due to the local pressure radiating from the end into the fluid outside the port. An end correction for a flanged tube can be derived (sec. 2.5), where a flanged tube represents a tube that opens through a plane baffle of infinite extent.[4, p. 381] Equation (2), a low-frequency estimate, can be derived by considering first-order terms (sec. 2.5.1):

$$\Delta L \approx \frac{8R}{3\pi} \,, \tag{2}$$

where ΔL is an end correction and R is the radius at the opening.[1, pp. 151–152; 2, pp. 272–274]

The quarter-wave natural frequency of a flanged sensor port can then be estimated using equation (3) where the effective length is given by $L' = L + \Delta L$:

$$f_n = \frac{\bar{c}}{4L'} \,. \tag{3}$$

This is the traditional form used in identifying the fundamental resonance frequency of a flanged quarter-wave resonator.

Given the quarter-wave natural frequency, rules of thumb vary for predicting an acceptable bandwidth. Criteria for many applications range between 3× to 5× lower than the natural frequency and are based on the amount of gain response (or pressure amplification) that is acceptable, e.g., a 3× factor is recommended in references 5, p. 464 and 6, p. 63 for combustion stability. The ratio, $M = f_n / f_i$, used commonly as criteria for sensor port design, can be referred to as the frequency multiplication factor. It is described as the ratio of the natural frequency to the maximum frequency of interest, f_i. The frequency of interest is required to be less than the fundamental resonance so $M > 1$. To generate estimates for the gain and error associated with a particular frequency multiplication factor, the acoustics in the sensor port can be surmised to follow a forced time-harmonic oscillator response of a single-degree-of-freedom (SDOF) system.

The pressure gain associated with the sensor port can be roughly estimated by considering an undamped SDOF solution. This approximation provides a reasonable estimate; however, the undamped SDOF response may not necessarily produce the worst-case amplification over the entire frequency bandwidth. The gain for an undamped SDOF, D, given in equation (4), provides the magnification at the maximum frequence of interest:

$$D = \frac{1}{1 - \left(f_i / f_n\right)^2} = \frac{M^2}{M^2 - 1} \,. \tag{4}$$

It can also be written in terms of the frequency multiplication factor where values close to 1 are obviously not applicable as the gain approaches infinity for an undamped system.

This undamped gain is classically used as a guide to represent the upper bound of the pressure amplification factor. However, the acceptable range defining a flat, useable bandwidth is ultimately determined by the analyst or end user. To aid with this definition, the relative error, ε, associated with the undamped response gain can be calculated considering that the ideal gain for a flush-mounted sensor, or true gain, is equal to a value of 1 (no amplification):

$$\varepsilon = \left| \frac{D_{\text{true}} - D_{\text{est}}}{D_{\text{true}}} \right| = \left| 1 - D_{\text{est}} \right| \ . \tag{5}$$

Using equation (4) for the gain estimate, the gain error in equation (5) is given simply as equation (6):

$$\varepsilon = D - 1 = \frac{1}{M^2 - 1} \ . \tag{6}$$

For the example rule of thumb described earlier, the error can simply be calculated considering that the system behaves as an undamped SDOF. Equation (6) can be used to show that for $M = 3$, the error is 12.5%, and for $M = 5$, the error is 4.2%. As another example, it is often established that the gain error is within a certain percentage. In the example where a flat, useable bandwidth is specified to be within 5%, the frequency multiplication factor can be calculated to be $M = 4.6$; therefore, the maximum frequency of interest must be approximately 4.6× lower than the natural frequency for the response to be within this error.

These examples can be used as design guidance, and in some cases, the port length may need to be shortened so that this criterion is met. Using equation (3) and the multiplication factor, a design length, L_i, is derived in equation (7):

$$L_i \le \frac{\bar{c}}{4 f_i M} - \frac{8R}{3\pi} \ . \tag{7}$$

The inequality denotes that smaller lengths are acceptable.

The design length can also be described in a more useful form by incorporating a specified flat, useable bandwidth. This specification would include the gain relative error and maximum frequency of interest. Substituting equation (6) into equation (7) produces this practical formula as equation (8):

$$L_i \le \sqrt{\frac{\varepsilon}{\varepsilon + 1}} \cdot \frac{\bar{c}}{4 f_i} - \frac{8R}{3\pi} \ . \tag{8}$$

While these relationships provide a guide for a sensor port design, they do not produce a representative frequency response. The simple design guide may also break down in many cases; e.g., the undamped SDOF model may not apply over the bandwidth of interest or the guide may be inaccurate for a complex multiport design. Also, the port design may not be practical to construct, and a more accurate estimate may provide a viable standoff length. In addition, accurate estimates for correcting data with port resonances at various frequencies may also be desired.

2.3 Sensor Port Frequency Response Model—Theory

The goal is to be able to predict an accurate sensor port response by modeling the port acoustic cavity frequency response. As an improvement to the undamped SDOF model used classically, a comprehensive theory is developed for obtaining the acoustic frequency response of a sensor port. There are three critical advancements necessary to extend classic acoustic theory into a practical sensor port frequency response model: (1) Application of a distributed acoustics model rather than the lumped acoustic element approach, which relies on the long wavelength limit, (2) development of an exact solution to the thermoviscous wave equation applicable to the framework, and (3) reformulation of acoustic radiation impedance as an acoustic propagation constant. The entire development is discussed along with these theoretical improvements in the following subsections.

To obtain the frequency response, the complex pressure ratio is explored. This pressure transfer function or complex pressure ratio is an important quantity, which measures the complex pressure of the output to the input:

$$H = \frac{\hat{p}_{\text{out}}}{\hat{p}_{\text{in}}} \; . \tag{9}$$

In the frequency domain, two important parameters provide information about the response: the pressure amplification factor, X, and relative phase, ϕ. Both these parameters can be obtained from the complex pressure ratio and are functions of frequency.

A pressure amplification factor is also referred to as an amplification factor or gain. The terminology is borrowed from electronics and is a measure of amplitude increase of a signal from the input to the output. The pressure amplification factor[1, p. 155; 2, p. 285] of a resonator is the ratio of the acoustic pressure amplitude at the back of the sensor port, i.e., the measurement location, to the acoustic pressure amplitude of an incident wave on the sensor port, i.e., without influence of the port. The relative phase is simply the deviation in phase angle between the pressure at the back of the sensor port and the incident pressure wave on the sensor port. For both analytical and numerical modeling, the influence of the port must be appropriately handled as not to obscure the incident pressure field.

While any reference frame is acceptable, it is useful to think of a propagating wave moving from the back of the port and moving towards the opening, especially when the concept of input impedance is introduced in section 3.3.2 and discussed further in appendix F. In the following theory, the output is the upstream end defined at the sensor port back (at the measurement location). In a 1-D sense, the input of the sensor port is represented somewhat abstractly as the location downstream of the end correction region. The effects of the end correction region can be captured appropriately by incorporating the physical influences using a transfer line model with an independent line segment.

These radiation effects will be discussed in detail later and will become clearer in sections 2.3.3 and 2.5. The transfer line model will be discussed as the distributed acoustic framework in section 2.3.1.

Using subscript U for the upstream boundary and subscript D for the downstream boundary, the modulus and argument of the complex pressure ratio are written as equations (10) and (11), referred to as the pressure amplification factor and relative phase, respectively:

$$X(f) = \left| \frac{\hat{p}_U}{\hat{p}_D} \right| \tag{10}$$

and

$$\phi(f) = \angle\left(\frac{\hat{p}_U}{\hat{p}_D} \right) . \tag{11}$$

The upstream and downstream transfer line nomenclature are adopted from reference 7. These equations together will be referred to as the sensor port response.

2.3.1 Theoretical Framework

Before deriving pressure transfer equation relationships that provide a complex pressure ratio, the theoretical framework used for modeling dissipation is discussed. There are many different forms of dissipation that may apply to an acoustic system. Examples include dissipation due to thermal heat conduction and viscous absorption in a fluid, thermal heat conduction and viscous absorption at a boundary, molecular relaxation, and other flow or acoustic-induced dissipation mechanisms. The physical process of each mechanism is different; therefore, the governing equations differ. However, each mechanism is described by a separate lossy wave equation, and their solution form remains identical. Equation (12) represents the wave equation pressure solution where the acoustic pressure, p', [1, p. 46] is a time-harmonic signal. The acoustic pressure is also referred to as oscillatory pressure.

$$p' = \overline{P} e^{i\omega t} e^{-i\hat{k}x} = \overline{P} e^{i\omega t} e^{-\hat{\gamma}x} . \tag{12}$$

It is described in terms of either complex wave number or propagation constant, which characterize the propagation losses of an individual mechanism.[1, pp. 299, 302; 2, p. 212; 7, p. 291; 8, p. 4] Note the hat notation shown previously is dropped for the complex pressure in the remaining part of this TP. Also note that in this TP, k without the hat is the wave number, $k = \omega/\overline{c}$, and γ without the hat is the specific heat ratio.

The relationship between propagation constant and complex wave number is given by $\hat{\gamma} = i\hat{k}$. The complex wave number and complex propagation constant for an outgoing wave moving in the positive direction is given as equations (13) and (14), respectively, shown with a real and imaginary part:[1, p. 299; 2, p. 212; 7, p. 291; 8 p. 4]

$$\hat{k}_+ = \beta - i\alpha \tag{13}$$

and

$$\hat{\gamma}_+ = \alpha + i\beta. \tag{14}$$

The complex propagation constant is preferred in the following framework; however, the complex wave number is convenient in some cases. The propagation constant is complex and characterizes the absorption and dispersion associated with waves propagating through a dissipative fluid.

The incoming wave is given by the negative of equations (13) and (14); however, for discussion, the outgoing wave is examined. Equation (12) can then be written as an outgoing pressure wave, expanded as equation (15):[1, p. 302; 2, p. 212; 7, p. 291]

$$p' = \bar{P}_+ e^{i\omega t} e^{-(\alpha + i\beta)x} = \bar{P}_+ e^{i\omega t} e^{-\alpha x} e^{-i\beta x} \quad . \tag{15}$$

The parameter α is the spatial absorption coefficient, since the amplitude decays spatially by $e^{-\alpha x}$ as observed in equation (15). The parameter β is a phase shift parameter (confusingly, it is sometimes referred to as the propagation constant) and is related to the phase speed, c_p, by equation (16):

$$c_p = \frac{\omega}{\beta} \quad . \tag{16}$$

The solution to the lossy wave equations given as equation (12) or expanded as equation (15) show that the pressure represents an attenuating pressure oscillation with the wave propagation speed given by the phase speed. Because the solution to lossy wave equations describing different physical processes can all be represented using the same functional form, it is possible to describe a propagation constant that is specific for each physical mechanism. Therefore, the phase speed and spatial absorption coefficient can also be described for a specific dissipation mechanism.

The Helmholtz equation represents the time-independent form of the wave equation and can be used as a consistent theoretical framework that satisfies the solution form of equation (15). This framework is useful to obtain sensor port relationships. It is also useful to represent the solution in terms of impedance, which is a function of frequency, since the desire is to obtain the frequency response.

An acoustical-electrical analogy, applicable to acoustic pipe systems and waveguides,[2, pp. 272, 287-288] can be used in the model development and formulated in terms of impedance. Impedance can be described by the ratio of an effort variable to a corresponding flow variable.[1, p. 46] The appropriate acoustic effort and flow variables in the impedance formulation are obtained by comparison to an electrical system where the acoustic variables must have a mathematical form identical to the electric variables. Commonly, the effort and flow variables are related in such a way that when multiplied together have units of power. For example in the electrical system, the effort variable is voltage and the flow variable is current and when multiplied gives electrical power. For the analogy to hold in an acoustic system, the effort variable is pressure and the flow variable is volumetric flow rate (also referred to as volume velocity) and when multiplied gives sound power.[1, pp. 48-51] Acoustic impedance is therefore defined as the quotient of complex pressure to complex volume velocity.[2, p. 286] Volume velocity, q, is the area multiplied by velocity, i.e., $q=A\cdot u$. The pressure and volume velocity are the most convenient variables in an acoustic waveguide impedance framework[2, p. 288] and will be used in the development of the sensor port model. Impedance can be represented in numerous ways, however, three are relatively common in acoustics.[1, p. 47; 2, p. 286]

The acoustic impedance is given as equation (17):

$$Z=\frac{\hat{p}}{\hat{q}}=\frac{1}{A}\frac{\hat{p}}{\hat{u}} \ . \tag{17}$$

Throughout this TP, 'impedance' will refer to the acoustic impedance unless otherwise noted. As noted, it is the ratio of complex pressure to complex volume velocity.

The specific acoustic impedance is given as equation (18); it is the ratio of complex pressure to complex velocity:

$$z=\frac{\hat{p}}{\hat{u}} \ . \tag{18}$$

The mechanical impedance is given as equation (19); it is the ratio of complex force to complex velocity:

$$\breve{Z}=\frac{\hat{f}}{\hat{u}}=A\frac{\hat{p}}{\hat{u}} \ . \tag{19}$$

A 'pipe' section is used to develop a formulation that can be applied to a sensor port, schematically shown in figure 3. A parameter referred to as the characteristic impedance, Z_C, represents the impedance associated with a wave propagating in one direction in the absence of reflections. The characteristic impedance and propagation constant are dependent on the fluid properties and pipe geometry. The arrow denotes the positive direction of flow, resulting in the upstream and downstream nomenclature, however note there is no mean flow.

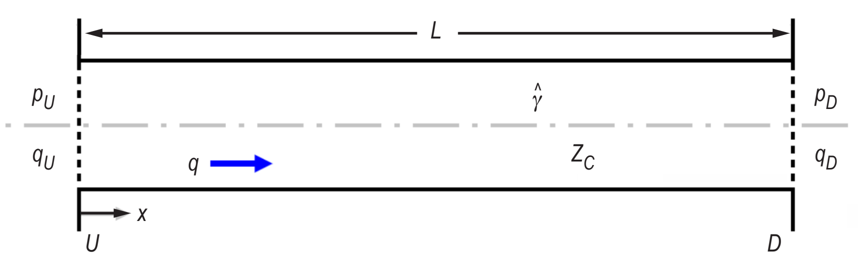

Figure 3. Pipe section schematic.

The equations of motion are described using the momentum equations, continuity equation, and equation of state.[1, pp. 27–39, 299; 7, pp. 289–293] By linearizing and applying a separation of variables technique, the governing equations can be split into a spatially dependent and temporally dependent form.[7, p. 291] The spatially dependent form is the Helmholtz equation and will be examined carefully here. Pressure and volume velocity are used in the formulation to remain consistent with the acoustical-electrical analogy. Applying the upstream boundary conditions to the pipe section gives the spatial component of acoustic pressure and volume velocity, $\tilde{p}$ and $\tilde{q}$, respectively, and can be described as equations (20) and (21):[7, pp. 289–293]

$$\tilde{p}(x) = p_U \cosh(\hat{\gamma}x) - Z_C q_U \sinh(\hat{\gamma}x) \tag{20}$$

and

$$\tilde{q}(x) = -\frac{p_U}{Z_C}\sinh\left(\hat{\gamma}x\right) + q_U \cosh(\hat{\gamma}x) \ . \tag{21}$$

These distributed solutions are referred to as transfer equations and are the basis for distributed element models. Applying this distributed element model to a sensor port is necessary to correctly predict the acoustic frequency response, since the classic lumped acoustic element approach only applies in the long wavelength limit.[2, p. 283]

Equations (20) and (21) are developed in appendix A and it is shown that the framework applies to any of the lossy wave equations. Typically, these may be seen in literature written in terms of exponential functions; however, hyperbolic trigonometric functions simplify the solution form and provide a means of convenient manipulation. Impedance is a complex, time-independent quantity and, spatially, can be represented in the 1-D domain as $Z(x) = \tilde{p}(x) / \tilde{q}(x)$.[1, pp. 46–47; 7, p. 293] It can be obtained at any given point using equations (20) and (21).

The characteristic impedance of the fluid for an outgoing wave, written in terms of the propagation constant, can be determined by calculating the ratio given in equation (22) for an outgoing wave.[1, pp. 38–39; 2, p. 126; 7, pp. 291–292] The relationship can be derived by examining only the outgoing wave, using the ratio of pressure, equation (12), to the analogous form for volume velocity. The characteristic impedance of the fluid is given as equation (22) and also described in appendix A:

$$Z_C \equiv \left(\frac{p'}{q'}\right)_+ = -\frac{\bar{\rho}\bar{c}^2\hat{\gamma}}{A\omega} i \ . \tag{22}$$

One particular pair of transfer equations is very useful in manipulating sensor port relationships. By substituting $x = L$ into equations (20) and (21), where $\tilde{p}(L) = p_D$ and $\tilde{q}(L) = q_D$, and solving for the upstream conditions, the following relationships are obtained:

$$p_U = p_D \cosh(\hat{\gamma}L) + Z_C q_D \sinh(\hat{\gamma}L) \tag{23}$$

and

$$q_U = \frac{p_D}{Z_C}\sinh(\hat{\gamma}L) + q_D\cosh(\hat{\gamma}L) \ . \tag{24}$$

Two very useful impedance relationships can also be written. The upstream impedance, equation (25), can be obtained by first dividing equation (23) by equation (24) and then multiplying the numerator and denominator each by $1/\left(q_D\cosh(\hat{\gamma}L)\right)$ to simplify:

$$Z_U = \frac{Z_D + Z_C\tanh(\hat{\gamma}L)}{1+\dfrac{Z_D}{Z_C}\tanh(\hat{\gamma}L)} \ . \tag{25}$$

The downstream impedance, equation (26), can also be written by rearranging equation (25):

$$Z_D = \frac{Z_U - Z_C\tanh(\hat{\gamma}L)}{1-\dfrac{Z_U}{Z_C}\tanh(\hat{\gamma}L)} \ . \tag{26}$$

The distributed solutions and relationships given in this section are used as a general acoustic framework to describe the propagation of waves within a sensor port. The propagation constants that are used in the sensor port model will be detailed following the line models discussion.

As a note, one common approach in acoustics is to model a system using the long wavelength limit where, generally, a characteristic length is much shorter than the wavelength, $L \ll \lambda$.[1, pp. 144–156; 2, pp. 283–287] However, the shortcomings using this approximation are extreme except in the low frequency limit and should not be used in sensor port analysis. The lumped acoustic element approach uses this procedure to combine the overall impedance in the low-frequency limit, usually approximated to first order, to produce an effective mass, effective stiffness, and effective resistance. This practice also excludes the spatial effects.[2, p. 283] A distributed element system effectively considers the mass, stiffness, and resistance per unit of length and is accurate at low and high frequency.

2.3.2 Sensor Port Frequency Response Model—One-Line Model

This section develops the analytical expressions for a one-line model using the schematic shown in figure 4.[9] The one-line model is most applicable to very long sensor ports with a constant diameter and single set of fluid properties, where the end correction is negligible. It is applicable in modeling thermoviscous effects and is not general enough to account for radiation acoustics. Notice the upstream end is a closed boundary; this would represent the location of the sensor diaphragm. For any sensor port analysis, it is recommended that at least a two-line model be applied so that both thermoviscous effects and radiation acoustics can be incorporated. In the one-line port model, the propagation constant is a function of the thermoviscous spatial absorption coefficient. This model is primarily included for completeness, since radiation effects cannot be incorporated into the model.

Also, note that since, in general, there will be multiple-line models making up a complex sensor port, a numbering scheme is used instead of the upstream and downstream notation.

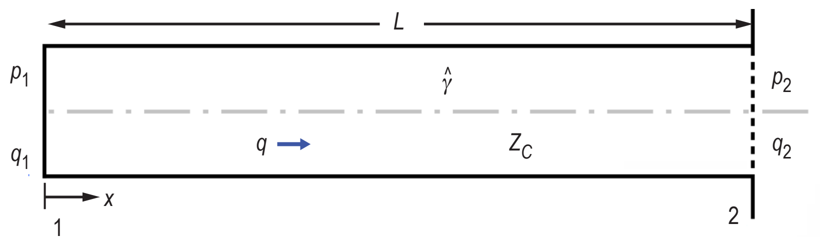

Figure 4. Pipe section schematic for one-line sensor port.

The complex pressure ratio of a one-line model can be derived simply. Using equation (23) as a general line segment relationship, the formula for a complex pressure ratio of a pipe section is obtained by dividing by the downstream pressure, p_2, shown as equation (27):

$$\frac{p_1}{p_2} = \cosh(\hat{\gamma}L) + \frac{Z_C}{Z_2}\sinh(\hat{\gamma}L) \ . \tag{27}$$

For a closed boundary, the location 1 impedance is infinite. By applying this limit to equation (26), the location 2 boundary impedance simplifies to equation (28):

$$\lim_{Z_1 \to \infty} Z_2 = -Z_C \cdot \coth(\hat{\gamma}L) \ . \tag{28}$$

Substituting equation (28) into equation (27) results in the complex pressure ratio for a one-line model and simplifies to equation (29):

$$\frac{p_1}{p_2} = \operatorname{sech}(\hat{\gamma}L) \ . \tag{29}$$

Now that the complex pressure ratio is obtained, equations (10) and (11) can be used to obtain the pressure amplification factor and relative phase, given as equations (30) and (31), respectively, denoted using the real part, $\Re$, and imaginary part, $\Im$:

$$X(f) = \left|\operatorname{sech}(\hat{\gamma}L)\right| = \sqrt{\Im\left(\operatorname{sech}(\hat{\gamma}L)\right)^2 + \Re\left(\operatorname{sech}(\hat{\gamma}L)\right)^2} \tag{30}$$

and

$$\phi(f) = \angle\left(\operatorname{sech}(\hat{\gamma}L)\right) = \tan 2^{-1}\left(\Im\left(\operatorname{sech}(\hat{\gamma}L)\right), \Re\left(\operatorname{sech}(\hat{\gamma}L)\right)\right) \ . \tag{31}$$

The function $\tan 2^{-1}(y,x)$ is the two-argument arctangent (also called the four-quadrant inverse tangent) and can also be represented mathematically as the argument function, $\arg(x+iy)$.

For a one-line port model, the pressure amplification and relative phase can be described by plotting these equations as a function of frequency.

2.3.3 Sensor Port Frequency Response Model—Two-Line Model

This section develops the analytical expressions for a two-line model. The two-line model is general enough to consider damping effects due to thermoviscous acoustics and acoustic radiation out of the port, for a constant diameter port and single set of fluid properties. In this model, a propagation constant would be defined for thermoviscous effects and another propagation constant for acoustic radiation. A schematic drawing with two equal-diameter segments is shown in figure 5, now with a midstream location separating the line segments. Line segment A will represent the actual geometric port length and thermoviscous effects and line segment B will represent the end correction for acoustic radiation. It should be emphasized that a two-line model represents a constant diameter port, where the first line segment is associated with the constant diameter and a single set of fluid properties, and the second line segment is associated with the end correction.

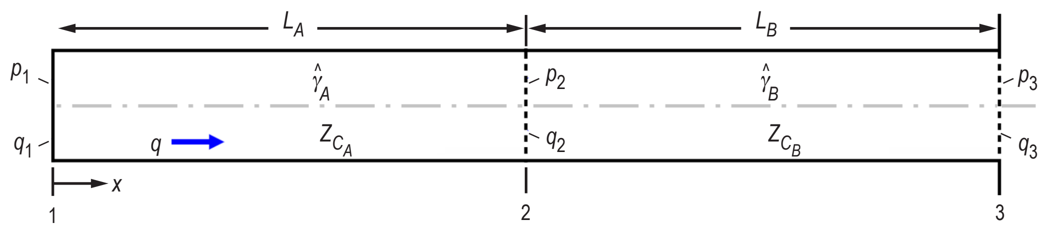

Figure 5. Pipe section schematic for two-line sensor port.

The two-line model expressions can be derived by first examining just pipe section A using equation (23), but dividing through by the far downstream pressure, p_3, resulting in equation (32):

$$\frac{p_1}{p_3} = \frac{p_2}{p_3}\cosh\left(\hat{\gamma}_{\mathrm{A}} L_{\mathrm{A}}\right) + \frac{q_2}{p_3} Z_{C,\mathrm{A}} \sinh\left(\hat{\gamma}_{\mathrm{A}} L_{\mathrm{A}}\right) . \tag{32}$$

Now expressions are only needed for p_2/p_3 and for q_2/p_3. The former can be found simply by examining pipe section B using equation (23) and dividing through by p_3, resulting in equation (33):

$$\frac{p_2}{p_3} = \cosh\left(\hat{\gamma}_{\mathrm{B}} L_{\mathrm{B}}\right) + \frac{Z_{C,\mathrm{B}}}{Z_3} \sinh\left(\hat{\gamma}_{\mathrm{B}} L_{\mathrm{B}}\right) . \tag{33}$$

The latter can be found simply by also examining pipe section B using equation (24) and dividing through by p_3, resulting in equation (34):

$$\frac{q_2}{p_3} = \frac{1}{Z_{C,\mathrm{B}}} \sinh\left(\hat{\gamma}_\mathrm{B} L_\mathrm{B}\right) + \frac{1}{Z_3} \cosh\left(\hat{\gamma}_\mathrm{B} L_\mathrm{B}\right) \ . \tag{34}$$

The impedance at location 3 in equations (33) and (34) is the only remaining unknown variable. This can be found from the boundary condition at location 1. Similar to the procedure in the one-line model, pipe section A is examined using equation (26) and the closed boundary impedance limit is applied, $Z_1 \to \infty$, resulting in equation (35) at location 2:

$$\lim_{Z_1 \to \infty} Z_2 = -Z_{C,\mathrm{A}} \cdot \coth\left(\hat{\gamma}_\mathrm{A} L_\mathrm{A}\right) \ . \tag{35}$$

Subsequently, pipe section B can be examined also using equation (26) with the substitution of equation (35) for Z_2. This results in a cumbersome impedance relationship at location 3; however, there are no longer any remaining unknown variables:

$$Z_3 = \frac{-\dfrac{Z_{C,\mathrm{A}}}{\tanh\left(\hat{\gamma}_\mathrm{A} L_\mathrm{A}\right)} - Z_{C,\mathrm{B}} \tanh\left(\hat{\gamma}_\mathrm{B} L_\mathrm{B}\right)}{1 + \dfrac{Z_{C,\mathrm{A}}}{Z_{C,\mathrm{B}}} \dfrac{\tanh\left(\hat{\gamma}_\mathrm{B} L_\mathrm{B}\right)}{\tanh\left(\hat{\gamma}_\mathrm{A} L_\mathrm{A}\right)}} \ . \tag{36}$$

Equations (33), (34), and (36) can now be substituted into equation (32). After a fair amount of manipulation and simplification, a relationship can be found for p_1/p_3. Equation (37) is the complex pressure ratio for a two-line model:

$$\frac{p_1}{p_3} = \left(\cosh\left(\hat{\gamma}_\mathrm{A} L_\mathrm{A}\right) \cosh\left(\hat{\gamma}_\mathrm{B} L_\mathrm{B}\right) + \frac{Z_{C,\mathrm{B}}}{Z_{C,\mathrm{A}}} \sinh\left(\hat{\gamma}_\mathrm{A} L_\mathrm{A}\right) \sinh\left(\hat{\gamma}_\mathrm{B} L_\mathrm{B}\right) \right)^{-1} \ . \tag{37}$$

For a two-line model, the pressure amplification factor and relative phase can be described by applying equations (10) and (11) to equation (37). This formula is an important relationship and it should be emphasized that it is the simplest form possible needed to represent both thermoviscous effects and radiation acoustics for a constant diameter sensor port, both of which are necessary to produce an accurate sensor port acoustic response. This model will be used for comparisons in the numerical analysis section, section 3.3.4.

2.3.4 Sensor Port Frequency Response Model—Multiline Model

To account for damping effects due to thermoviscous acoustics, acoustic radiation from the port, and a sensor port with a single diameter change, a 3-line model must be developed. Note also that each line segment can consider separate fluid properties. Using a similar procedure as described in the previous subsection, the complex pressure ratio is found as equation (38):

$$\frac{p_1}{p_4}=\left(\begin{array}{l}\left(\cosh\left(\hat{\gamma}_{\mathrm{C}}L_{\mathrm{C}}\right)\cosh\left(\hat{\gamma}_{\mathrm{B}}L_{\mathrm{B}}\right)+\dfrac{Z_{C,\mathrm{C}}}{Z_{C,\mathrm{B}}}\sinh\left(\hat{\gamma}_{\mathrm{C}}L_{\mathrm{C}}\right)\sinh\left(\hat{\gamma}_{\mathrm{B}}L_{\mathrm{B}}\right)\right)\cosh\left(\hat{\gamma}_{\mathrm{A}}L_{\mathrm{A}}\right)\\ +\left(\dfrac{Z_{C,\mathrm{B}}}{Z_{C,\mathrm{A}}}\sinh\left(\hat{\gamma}_{\mathrm{B}}L_{\mathrm{B}}\right)\cosh\left(\hat{\gamma}_{\mathrm{C}}L_{\mathrm{C}}\right)+\dfrac{Z_{C,\mathrm{C}}}{Z_{C,\mathrm{A}}}\sinh\left(\hat{\gamma}_{\mathrm{C}}L_{\mathrm{C}}\right)\cosh\left(\hat{\gamma}_{\mathrm{B}}L_{\mathrm{B}}\right)\right)\sinh\left(\hat{\gamma}_{\mathrm{A}}L_{\mathrm{A}}\right)\end{array}\right)^{-1} . \quad (38)$$

For a sensor port with several segments, a multiple line model can be used to obtain the complex pressure ratio. However, it becomes simpler to solve the formulation numerically. A transfer matrix approach can also be adapted to ports of many sections.[7, p. 295; 10] The development described in the previous section can easily be extended recursively to any number of line segments. A pseudocode is given below as an example. In this manner, it can be extended to consider damping effects due to thermoviscous acoustics, dissipation due to acoustic radiation out of the port, a port with multiple diameter changes, and a port with distributed fluid properties.

The pseudocode provides an outline to obtain the complex pressure ratio from the aft end of a sensor port to the inlet end. The numbering scheme in the figure 6 multiline schematic is used for the code numerical indexing. Note that the pseudocode below is written considering an infinite impedance at the back end. In this case, the specification of the location 1 impedance is unnecessary, since the location 2 impedance is defined mathematically as an infinite limit from equation (28). However, a simple modification can be made to incorporate a general diaphragm or wall impedance by specifying the value of the location 1 impedance, removing the line describing the location 2 impedance, and modifying the impedance calculation loop to begin at index 2.

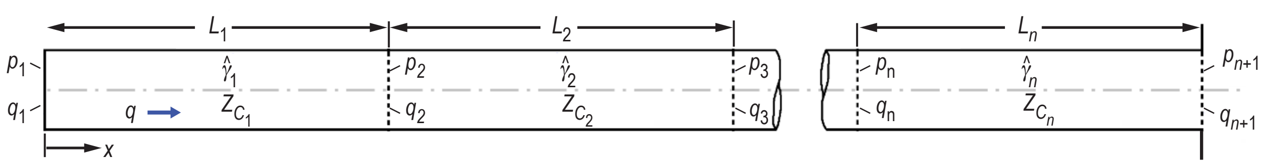

Figure 6. Pipe section schematic for programming logic of a multiline model.

As done previously, the last line segment should include parameters associated with acoustic radiation. The number of line segments would be one more than is needed for the number of physical geometric constant diameter sections or fluid property changes within the port. Also note that several input variables will be described in subsequent sections and are additionally functions of frequency, i.e., propagation constant, characteristic impedance, and length (specifically the radiation end correction length). These would need to be evaluated over the entire frequency range.

<u>Pseudocode to obtain sensor port complex transfer equation</u>

```
Input: n // number of line segments
Input: γk // propagation constant for each line segment
Input: ZC,k // characteristic impedance for each line segment
Input: Lk // length of each line segment

// use this code section if there is a one-line segment, otherwise skip ahead
if n=1 then
       pp1 = sech(γ1 × L1)
       end
end if

// obtain impedance at inlet, Zn+1, based on aft end impedance condition, Z1
Z1 = inf
Z2 = -ZC,1 / tanh(γ1 × L1)
for k = 3 to n+1 by +1 do
       Zk = [Zk-1 - ZC,k-1 × tanh(γk-1 × Lk-1)] / [1 - Zk-1 / ZC,k-1 × tanh(γk-1 × Lk-1)]
end for

// obtain transfer equation p1/pn+1 using qk/pn+1 and pk/pn+1
qpn = 1 / ZC,n × sinh(γn × Ln) + 1 / Zn+1 × cosh(γn × Ln)
ppn = cosh(γn × Ln) + ZC,n / Zn+1 × sinh(γn × Ln)
for k = n-1 to 1 by -1 do
       qpk = ppk+1 / ZC,k × sinh(γk × Lk) + qpk+1 × cosh(γk × Lk)
       ppk = ppk+1 × cosh(γk × Lk) + qpk+1 × sinh(γk × Lk)
end for

// display transfer equation p1/pn+1
disp pp1

end
```

2.4 Thermoviscous Boundary Dissipation

The acoustic framework is developed and a complex pressure ratio is derived in section 2.3; however, the propagation constants remain undetermined. The propagation constant, first described in section 2.3.1, contains information about the decay rate and phase speed of the propagating wave. This section gives background on thermoviscous boundary dissipation, with sections 2.4.1 and 2.4.2 providing the thermoviscous propagation constant. Radiation acoustics and an associated propagation constant will be discussed in section 2.5.

Acoustic dissipation in a fluid is considered by studying the propagation of acoustic waves with thermal and viscous losses. Reference 9 provides a summary of these thermoviscous effects including a description of absorption coefficients for several different thermoviscous mechanisms.

Sources of thermoviscous dissipation can be broken into two categories: damping mechanisms intrinsic to the medium and those associated with the boundary.[2, p. 210] Lossy wave equations for the different mechanisms are discussed in appendix B.

The damping mechanisms intrinsic to the medium are generally small and are often applicable to dissipation over long distances. Example intrinsic mechanisms include viscous dissipation due to relative particle motion between the compressions and expansions of a sound wave, heat conduction from a higher temperature condensation to a lower temperature rarefaction, or various molecular processes. In most cases these mechanisms are small or negligible; however, it should be noted that for some fluids and frequency ranges, these intrinsic mechanisms may be relevant.[1, pp. 301–322]

The damping mechanisms associated with the boundary are discussed in reference 1, pp. 322–324, 519–525 and reference 2, pp. 228–234 and are important for sensor port analysis. Boundary dissipation occurs due to the passage of a wave over a surface boundary. At a wall, there are viscous losses due to an acoustic shear layer and thermal losses due to heat transfer between the adiabatic fluid and isothermal wall. Both viscous and thermal effects result in the loss of energy from the propagating wave. This mode of damping is relevant in areas with small dimensions, such as in sensor ports, where an acoustic thermal and viscous boundary layer exist. Similar to a boundary layer that is caused by a steady flow, acoustic waves generate an acoustic boundary layer. The acoustic boundary layer is much thinner because the oscillatory flow continually changes direction, limiting the boundary layer growth.

In general, thermoviscous acoustics problems can be solved directly using continuity, Navier-Stokes, and an energy equation along with appropriate constitutive equations (Stokes expression, Fourier heat conduction law, and equation of state). Rather than examining the complete set of equations, described in appendix C,[11, p. 500] which would need to be solved numerically, a simpler description is useful in determining the thickness of the acoustic boundary layers. The boundary layer thickness for the oscillating flow is defined as the distance from the wall to a location where the shear-wave amplitude decays to 1/*e* of the mainstream value.

By independently examining the effect of viscosity on oscillatory wave motion, an acoustic viscous boundary layer thickness can be derived, and is given as equation (39):[1, pp. 520–523]

$$\delta_\mu = \sqrt{\frac{2\mu}{\omega\bar{\rho}}} \ . \tag{39}$$

Similarly, by examining the effect of thermal conduction on oscillatory wave motion, the acoustic thermal boundary layer thickness can be written as equation (40):[2, p. 232]

$$\delta_\kappa = \sqrt{\frac{2\mu}{\omega\bar{\rho}\,\mathrm{Pr}}} \ . \tag{40}$$

The viscous boundary layer absorption occurs because of the presence of viscosity in the fluid. Fluid particles oscillate in the main flow field, but fluid particles adjacent to the wall adhere to the wall. A transition where the oscillation amplitude decreases from the nominal amplitude in the main flow field down to zero at the wall occurs.[1, p. 322] The traditional spatial absorption coefficient associated with viscous boundary layer absorption is approximated to first order and is given as equation (41):[1, pp. 324–325; 2, pp. 228–232]

$$\alpha_{\mu} = \frac{1}{\bar{c}R} \cdot \sqrt{\frac{\mu\omega}{2\bar{\rho}}} \ . \tag{41}$$

The thermal boundary layer absorption occurs because acoustic oscillations in the main flow field occur adiabatically. However, near the pipe wall, the oscillatory flow is isothermal because the wall behaves effectively as an infinite source/sink since thermal conduction in a solid is typically orders of magnitude greater than in a fluid. The particles adjacent to the wall are therefore at a constant temperature and any temperature change in adjacent fluid is immediately quenched by heat flow into or out of the wall.[1, p. 323] The traditional spatial absorption coefficient associated with thermal boundary layer absorption is given to first order as equation (42):[1, pp. 324–325; 2, pp. 232–233]

$$\alpha_{\kappa} = \frac{1}{\bar{c}R} \cdot \sqrt{\frac{\mu\omega}{2\bar{\rho}}} \left(\frac{\gamma - 1}{\sqrt{\mathrm{Pr}}} \right) \ . \tag{42}$$

Note that the variable, γ, is used for specific heat ratio and not propagation constant.

While the traditional thermoviscous spatial absorption coefficients are given as equations (41) and (42), a wave equation that describes the thermoviscous processes is developed in literature. A quasi-1-D acoustic boundary layer model is described where the losses associated with both the viscous and thermal boundary layer are homogenized and distributed evenly across the fluid.[1, pp. 524–525; 2, pp. 230–233] The development allows simplification of the complete set of governing equations to a wave equation. Thermoviscous boundary dissipation can then be described as an effective solution and used to obtain a propagation constant.[1, pp. 324, 524] It is shown in appendix B.1 that the traditional spatial absorption coefficient, described as separate contributions in equations (41) and (42), is a first-order approximation of the wave equation exact solution.

The wave equation that describes the thermoviscous boundary dissipation from reference 1, p. 524 is written in terms of pressure as equation (43) using partial derivative notation:[1, p. 324]

$$p_{xx} - \frac{1}{\bar{c}^2} p_{tt} = \frac{2}{R} \cdot \sqrt{\frac{\mu}{\bar{\rho}\pi}} \left(1 + \frac{\gamma - 1}{\sqrt{\mathrm{Pr}}} \right) \cdot \int_0^{\infty} \frac{p_{xx}(x, t - \tau)}{\sqrt{\tau}} d\tau \ . \tag{43}$$

Note that deriving the pressure form of the wave equation rather than the particle velocity form as described in reference 1 is sometimes preferred. Obtaining this pressure form can be accomplished by first linearizing the momentum equation[1, p. 524] followed by differentiating the momentum equation with respect to the spatial variable, differentiating the linearized form of continuity and state (app. A, eq. (87)) with respect to the temporal variable, and combining the equations.

It should be noted that the domain of interest for boundary dissipation is over the length of the port geometry and not the exterior of the opening. Additionally, the acoustic boundary layer thickness must be much less than the port radius, i.e, the inequality $\delta \ll R$ must hold for this acoustic absorption model, so that the curvature of the pipe wall is much greater than either of the acoustic boundary layer thicknesses. Because of this inequality, the acoustic absorption model is sometimes referred to as the wide-pipe model. The boundary layer absorption complex wave number for this model, combining both viscous and thermal contributions, is developed in the literature as equation (44):[1, p. 325]

$$\hat{k}_{\mathrm{BL}} = \frac{\omega/\bar{c}}{\sqrt{1-\frac{2}{R}\sqrt{\frac{\mu}{i\omega\bar{\rho}}}\left(1+\frac{\gamma-1}{\sqrt{\mathrm{Pr}}}\right)}} \,. \tag{44}$$

Note that the variable γ is used for specific heat ratio and not propagation constant.

The next two subsections provide two separate thermoviscous propagation constants for use in the sensor port theoretical framework. The first propagation constant is based on traditional dissipation parameters, which are derived using first-order approximations of the exact complex wave number, equation (44); this is a common procedure described in literature.[1, p. 325] The second propagation constant is also derived using the exact complex wave number, equation (44); however, the exact form is retained. The procedure to reformulate the exact complex wave number into the expanded form described by equation (14) is developed for incorporation into the sensor port framework. Additional forms of boundary layer dissipation are also described in appendix B.

2.4.1 Thermoviscous Boundary Dissipation—Traditional Model

The total acoustic dissipation can be described using spatial absorption coefficients. In a region where multiple forms of thermoviscous absorption apply, the total absorption coefficient can be regarded as the sum of the absorption coefficients for the individual thermoviscous loss mechanisms, as shown in equation (45):[2, pp. 217, 229, 233–234]

$$\alpha = \sum_i \alpha_i = \alpha_\mu + \alpha_\kappa + \ldots \,. \tag{45}$$

Superposition is typically justified in practice, and true when losses are small; however, in general, they do have interactions with each other.[1, pp. 301–303] Note that as an approximation, this can be extended to other loss mechanisms over the same geometric domain, such as molecular relaxation absorption.

The spatial absorption coefficient associated with viscous boundary layer absorption and thermal boundary layer absorption can be combined using equation (45) into a combined boundary layer absorption coefficient. The traditional form is presented here as equation (46):

$$\alpha_{\mu\kappa} = \frac{1}{\bar{c}R} \cdot \sqrt{\frac{\mu\omega}{2\bar{\rho}}} \left(1 + \frac{\gamma - 1}{\sqrt{\text{Pr}}} \right) . \tag{46}$$

The traditional absorption coefficient for thermoviscous boundary dissipation can be obtained using a first-order approximation of equation (44).[1, p. 325] It is also possible to show that the traditional form of phase speed can be combined and written as equation (47) (elaborated in app. B.1):

$$c_{p,\mu\kappa} = \bar{c} \left(1 - \frac{\bar{c}}{\omega} \alpha_{\mu\kappa} \right) . \tag{47}$$

The phase speed can be expanded as equation (48):[1, p.325; 2, p. 233]

$$c_{p,\mu\kappa} = \bar{c} - \frac{\bar{c}}{R} \sqrt{\frac{\mu}{2\omega\bar{\rho}}} \left(1 + \frac{\gamma - 1}{\sqrt{\text{Pr}}} \right) . \tag{48}$$

The traditional propagation constant can be reconstructed by combining equations (46) and (48) using equations (14) and (16), shown as equation (49):

$$\hat{\gamma}_{\mu\kappa} = \frac{1}{\bar{c}R} \cdot \sqrt{\frac{\mu\omega}{2\bar{\rho}}} \left(1 + \frac{\gamma - 1}{\sqrt{\text{Pr}}} \right) + i \cdot \frac{\omega}{\bar{c}} \cdot \left(1 - \frac{1}{R} \sqrt{\frac{\mu}{2\omega\bar{\rho}}} \left(1 + \frac{\gamma - 1}{\sqrt{\text{Pr}}} \right) \right)^{-1} . \tag{49}$$

2.4.2 Thermoviscous Boundary Dissipation—Exact Model

The complex propagation constant shown in equation (49) is the result of combining first-order terms of a series expansion. This level of accuracy is traditionally used in most applications. However, improved accuracy can be achieved by using the exact complex wave number from the acoustic boundary layer model. For conciseness, the exact complex wave number, equation (44), is first written in terms of the traditional boundary layer absorption coefficient as equation (50) recalling during simplification that $\sqrt{8/i} = 2 - 2 \cdot i$:

$$\hat{k}_{\text{BL}} = \frac{\omega / \bar{c}}{\sqrt{\left(1 - \frac{2\bar{c}}{\omega} \alpha_{\mu\kappa} \right) + i \cdot \frac{2\bar{c}}{\omega} \alpha_{\mu\kappa}}} . \tag{50}$$

However, instead of expanding this function into a series and using only the first-order terms for analysis, the real and imaginary parts can be obtained exactly. The development is described in appendix D. The complex propagation constant is provided as equation (51) where the functions R_{den} and I_{den} are given as equations (143) and (144) in appendix D:

$$\hat{\gamma}_{\mathrm{BL}} = \left(\frac{\omega}{\bar{c}} \cdot \frac{I_{\mathrm{den}}}{\left(R_{\mathrm{den}}\right)^2 + \left(I_{\mathrm{den}}\right)^2} \right) + i \cdot \left(\frac{\omega}{\bar{c}} \cdot \frac{R_{\mathrm{den}}}{\left(R_{\mathrm{den}}\right)^2 + \left(I_{\mathrm{den}}\right)^2} \right) . \tag{51}$$

This form is always recommended, as it remains exact. Likely, it has not been derived previously due to the difficulty in obtaining a tractable complex expansion; however, with the aid of Maple™, a computer algebra system,[12] this complex expansion can be easily performed.

Using equations (14) and (16), the equation (51) propagation constant can be used to write the exact absorption coefficient and exact phase speed as equations (52) and (53), respectively:

$$\alpha_{\mathrm{BL}} = \frac{\omega}{\bar{c}} \cdot \frac{I_{\mathrm{den}}}{\left(\mathrm{R}_{\mathrm{den}}\right)^2 + \left(I_{\mathrm{den}}\right)^2} \tag{52}$$

and

$$c_{p,\mathrm{BL}} = \bar{c} \frac{\left(R_{\mathrm{den}}\right)^2 + \left(I_{\mathrm{den}}\right)^2}{R_{\mathrm{den}}} . \tag{53}$$

2.4.3 Overall Effective Dissipation Parameters

Dissipation parameters can typically be combined over a given length, however, this combination does not apply over separate segments of length. For example, equation (45) applies for thermoviscous absorption associated with a section of length, but radiation absorption acts over a separate section of length; therefore, the absorption coefficients cannot simply be summed to obtain a total absorption coefficient. Some texts provide simple examples of summing the radiation and thermoviscous resistance,[2, pp. 284–286] and apply to very specific conditions such as low frequency and lumped element. In general, this approach does not apply to sensor port analysis. If overall effective parameters are desired, appendix E details the recommended approach. While it is unnecessary to develop an effective absorption coefficient for a sensor port, it may be useful in describing the overall system.

2.5 Radiation Impedance

The previous section, section 2.4, describes the dissipation associated with thermoviscous effects. This section will provide the background on radiation acoustics, along with a propagation constant associated with radiation acoustics that can be used in the frequency response models.

An effective damping mechanism is considered that is due to the local pressure in the sensor port radiating into the fluid outside of the sensor port. Attenuation due to the geometry is not truly a damping mechanism as no absorption takes place and no energy is lost.[1, pp. 112, 298; 2, pp. 436–437] However, an effective absorption coefficient can be described that models the effect of attenuation.

As a wave propagates through a sensor port it eventually encounters an impedance at the open end. The open end is not an ideal pressure release boundary, as is often assumed, since it radiates sound into the surrounding medium. There is a non-zero impedance; therefore, a pressure node is not located at the open end.

Sound in a sensor port is not all reflected back into the port. Some sound is radiated outside of the port into the surrounding medium at the open end. The surrounding medium imposes an impedance on the propagating waves. This impedance is the radiation impedance of the acoustic wave propagated into the surrounding medium.[2, p. 184] This radiation impedance results in attenuation of the acoustics in the sensor port and an added length to the port.

At low frequencies, the only waves that can propagate in a sensor port are plane waves. The fluid at the open end location behaves as a piston with zero mass, radiating some sound out away from the port and reflecting some sound back into the port.[4, p. 471] The radiation impedance of the open end characterizes this effect, where the radiation resistance represents energy lost from the tube and the radiation reactance represents the reflection back into the port.[4, p. 472] To be precise, the energy is not lost but transferred to the surrounding environment. However, in the context of the port domain, this energy transferred out of the port is modeled as an effective absorption coefficient, assuming the acoustic motion at the opening behaves as an oscillatory piston. At higher frequencies, more energy is lost through the open end and port resonances become more damped with a broader, lower amplitude response.[4, p. 473]

2.5.1 Piston Model

Acoustic radiation that arises from a moving surface is well understood and discussed in literature. To model the effects of a plane wave leaving a sensor port that encounters a surrounding medium, piston vibration theory is considered. A damped harmonic oscillator model can be used to represent the acoustic radiation as the impedance of a pressure wave exiting the flanged sensor port.

For the sensor port application, the reaction force of the surrounding fluid back onto a driving piston is first analyzed.[1, pp. 457–460; 2, pp. 184–187; 4, pp. 381–387] The configuration is flanged and the piston is assumed to be circular and rigid. It can be shown that if a force is applied to some device (or fluid parcel), that this applied force divided by the velocity of the device (or fluid parcel) represents the sum of the input mechanical impedance plus the mechanical impedance of the device (or fluid parcel). For the piston model, the force applied by the piston similarly encounters the sum of the piston mechanical impedance and radiation impedance of the propagated acoustic wave.[2, pp. 184–185] The radiation impedance, or mechanical impedance of the fluid parcel, can be obtained generally by using equation (54), noting the overbar arc to denote mechanical impedance:

$$\breve{Z}_{\text{rad}} = \int_s \frac{df_r'}{u_x'} \quad . \tag{54}$$

It is represented by the complex reaction force divided by complex velocity at the point where the force is applied. The differential df'_r is the normal component of the piston reaction force locally on an area element dS, and u'_x is the normal component of velocity that, in general, may vary radially.[2, p. 184] Both the force term and velocity term are oscillatory functions of time.

A force balance of an oscillating piston within a fluid can be represented as a damped harmonic oscillator given as equation (55) using dot notation for differentiation, where the left-hand side represents the diaphragm motion (m is diaphragm mass, $\breve{R}_m$ is diaphragm mechanical resistance, and s is diaphragm stiffness), and f'_p is the externally applied force:[2, pp. 184–185; 13, pp. 180–181]

$$m\ddot{x}' + \breve{R}_m \dot{x} + sx' = f'_p - f'_r \ . \tag{55}$$

For a piston representing plane waves, the diaphragm is regarded as maintaining radial uniformity, where $u'_x = \bar{u}_x e^{i\omega t}$. With uniform movement, the reaction force, f'_r, can then be reduced using equation (54) and expressed in terms of the radiation impedance as $f'_r = \breve{Z}_{\text{rad}} u'_x$.

The solution to equation (55) can be written in terms of the piston velocity as equation (56):

$$u'_x = \frac{f'_p}{\breve{R}_m + i\left(\omega m - s/\omega\right) + \breve{Z}_{\text{rad}}} = \frac{f'_p}{\left(\breve{R}_m + \breve{R}_{\text{rad}}\right) + i\left(\omega m - s/\omega + \breve{X}_{\text{rad}}\right)} \ . \tag{56}$$

The radiation impedance, $\breve{Z}_{\text{rad}}$, is expanded into the real part, $\breve{R}_{\text{rad}}$, as the radiation resistance and imaginary part, $\breve{X}_{\text{rad}}$, as the radiation reactance.[13, p. 192]

For this harmonic oscillator model, an added mass can be used as a basis for a correction at the end of the port. The radiation reactance can be represented as an added mass by comparing the radiation reactance to the mass term in the imaginary part of the denominator. More precisely, this can be deduced by equating the piston velocity general solution, equation (56), to the velocity solution of a simple forced harmonic oscillator, i.e., equation (56) with $\breve{Z}_{\text{rad}} = 0$ since there would be no reaction force. By comparison, it can then be observed that the radiation reactance contributes to an overall effective mass for a simple forced harmonic oscillator, i.e., $\omega m_{\text{eff}} \equiv \omega m + \breve{X}_{\text{rad}}$. The added mass, m_{rad}, can be written as the overall effective mass minus the piston diaphragm mass, $m_{\text{rad}} = m_{\text{eff}} - m$. The added mass can also be written as the ambient density multiplied by an end correction volume, where the end correction volume is represented by the cross-sectional area of the piston, A, and an end correction. These can be equated and simply written as equation (57):

$$m_{\text{rad}} = \bar{\rho} A \Delta L = \frac{\breve{X}_{\text{rad}}}{\omega} \ . \tag{57}$$

The radiation reactance can therefore be considered individually as contributing as an added mass.

This added mass term has the effect of decreasing the resonance frequency.[2, p. 185] The mass is equivalent to that of an imaginary cylinder of ambient fluid having the same radius as the piston and length given by the end correction, ΔL.[13, p. 181] The wave encounters not a zero load but an effective load equivalent to a short continuation of the sensor port.[1, pp. 151–152] Note that the short continuation is referred to as 'effective height' when referring specifically to the piston model.

The radiation impedance that is represented in equation (56) can next be obtained by analyzing the acoustics generated in the near field. The radiation impedance due to a circular piston can be expressed in a closed form developed in literature as equation (58), where J_1 is the first-order Bessel function of the first kind, H_1 is the first-order Struve function, and R is the piston radius:[1, pp. 151, 457–460; 2, pp. 185–187]

$$\breve{Z}_{\text{rad}} = \breve{R}_{\text{rad}} + i\breve{X}_{\text{rad}} = \bar{\rho}\bar{c}A \cdot \left[\left(1 - \frac{J_1(2kR)}{kR}\right) + i\left(\frac{H_1(2kR)}{kR}\right)\right] . \tag{58}$$

Equations (59) and (60) are the real and imaginary bracketed part of equation (58), respectively, which are known as piston functions:

$$R_1(x) = 1 - \frac{2J_1(x)}{x} \tag{59}$$

and

$$X_1(x) = \frac{2H_1(x)}{x} . \tag{60}$$

They can be thought of as terms of a normalized specific acoustic impedance, normalized by $\bar{\rho}\bar{c}$, where $x = 2kR$.

Figure 7 shows a plot of the piston resistance function, $R_1(x)$, and the piston reactance function, $X_1(x)$.

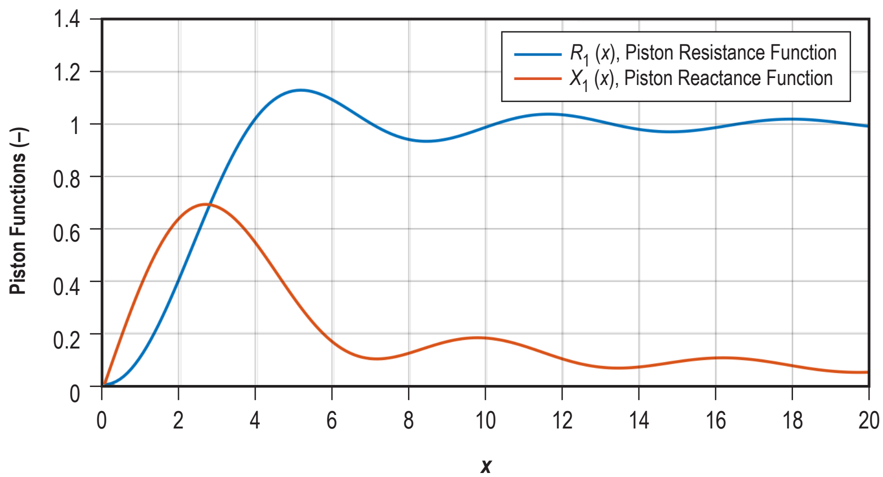

Figure 7. Radiation terms for a flanged circular piston.

As described earlier, the open end of the sensor port can be represented with this piston model. At the sensor port opening, a propagating wave leaving the sensor port confronts a sudden increase in total resistance, described by the resistance term in equation (58), and an increase in mass loading, described by the reactance term in equation (58). The radiation reactance is positive and represents an added mass that results in an overall decrease in resonant frequency.[13, p. 181] The added mass to the sensor port is referred to as the radiation mass.[2, p. 185]

A general termination impedance for a sensor port configuration can be represented as a function of the sensor port acoustics and is discussed in appendix F. This form is useful for comparing to the piston model radiation impedance, appendix G, and analysis of the end correction, appendix H.

2.5.2 Piston Model—End Correction

The radiation reactance contribution to the sensor port is examined first. Equation (57) can be rewritten as equation (61) in terms of the short continuation:

$$\Delta L = \frac{\breve{X}_{\text{rad}}}{\bar{\rho} A \omega} \ . \tag{61}$$

Equation (61) is referred to as the end correction and can now be rewritten in terms of the piston reactance function using equation (58) and noting $\breve{X}_{\text{rad}} = \bar{\rho}\bar{c}A \cdot X_1(2kR)$, where A is the cross-sectional area at the opening and R is the radius at the opening. It can subsequently be written in terms of the Struve function noting that $X_1(2kR) = H_1(2kR)/kR$ from equation (60). The end correction in terms of the piston reactance function or Struve function is given as equation (62):

$$\Delta L = \frac{X_1(2kR)}{k} = \frac{H_1(2kR)}{k^2 R} \ . \tag{62}$$

This end correction is derived from vibration theory for a flanged oscillating piston; however, it is a good representation of an oscillating planar wave at a sensor port opening.[1, pp. 151–152] The contribution of the port may influence the sensor port end correction slightly and is discussed further in appendix H.

Equation (62) reveals that the end correction is in fact frequency dependent and a precise model would incorporate this dispersion. The well-known end correction, equation (2), can be derived by characterizing the low-frequency limit of equation (62). To obtain this approximation, equations (59) and (60) are written as a formal Maclaurin power series in equations (63) and (64):

$$R_1(x) = 1 - \frac{2J_1(x)}{x} = \sum_{m=0}^{\infty} \frac{(-1)^m}{\Gamma(m+2)\Gamma(m+3)} \left(\frac{x}{2}\right)^{2m+2} = \frac{x^2}{2 \cdot 4} - \frac{x^3}{2 \cdot 4^2 \cdot 6} + \frac{x^5}{2 \cdot 4^2 \cdot 6^2 \cdot 8} - \cdots \tag{63}$$

and

$$X_1(x) = \frac{2H_1(x)}{x} = \sum_{m=0}^{\infty} \frac{(-1)^m}{\Gamma(m+3/2)\Gamma(m+5/2)} \left(\frac{x}{2}\right)^{2m+1} = \frac{4}{\pi}\left(\frac{x}{3} - \frac{x^3}{3^2 \cdot 5} + \frac{x^5}{3^2 \cdot 5^2 \cdot 7} - \cdots\right) . \quad (64)$$

Appendix I discusses alternate forms of the power series and appendix J provides a pseudocode for calculation of the Struve function.

The linearization of the expansion near $x = 0^+$ is given as the first term in equation (64). The low-frequency approximation is given as equation (65):

$$X_1(x) \approx \frac{4x}{3\pi} . \quad (65)$$

This can be visualized in figure 7 as a linear approximation to the exact solution in the low-frequency limit, where $2kR \ll 1$.

This low-frequency approximation can be applied to equation (62), where $x = 2kR$ to give the well-known end correction, equation (2). At low frequency, the piston appears to be loaded with a cylindrical volume of fluid whose cross-sectional area is πR^2 and length given by the end correction, rewritten as equation (66):[2, p. 187; 14, p. 220]

$$\Delta L \approx \frac{8R}{3\pi} . \quad (66)$$

Note that the end correction for this low-frequency approximation is not frequency dependent.

The relative error as a percentage, δ, can be calculated from exact and approximate values, v, using equation (67):

$$\delta = 100 \cdot \left| \frac{v_{\text{exact}} - v_{\text{approx}}}{v_{\text{exact}}} \right| . \quad (67)$$

The error associated with the end correction is obtained by applying equations (62) and (66) to equation (67). At $x = 1$, $x = 2$, and $x = 3$, the error is approximately $\delta \approx 6.9\%$, $\delta \approx 31.2\%$, and $\delta \approx 87.2\%$, respectively. In many cases the fundamental mode is well below $x = 1$ and the error is small in using equation (66). However, for precise calculations in all port configurations and at higher frequencies, the exact formula in equation (62) is recommended. References 15 and 16 discuss efficient approximations for the Struve function since equations (63) and (64) become increasingly difficult to evaluate, which may be necessary to achieve a small relative error. An end correction comparison between the exact solution and approximate solution is shown in figure 8 for an example sensor port with radius 0.25 in (0.00635 m) and ambient air.

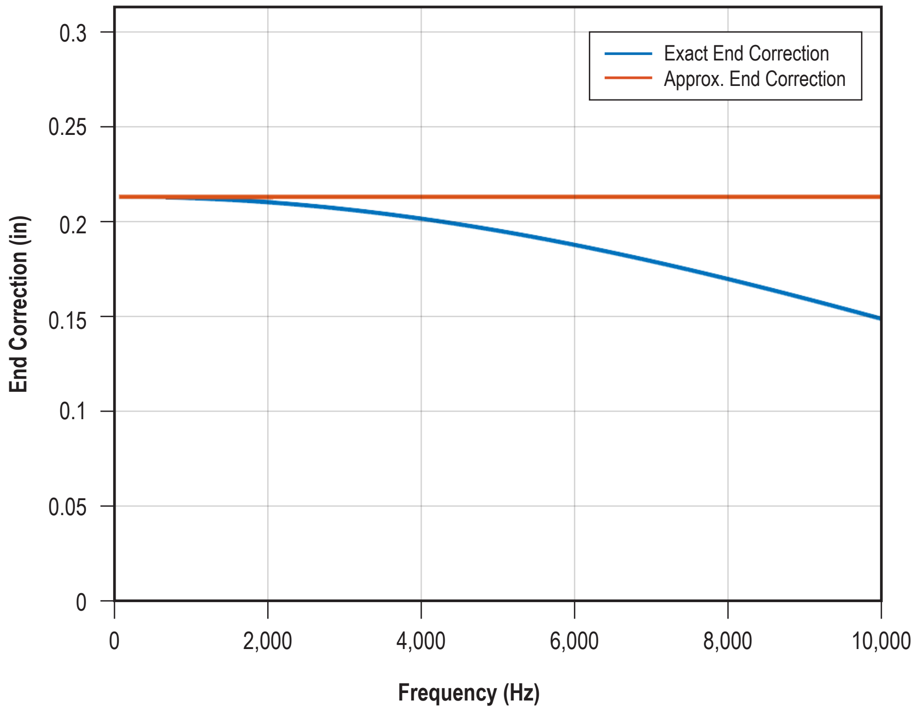

Figure 8. Exact and approximate end correction: Ambient air ($\bar{c}$ = 1,140 ft/s) and 0.25 in radius (figure uses EE units).

2.5.3 Piston Model—Propagation Constant

For the simple harmonic oscillator model described in equation (55), the temporal absorption coefficient for the radiation mechanism, $\tilde{\beta}_{\text{rad}}$, is given as equation (68):[2, pp. 8–11, 17, 184–185]

$$\tilde{\beta}_{\text{rad}} = \frac{\breve{R}_{\text{rad}}}{2m_{\text{rad}}} \; . \tag{68}$$

The tilde denotes that the parameter is not related to the phase shift parameter, β, used throughout this TP. The temporal absorption coefficient parameter is commonly written in terms of damping ratio and undamped natural frequency as $\tilde{\beta} \equiv \zeta\omega_n$.

Both the temporal absorption coefficient and the spatial absorption coefficient can be used to describe the amplitude decay of a pressure wave. The temporal absorption coefficient from the time-domain SDOF system can be transformed into the spatial absorption coefficient using the following relationship:[1, pp. 299–300; 2, pp. 8–11, 17, 212, 217, 285]

$$\tilde{\beta}_{\text{rad}} = \bar{c}\alpha_{\text{rad}} \; . \tag{69}$$

This transformation represents the wave nature of propagation where a transient disturbance remains unchanged and travels along a spatial direction.[1, p. 6; 2, p. 40]

Substituting equation (69) into equation (68) and using equation (57) gives the form of the spatial absorption coefficient representing the radiation mechanism:

$$\alpha_{\text{rad}} = \frac{k}{2}\frac{\breve{R}_{\text{rad}}}{\breve{X}_{\text{rad}}} \; . \tag{70}$$

Note that the absorption coefficient incorporates the contribution of both the radiation resistance and radiation reactance. Substituting the resistance and reactance terms of equation (58) into equation (70) and using the relationship in equation (62) gives a useful form of the absorption coefficient. The spatial absorption coefficient associated with radiation impedance can be written as equation (71), considering that the acoustic radiation from the flanged port behaves as the pressure field generated by a flanged piston:

$$\alpha_{\text{rad}} = \frac{1}{2\Delta L}\cdot\left(1-\frac{\bar{c}\cdot J_1(2\omega R/\bar{c})}{\omega R}\right) \; . \tag{71}$$

The end correction length is a characteristic dimension or artificial length that describes the additional mass of fluid necessary to simulate the radiation impedance. The radiation contribution associated with the harmonic oscillator is embedded entirely in the absorption coefficient at the opening location. The propagation of a pressure response associated with the reaction to an oscillating piston, though, is simulated within the lossless fluid (no thermoviscous dissipation) outside of the port over the length of the end correction. Because the fluid over the span of the end correction is lossless, the phase speed is simply the ambient sound speed $c_{p,\text{rad}} = \bar{c}$. Noting that the phase shift parameter can be written using equation (16), the propagation constant for the radiation mechanism can be described using equation (72):

$$\hat{\gamma}_{\text{rad}} = \alpha_{\text{rad}} + i\beta_{\text{rad}} = \frac{1}{2\Delta L}\cdot\left(1-\frac{\bar{c}\cdot J_1(2\omega R/\bar{c})}{\omega R}\right) + i\frac{\omega}{\bar{c}} \; . \tag{72}$$

Expanding this equation using the accurate definition of the end correction gives the propagation constant for acoustic radiation explicitly as equation (73):

$$\hat{\gamma}_{\text{rad}} = \frac{R\omega^2/\bar{c}^2}{2H_1(2\omega R/\bar{c})}\cdot\left(1-\frac{\bar{c}\cdot J_1(2\omega R/\bar{c})}{\omega R}\right) + i\frac{\omega}{\bar{c}} \; . \tag{73}$$

The propagation constant described here for acoustic radiation effects is a critical advancement for application to sensor ports. Depending on the sensor port configuration, the influence of radiation acoustics can be significant.

3. NUMERICAL MODELING

3.1 Background

A primary advantage of a computer simulation, or numerical modeling, is to tackle problems that are too complex for analytical solutions. Additionally, it is also a very useful approach in gaining insight into relevant physical mechanisms and important system features. Tools such as COMSOL Multiphysics® and the ANSYS software suite are examples of well-known engineering multiphysics software tools. These tools provide a simple workflow and user interface, incorporate and numerically simulate coupled physical models, and provide a means to manage solution data and visualize results. The examples and procedures in this TP will use COMSOL version 5.4[17] as the numerical modeling tool.

While the sensor port analytical models are relatively simple and efficient, they are tractable because assumptions are enforced and limitations exist. In many cases, the limitations may not be relevant and the solution is representative; however, there are situations where more complex physics must be included. By using COMSOL, many of these limitations can be addressed in a rigorous manner. There are several examples of limitations that may be relevant to a sensor port analysis that are not usually incorporated in an analytical model. These include the effects of crossflow over the sensor port opening; flow through the sensor port; finite and realistic geometry, such as a port installed in a pipe rather than in an infinite medium; thermal conditions surrounding the sensor port; nonlinear finite acoustics; unsteady losses at geometric interfaces; accurate property distribution in the ambient surroundings and port geometry; fluid-structural interaction; and true dynamic behavior of the fluid system, rather than using the piston model described in section 2.5.1 as an approximation.

Aside from the removal of physical and geometric limitations, there is another very important advantage in using a numerical framework for sensor port analysis. A direct comparison can easily be made by comparing the solutions of the exact configuration (with a sensor port) and the desired configuration (usually with no sensor port). Often, it is desired to remove the effects of the sensor port or understand what the port influence is to help determine the acceptable response range. This can be addressed by simulating the exact configuration and the desired configuration separately using all of the identical simulation conditions, e.g., same excitation source and same boundary conditions. Because the numerical simulation is deterministic, the pertinent quantities of interest between the two configurations can be obtained very precisely. The theory for this comparative analysis is developed and described later in the section. This innovative, yet very basic, procedure is remarkably powerful when combining solutions from deterministic numerical simulations.

Computer simulations have many advantages, nevertheless there are some disadvantages. Depending on the additional physics and domain included, the computation can be extremely time intensive. However, computer speed and numerical algorithms are always improving. Additionally, one difficult part of computer simulation is often the model setup; however, COMSOL's work flow is designed so that the setup difficulty is minimized.

3.1.1 Numerical Framework

Several model frameworks are used in the forthcoming numerical analyses. While the model description and usage are discussed throughout the following sections, the details and mathematical formulations of each model framework can be found in reference 11.

3.2 Numerically Modeling Piston Functions

In this section, the piston functions that are discussed theoretically in section 2.5.1 are modeled numerically by solving the Helmholtz equation in the frequency domain. This is done by using the COMSOL Pressure Acoustics, Frequency Domain Interface. This interface is suited to model pressure variations for the propagation of acoustic waves in fluids at quiescent background conditions.

This simple numerical example is a very important step in the sensor port analysis. Most importantly, it provides a verification that relevant radiation acoustics physics can be modeled adequately in a forthcoming sensor port analysis (sec. 3.4). The error can be assessed by making a comparison between this numerical piston model solution and the exact piston model solution. Minimizing this error aids in optimizing the sensor port analysis since considerations would be made in using the same fluid properties, domain, boundary conditions, frequency range, and mesh design.

Equation (58) shows that both the fluid properties and the radius influence the piston functions and radiation impedance. Therefore, for a typical verification analysis, the piston radius would be set equal to the sensor port opening radius and the fluid properties would also be the same. Satisfactorily simulating the piston functions over the sensor port frequency range of interest ensures that the radiation acoustics will be captured adequately in a sensor port with the same radius and fluid. Considering that the sensor port response will be studied using the same setup, addressing regions of large error in the numerical piston model can help determine optimal domain and mesh designs for use in the sensor port analysis. To satisfactorily model the radiation impedance in the sensor port model, both the domain and mesh need to be designed appropriately.

3.2.1 Example Flanged Circular Piston

The acoustics associated with an oscillatory piston of radius 0.25 in (0.00635 m) is studied in ambient air. The air is at a temperature of 77 °F (298.15 K) with sound speed 1,136 ft/s (346 m/s) and density 4.2779×10^{-5} lb_m/in^3 (1.1841 kg/m^3). The total domain radius is 7.5 in (0.1905 m), which is 30× the piston radius, and includes a 0.375-in-thick (0.009525-m-thick) perfectly matched layer (PML) that behaves as an absorptive boundary. A grid refinement region is also defined at 10× the piston radius near the far-field transition radius. The analysis is explored over the bandwidth through 20,000 Hz by increments of 200 Hz. The minimum wavelength of interest, an important parameter for mesh resolution, is therefore 0.6816 in (at 20,000 Hz).

Note that the default COMSOL configuration takes metric input values and are used in the numerical analyses.

3.2.2 Domain Setup

Figure 9 shows the general domain setup for numerically modeling the piston functions. The domain is designed using a 2-D axisymmetric model where the vertical axis is the axis of symmetry.

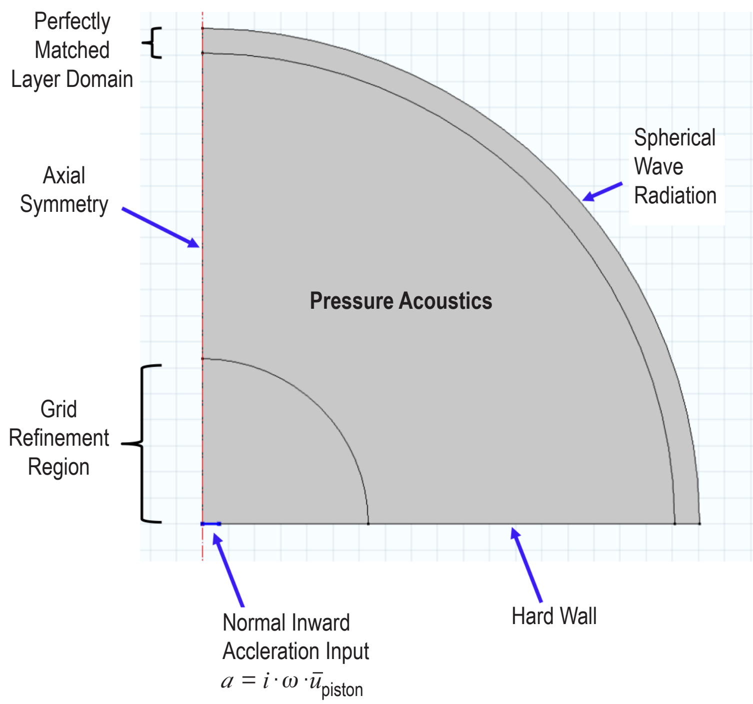

Figure 9. Modeling piston functions—2-D axisymmetric domain setup.

The piston is defined as a horizontal radius (blue) in the lower-left part of the domain with an inward normal acceleration. The acceleration can be represented as $a = i \cdot \omega \cdot \bar{u}_{\text{piston}}$ given the piston velocity, $\bar{u}_{\text{piston}}$. A constant velocity amplitude is imposed and set at 3.28 ft/s (1 m/s). Any value for the piston velocity is acceptable as this is a linearized model and impedance calculations consider both the input and response.

Except for the piston radius, the rest of the horizontal axis is defined as a sound hard (closed) boundary where the normal component of acceleration (and velocity) is zero. This definition is consistent with the hard wall definition used for a flanged baffle from section 2.5.

The piston functions are estimated for a piston set in a plane baffle of infinite extent. An ideal PML absorbs all outgoing waves without causing spurious reflections and would represent the infinite extent. In this problem, a PML is defined using a thickness of 5% of the overall domain radius. The spherical wave radiation boundary behind the PML provides a final layer of protection, but may only provide minimal error improvements. The default value of 1 was used for the PML scaling factor; however, it was found that further improvement in error was obtained in the low-frequency range by modifying the PML scaling curvature parameter to a value of 2. These parameters affect how the PML virtually stretches the local coordinate system creating a semi-infinite domain.

A sensitivity study for this problem showed that the PML could acceptably resolve the acoustic response down to a minimum frequency that has a wavelength approximately 10× longer than the domain radius. This approximation is not definitive as it can be influenced by various attributes, but may serve as a starting point for evaluation of error. For this example, to resolve a 200-Hz response in air, which has a 5.71-ft (1.74-m) wavelength, the domain radius (not including the PML) should be no smaller than 6.85 in (0.174 m), given the speed of sound of 1,138 ft/s (347 m/s). The overall domain radius is set to 30× the piston radius which gives a value (not including the PML) of 7.13 in (0.181 m). This ensures that error is addressed as low as 200 Hz. Evaluation of lower frequencies may need a larger domain; however, the large errors may be relatively inconsequential at very low frequencies as the radiation impedance values are near zero.

Other considerations may come into play in the design of the overall domain size, and error should always be reviewed because of unique aspects of a particular problem.

3.2.3 Mesh Design

A major source of error can arise by inadequately resolving the mesh. One particular area of interest should be the vicinity of the piston where the surface pressure and reaction force must adequately be resolved. Consider that the pressure produced by the piston results from a continuum of flanged simple sources that radiate spherically.[2, pp. 172, 179] Across the entire surface of the piston, each infinitesimal area produces an incremental pressure.[2, p. 185] And for a very short piston radiation wavelength, where $kR \gg 1$, each portion of the surface radiates separately and is separately loaded.[4, pp. 385–386] A refinement of 100 grid points across the piston provided a diminishing return in error over the range of wavelengths examined. As these additional grid points are only needed across the piston, the computational expense is not greatly increased.

An arc at 10× the piston radius is defined that encompasses a grid refinement region, and is shown in figure 9. This region is used for a more refined mesh in order to better resolve the near-field radiation effects. This region is loosely based on the characteristic far-field transition distance which can be inferred considering $r \gg R$ and $r \gg kR^2$.[14, p. 225] Selecting the widest of these two ranges is more conservative than using the Rayleigh distance, which marks the transition from near field to far field, defined in reference 1 as $r \gg kR^2/2$. Reference 18 provides a thorough review on various other definitions of the near-field and far-field transition distance. For this example, a free triangle mesh in this refined region was specified using a size expression such that the elements were no larger than the smaller of two values: 6× smaller than the piston radius or 30× smaller than the minimum wavelength. In the courser region, the free triangle mesh was also based on the smaller of two values: 4× smaller than the piston radius or 20× smaller than the minimum wavelength. In this example, the maximum frequency is 20,000 Hz; therefore, the smaller wavelength-based definition is used for the mesh. These definitions are loosely based on sensitivities that show an acoustic wavelength can be resolved with approximately five elements, but also to ensure good element transition from the higher refined regions to the lower refined regions. In addition, while not systematically studied, the increased mesh refinement region was implemented to capture interference and directivity attributes in the near field.

The PML was specified using a mapped grid. This allowed the ability to use a specified quadrilateral element mesh distribution. This element type is preferred in the PML domain to minimize numerical discretization error. Ten elements in the radial direction were specified in this example.

Figure 10 shows the mesh in the region near the PML and near the piston. The overall mesh is comprised of 116,822 elements and 60,539 mesh vertices.

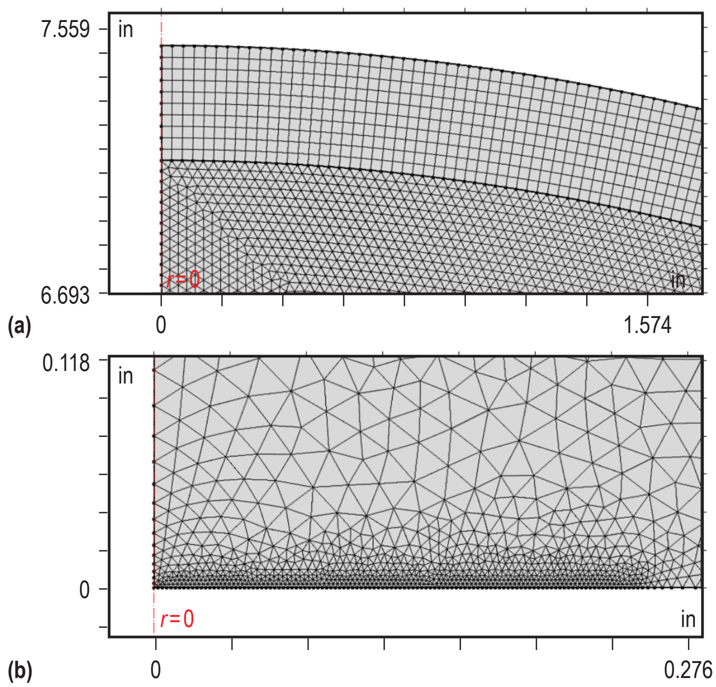

Figure 10. Mesh near (a) PML and (b) piston. Note different axes scales (figure uses EE units).

3.2.4 Comparison of Numerical and Analytical Solution

A piston function comparison between the numerical COMSOL solution using the domain and mesh previously described and exact analytical solution is shown in figure 11. The exact curves for the piston resistance function and piston reactance function can be plotted as a function of frequency using equations (59) and (60), respectively. In COMSOL, equation (54) can be used directly to estimate the numerical value of the mechanical impedance; subsequently, the piston functions can be estimated from the real and imaginary part (and normalized by $\overline{\rho}\overline{c}A$). The functions shown in equations (74) and (75) can be estimated numerically at each frequency using COMSOL to obtain the piston resistance function and the piston reactance function, respectively. The density and sound speed are directly used in the evaluation; however, their effect on amplitude is canceled by the evaluation of the integral term. This can be observed by comparing equations (54), (58), (59), and (60). This evaluation is performed at each frequency to numerically produce the curves in figure 11.

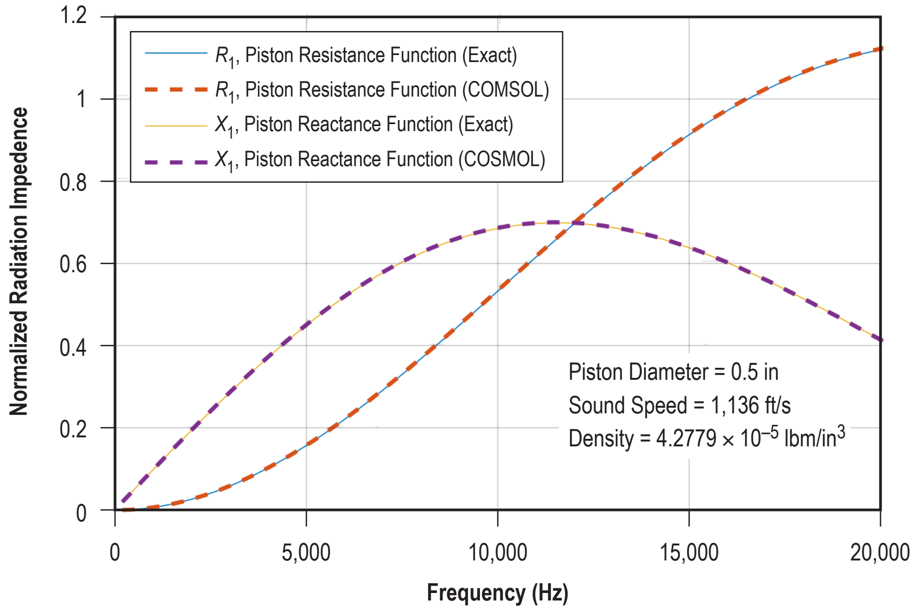

Figure 11. Piston functions as a function of frequency for a 0.5-in-diameter piston in ambient air.

While normalized piston functions apply for any circular piston in any fluid, the geometry and properties are noted in the figure used to numerically produce the curves:

$$R_1 = \frac{1}{\bar{\rho}\bar{c}\pi R^2} \cdot \Re\left(\int_0^{2\pi} \int_0^{R} \frac{p(r)}{u_x(r)} r \, dr d\theta \right) \tag{74}$$

and

$$X_1 = \frac{1}{\bar{\rho}\bar{c}\pi R^2} \cdot \Im\left(\int_0^{2\pi} \int_0^{R} \frac{p(r)}{u_x(r)} r \, dr d\theta \right) . \tag{75}$$

The normalized form is plotted analytically in figure 7; however, plotting at each frequency in figure 11 demonstrates the piston function contribution that would apply to a typical sensor port. Using this same example, appendix G compares piston functions of a flanged piston to those from a flanged sensor port.

Using the COMSOL results as the approximate solution and the analytical formula as the exact solution, the relative error as a percentage can be obtained for the piston functions using equation (67). Figure 12 shows the relative error as a function of frequency. The relative error is investigated over the range of frequencies to assure that the acoustic radiation physical mechanism is captured appropriately and the mesh and domain design can be used acceptably in a sensor port analysis.

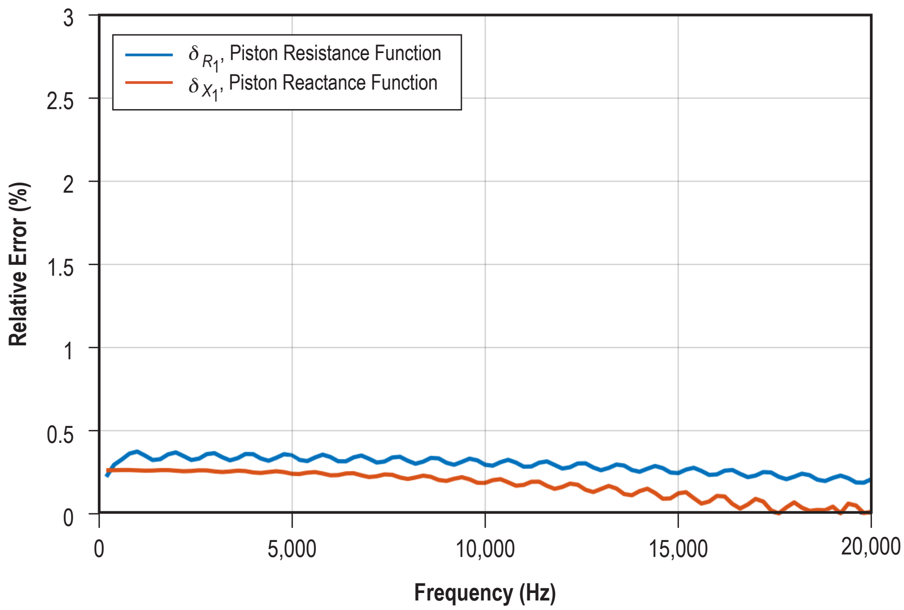

Figure 12. Piston function percent relative error.

Figure 13 shows the effective piston height as a function of frequency. As discussed previously in section 2.5.1, the piston appears to be loaded with a cylindrical volume of fluid whose cross-sectional area is πR^2 and height given by the exact curve in figure 13.[2, p. 187] This is equivalent to applying an end correction to a sensor port. The exact curve for a flanged piston can be plotted using equation (62) and the approximate solution is from equation (66). It was shown previously in sections 2.5.1 and 2.5.2 that the end correction is related to the imaginary part of the mechanical impedance and can be obtained numerically. In COMSOL, equation (61) can be used directly to estimate the numerical value of the effective height by incorporating the radiation reactance from equation (54). At each frequency, the function shown in equation (76) can be evaluated:

$$\Delta L = \frac{1}{\bar{\rho}\omega\pi R^2} \cdot \Im\left(\int_0^{2\pi} \int_0^R \frac{p(r)}{u_x(r)} r \, dr d\theta \right) . \tag{76}$$

Figure 13 shows that, for a piston, the exact effective height solution compares identically to the numerical solution. The approximate solution compares well only at low frequencies. The error associated with the effective height is identical to the error of the piston reactance function.

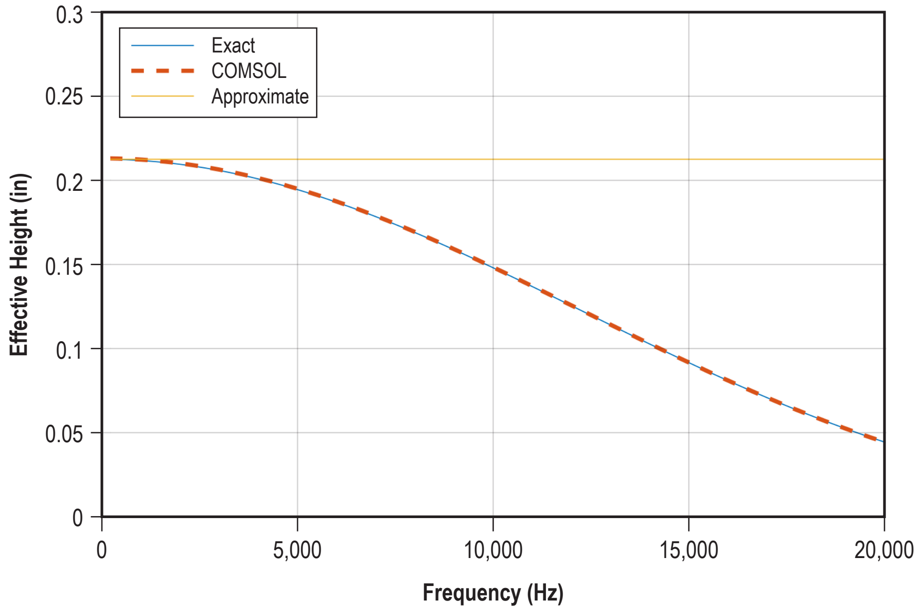

Figure 13. Piston effective height as a function of frequency (figure uses EE units).

3.3 Numerical Analysis of Thermoviscous Boundary Dissipation

In the previous section, a piston model was analyzed to verify the radiation acoustics physical mechanism and also to aid in domain and mesh design of the forthcoming sensor port simulation (sec. 3.4). In this section, the thermoviscous boundary dissipation previously discussed theoretically in section 2.4 is modeled numerically and analytically in several different ways. Three separate numerical approaches using COMSOL are first compared. Four separate analytical models are also compared. The comparisons are made to understand and explore differences. Table 1 summarizes the different thermoviscous acoustic models in increasing order of accuracy.

Table 1. Numerical and analytical models of thermoviscous boundary dissipation.

Model Name	Type	Domain	Equation	Description
Heuristic	Analytical	Frequency	Helmholtz equation	Propagation constant from Heuristic model
Traditional	Analytical	Frequency	Helmholtz equation	Propagation constant from physical model—a first-order approximation
Exact—with First-Order Approximation	Analytical	Frequency	Helmholtz equation	Propagation constant from physical model—a first-order approximation
Exact	Analytical	Frequency	Helmholtz equation	Helmholtz equation with exact propagation constant from physical model
Narrow Region Acoustics	Numerical	Frequency	Helmholtz equation	Helmholtz equation with exact propagation constant from physical model
Thermoviscous Acoustics	Numerical	Frequency or time domain	Linearized compressible flow equations	Navier-Stokes with continuity and energy that has been linearized
Multiphysics	Numerical	Time domain	Compressible flow equations	Navier-Stokes with continuity and energy: coupled laminar flow and fluid heat transfer

The first numerical approach listed is the Narrow Region Acoustics model. In this method, the Helmholtz equation is solved numerically in the frequency domain, and a complex wave number that is described by a boundary layer dissipation theoretical model is applied to the numerical framework.[1, pp. 324–325; 17] In fact, COMSOL uses the exact form of the complex wave number described by equation (44) in its numerical framework. This approach effectively is a quasi-1-D model where the dissipation is distributed evenly within the fluid throughout the port. The Narrow Region Acoustics model is implemented by using the COMSOL Pressure Acoustics, Frequency Domain interface and adding a COMSOL Domain node called Narrow Region Acoustics. This model has a very low computational cost compared to the numerically and physically more accurate Thermoviscous Acoustics and Multiphysics models, but is not accurate in all scenarios such as for short, high-aspect ratio ports or ports that do not have a constant cross section.[17] The numerical approach is equivalent to using the Exact analytical model where the propagation constant is derived from the Exact thermoviscous model described previously as equation (51).

The second numerical approach is referred to as the Thermoviscous Acoustics model and, in general, is an improvement in accuracy. This model uses the linearized Navier-Stokes equations with quiescent background conditions including continuity and an energy balance. It can be applied in the frequency domain or time domain, but is studied here in the frequency domain using the COMSOL Thermoviscous Acoustics, Frequency Domain interface. This interface is suited to model pressure, velocity, and temperature variations for the propagation of acoustic waves with quiescent background conditions near walls where viscous and thermal boundary layers exist.[17]

The third numerical approach, referred to as the Multiphysics model, is the most accurate and solves the complete Navier-Stokes equations including continuity, along with the convective-diffusion energy equation (including sources) and is described in appendix C.[11, pp. 500–501] The Multiphysics model can be applied only in the time domain, by manually coupling COMSOL's Laminar Flow interface with its Heat Transfer in Fluids interface. This multiphysics interface is suited to model pressure, velocity, and temperature variations and can be extended to more complex cases such as finite-amplitude (nonlinear) waves, propagation in liquids, or acoustics with flow. The Multiphysics model is similar to frameworks used in traditional computational fluid dynamics (CFD) and simulates both the flow effects and heat transfer in the fluid. One important contribution incorporated in the energy balance is associated with the pressure work. The work done by changes in pressure, including heating through adiabatic compression, is discussed in reference 19, pp. 336–337, where the energy change equation for a fluid is written in the form of temperature. Further details of the energy change equation for a fluid are described in appendix K. In COMSOL, the pressure work contribution is incorporated by including the Pressure Work subnode within the Heat Transfer in Fluids interface Fluid node. While the analysis in this TP couples the Laminar Flow interface with its Heat Transfer in Fluids interface to compute the Multiphysics simulation, note also that COMSOL can automatically set up a Multiphysics model by using the Laminar Flow interface in the Nonisothermal Flow branch. The nonisothermal model is more comprehensive, e.g., accounting for heat transfer in solids. It may require numerical stabilization so the numerical solvers are also set up considering the more complex problems. The additional structural interface complexities are not considered traditionally for the thermoviscous acoustics problems and so the manual coupling is preferred using isothermal wall boundaries.

The analytical models listed in table 1 are similar to the Narrow Region Acoustics numerical model, where the Helmholtz equation (or time-independent wave equation) is solved using a propagation constant that describes the thermoviscous dissipation. The multiple analytical models only differ by applying separate propagation constants, which are dependent on the particular boundary layer dissipation theoretical model and approximation made. The most accurate analytical propagation constant for boundary layer dissipation is given as equation (51) and referred to as the Exact model. A first-order approximation to the exact solution is occasionally used, described in appendix B.2, given as equation (114), and referred to as the Exact—with First-Order Approximation model. The traditional approach to acoustics problems uses formulas that can be reconstructed into a propagation constant as equation (49) and is referred to as the Traditional model, also described in appendix B.1. Lastly, the Heuristic model, described in appendix B.3 and given by equation (121) is an approximation analogous to a damped SDOF system and considers heuristically that there is a general pressure drop per unit length associated with thermoviscous effects.

In this TP, the analytical framework uses a pressure transfer equation model, equivalent to solutions of the Helmholtz equation, and is derived from the wave equation in appendix A. For comparisons in this section, the analytical solutions use the equation (29) transfer equation for a one-line model and incorporate a propagation constant based on one of the four separate analytical models.

The analysis in this section provides verification that the physics associated with thermoviscous dissipation, i.e., acoustic boundary layer dissipation, is modeled adequately and will be effectively applied to the forthcoming sensor port analysis. To model the acoustic boundary layer dissipation satisfactorily within the sensor port, both the domain and mesh need to be designed appropriately.

3.3.1 Numerical Model Example—Thermoviscous Boundary Dissipation

The response associated with a port of radius 0.25 in (0.00635 m) and length of 5 in (0.127 m) is numerically studied in ambient air at a temperature of 77 °F (298.15 K).

Note that the Thermoviscous Acoustics and Multiphysics models do not use sound speed explicitly as these models are simulated using primitive variables. The density in these models is described by a fourth-order constitutive equation of state as a function of pressure and temperature that is fit to real data from the REFPROP software.[20] However, the Narrow Region Acoustics model—based on the wave equation—does require a sound speed as an input material property. For an equal comparison of the linearized models, the equilibrium soundspeed is evaluated from the Thermovisocus Acoustics model solution, and then specified in the Narrow Region Acoustics model. Similarly, the analytical models require additional fluid property inputs. For an equal comparison, all properties are evaluated directly from the linearized Thermoviscous Acoustics model solution.The frquency domain models are explored over the bandwidth through 5,000 Hz by increments of 2 Hz.

3.3.2 Domain Setup

The domain setup is described for the Thermoviscous Acoustics model. Differences in domain setup are also noted for the Narrow Region Acoustics and Multiphysics models. Figure 14 shows the general domain setup for numerically modeling the dissipation effects associated with the acoustic boundary layer in a one-line port model. The domain is designed using a 2-D axisymmetric model where the vertical axis with the dashed red line is the axis of symmetry.

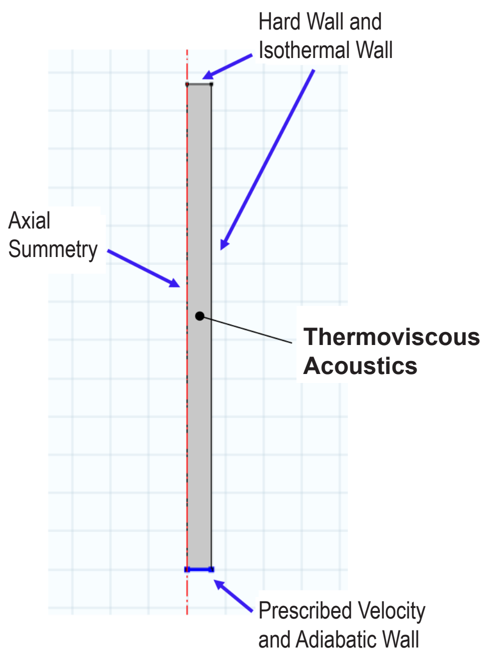

Figure 14. Modeling thermoviscous effects—
2-D axisymmetric domain setup.

To model the frequency response function (also referred to as the transfer function in this TP) of the port, the concept of input impedance is applied. The input impedance, or driving-point impedance, is the system equivalent impedance that is seen by an external source. The input impedance is a measurement of impedance at one location, but describes the spatial wave propagation through the entire system. Therefore, a transfer function can be obtained by applying an external source at one end of the port, followed by measuring the input response at the driven end and the output response at the other end of the port.[2, pp. 281–283] To apply a source that behaves as an open (soft) boundary, the external source should be applied as a massless driver with no stiffness.[2, pp. 281–283] In COMSOL, a massless driver with no stiffness can be applied simply by using a prescribed velocity at one end as shown in figure 14. Using this approach, the resulting pressure transfer function can simply be probed. This general approach is used to obtain lumped models for acoustic elements, such as short cavities, Helmholtz resonators, and more complex acoustic networks.[1, pp. 144–150, 153–156; 2, pp. 280–286] A constant velocity amplitude is imposed and set at 3.28 ft/s (1 m/s). However, any value for the prescribed velocity is acceptable as this is a linearized model and transfer function calculations consider both the input and response.

Note that in the Multiphysics model, a velocity amplitude of 3.28×10^{-5} ft/s (1×10^{-5} m/s) is applied since the model is not linearized and input amplitudes do play a role. This velocity input produced a maximum pressure near 5.8×10^{-5} psi (0.004 Pa), which is well within the acoustic regime. The input impedance concept does not apply for the time domain model.

The port walls behave effectively as an infinite heat source or sink and can be modeled as an isothermal boundary.[1, p. 323] In the fluid mainstream, the compressions and expansions take place adiabatically.[1, p. 323] The driver location represents the open end of the port in the mainstream of the fluid, so an adiabatic condition best approximates the thermal condition at this boundary. There would be no heat transfer to a wall at this boundary and the temperature would not be constrained. Sensitivities show that the thermal boundary condition of the acoustic driver has a negligible effect on results.

The remainder of the domain consists of an axis of symmetry and hard walls as shown in figure 14.

Figure 14 shows the general domain setup for numerically modeling the dissipation effects associated with the acoustic boundary layer for the Thermoviscous Acoustics model. The domain setup for the Narrow Region Acoustics model is very similar to the setup shown in the figure except that it has no thermal boundary conditions. The COMSOL wide duct approximation selection allows the model to apply analytical propagation constants that account for thermoviscous dissipation.

The Multiphysics model has a couple additional domain considerations. As noted previously, it uses the COMSOL Laminar Flow and Heat Transfer in Fluids physics interfaces. The first consideration is the differing nomenclature in the Heat Transfer in Fluids where the terms in figure 14, Adiabatic and Isothermal, are referred to as Thermal Insulation and Temperature, respectively. The more important interface characteristic is to ensure the variables in the Heat Transfer in Fluids interface work together with the variables in the Laminar Flow interface. To ensure this occurs, the Fluid Properties node in the Laminar Flow interface and Fluid node in the Heat Transfer in Fluids interface must use instantaneous dependent variables instead of ambient conditions. For example, the absolute pressure should be given as, $p + p_0$, and the temperature as the instantaneous temperature, T, rather than using the global steady ambient conditions, p_0 and T_0. Note that the variable T in those interfaces is the instantaneous temperature including both the unsteady and ambient temperature.

3.3.3 Numerical Model—Mesh Design

For the Narrow Region Acoustic model, only typical acoustic considerations should be made regarding the mesh design as the dissipation effects are homogenized over all the elements. Generally, for this case, the number of elements needed is purely based on the number of elements needed to resolve an acoustic wavelength, i.e., approximately five elements.

For the Thermoviscous Acoustics and Multiphysics models, the primary mesh design requirement should address capturing the dissipation effects. Efforts should be made to ensure there are enough elements within the acoustic boundary layer. A sensitivity study showed that a diminishing return on accuracy can be obtained where the thickness of the element closest to the wall is approximately one-third the size of the minimum boundary layer thickness. The minimum boundary layer thickness can be obtained by considering the highest frequency of interest and using equations (39) and (40), which define the viscous and thermal boundary layer thickness, respectively. Lower frequencies will have a larger boundary layer thickness; therefore, they would already contain an additional number of elements. However, even a mesh with elements approximately the same size as the boundary layer thickness produce reasonable results. It is recommended that a sensitivity study be performed to investigate the effect of element size on relative error.

In COMSOL, a Mesh Boundary Layer node can be used to set the thickness of the first layer element, h, the layer stretching factor, S, and the number of layer elements, n. Using equation (77), the total length of the boundary layer mesh, L_{BL}, is obtained before there is a transition to the interior mesh:

$$L_{\mathrm{BL}} = h\frac{S^n - 1}{S - 1} \ . \tag{77}$$

For this example the element closest to the wall is set to 0.2× the minimum boundary layer thickness, the stretching factor is set to 1.2 (a 20% increase in size from one element to the next), and the number of layers is set to eight elements. The boundary layer mesh, in this case, is approximately 3.3× the length of the minimum boundary layer thickness.

Figure 15 shows the mesh for the Thermoviscous Acoustics model in the vicinity of the boundary layer. Note that it includes a boundary layer mesh along the bottom boundary. A sensitivity was performed for this example and it was shown that the dissipation effect along this boundary is extremely small, but it was retained, in general, to account for minor corner effects where transverse flow may be present. This effect is negligible for longitudinal modes in long ports, the most relevant for sensor port analysis, but for transverse modes or different geometries, the effect may be more substantial. Since this frequency domain model encompasses a wide frequency range, there is a range of acoustic boundary layer thicknesses shown with the blue and green bars in figure 15. In this case, the minimum thickness is the viscous boundary layer at the maximum frequency (5,000 Hz) and the maximum thickness is the thermal boundary layer at the minimum frequency (2 Hz). The transition parameters within the Boundary Layers node can be adjusted to help obtain a smooth transition between the boundary layer and interior mesh. The overall mesh in this example comprises 31,992 quad elements and 32,751 mesh vertices. A mesh sensitivity study was performed showing that some coarsening is possible without producing discernable changes in results.

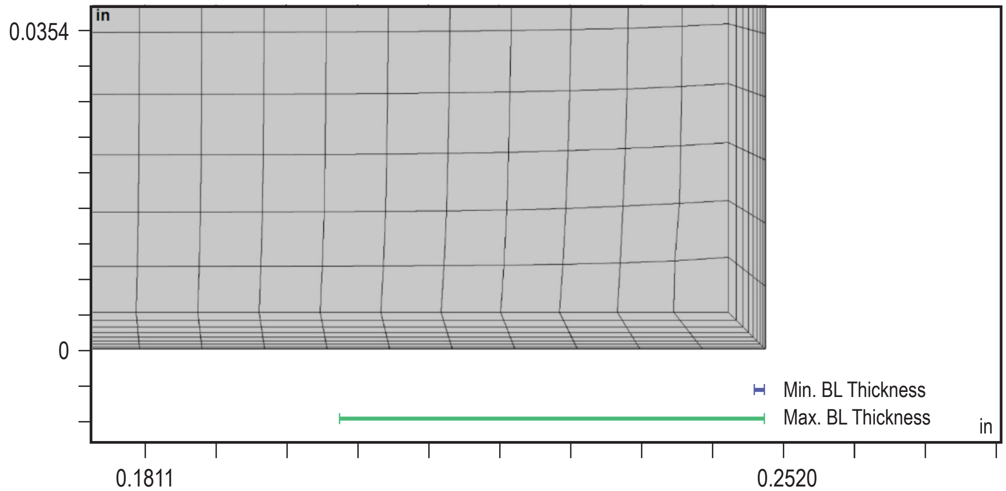

Figure 15. Mesh in the vicinity of the acoustic boundary layer. Blue and green bars show minimum and maximum boundary layer thicknesses, respectively (figure uses EE units).

Numerous other studies were performed to investigate various other sensitivities in this example. The following effects were shown to have a negligible or very small effect: (1) Adiabatic versus isothermal boundary condition at the driver boundary, (2) mesh element quads versus triangles, (3) refining the mesh an order of magnitude, (4) increasing the time resolution, (5) choice of numerical algorithm, (6) increasing significantly the mesh resolution along the driver boundary, and (7) applying boundary layer elements to all walls versus applying the elements to the wall with an acoustic boundary layer. A sensitivity of the driver amplitude is also important to understand in the Multiphysics model to ensure that the response is within the acoustic regime; the effects of nonlinear waves are discussed later in section 3.3.6. The overall mesh of the Multiphysics model includes 8,946 elements and 5,740 mesh vertices with tri elements in the interior and quad elements for the boundary layer.

Since the Multiphysics model is simulated within the time domain, there are several additional considerations. The primary consideration is an appropriate solver such as the Generalized alpha time-stepping method to minimize numerical damping and to also ensure stationarity is reached. Other solvers such as the implicit Backward Differentiation Formula (BDF) solver, while much more stable, will introduce damping that especially affects the results for low amplitude oscillations. For the acoustic-amplitude problems, 50 periods was a long enough duration to reach stationarity where the peak amplitudes no longer change. However, longer durations may be necessary for problems with nonlinear amplitudes. Additionally, a ramped start is used to help prevent numerical issues associated with simulation start. The ramp simply begins at a value of 0, has a slope equal to the inverse of the period, and is cut off at a value of 1; it also maintains smooth transition zones. This ramp function is a short duration about the duration of a single period and is multiplied by the sinusoidal wall velocity. Another beneficial feature to minimize numerical damping is to unselect the diffusion terms in both the Laminar Flow and Heat Transfer in Fluids interfaces. Also, the Fully Coupled solver setting should be used to ensure the equations are computed together. Finally, the default damped Newton's method solver uses a constant damping parameter (where the default actually has no damping) and is adequate for acoustics. These considerations are the baseline for the following analysis and is adequate to prevent convergence errors for the acoustics models.

In the Multiphysics model example, the solver takes time steps that are 60× shorter than a single period. Figure 16 shows that a resolution of 60× shorter than the period was necessary to resolve the solution to within less than 1% of the limiting solution (where the limiting amplification factor of 62.38 at 676 Hz is based on a resolution of 1,000× shorter than the period). At this resolution, there are diminishing returns on accuracy. The computational resolution necessary to resolve an accurate amplitude should not be confused with the Nyquist-Shannon sampling theorem where a sufficient sampling rate of more than two samples per period is required to capture all the information from a continuous time signal. While the Nyquist criterion is required to extract the given amplitude correctly, computational methods require much higher resolution so that the equations can be resolved accurately. Sensitives should always be done any time changes are made including those associated with the numerical algorithm or problem physics. While time steps are computed at 60× shorter than a period, the data are output at a resolution of 25× shorter than the period. This output rate was simply chosen so that smooth sinusoidal curves can be plotted in the time domain, any nonsinusoidal behavior could be observed, it produces a reasonable resolution for time domain-based instantaneous frequency and amplitude tracking, and file size was manageable.

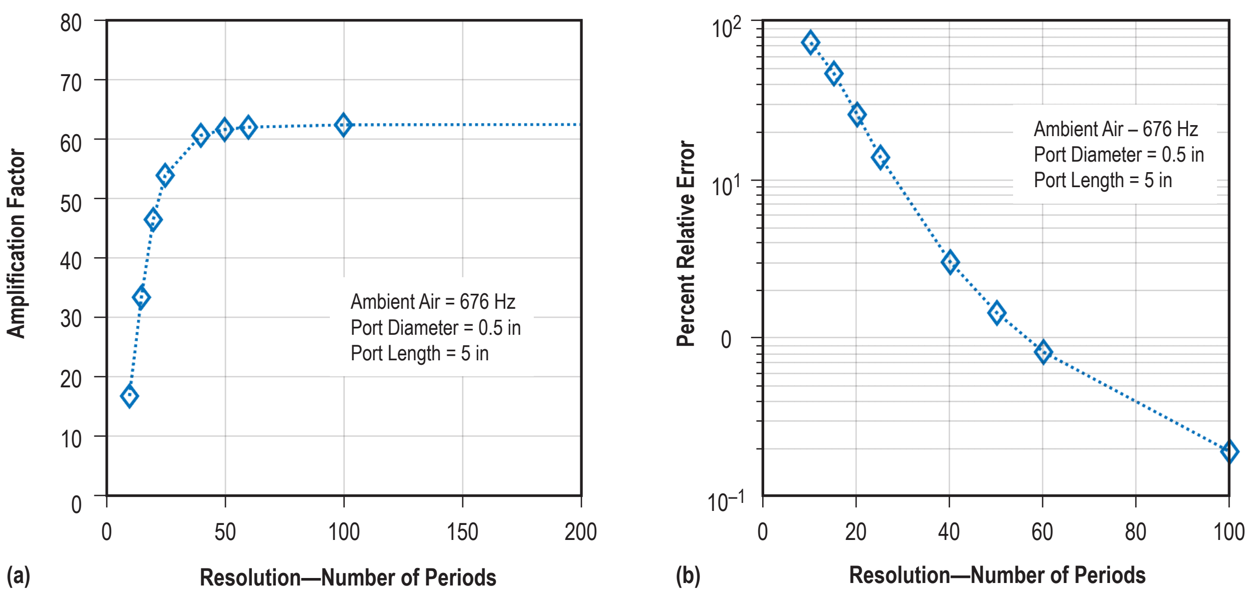

Figure 16. Time-stepping resolution sensitivity: (a) Example amplification factor at resonance and (b) percent relative error.

3.3.4 Comparison of Numerical and Analytical Solution

A comparison between the numerical COMSOL solutions (except the Multiphysics solutions) and analytical solutions are shown in figure 17. The response curve of each shows that, in general, all of the models produce similar results for this example case.

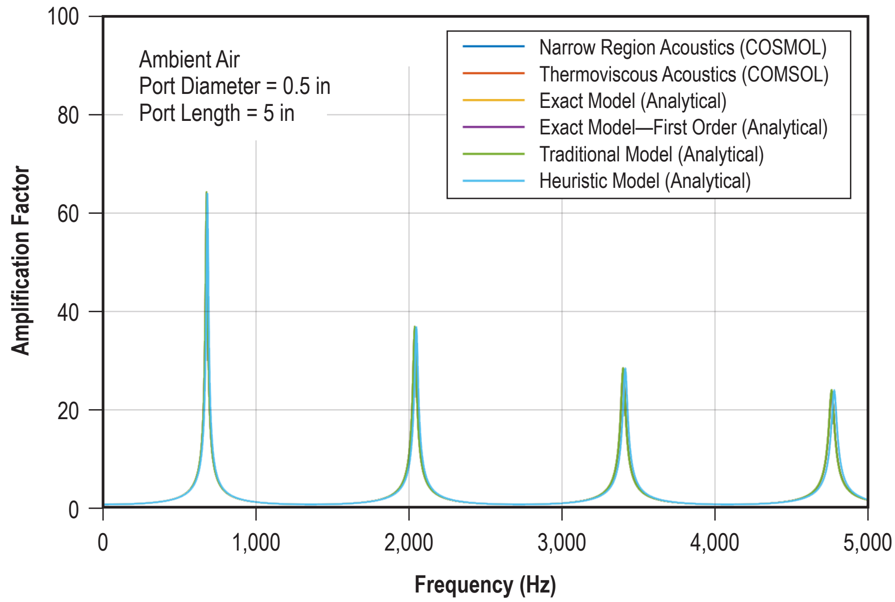

Figure 17. Thermoviscous response for a sensor port—frequency domain models

A detailed zoomed-in view of the fundamental mode is shown in figure 18 for the analytical models (Narrow Region Acoustics computational model is included for comparison) and figure 19 for the computational models.

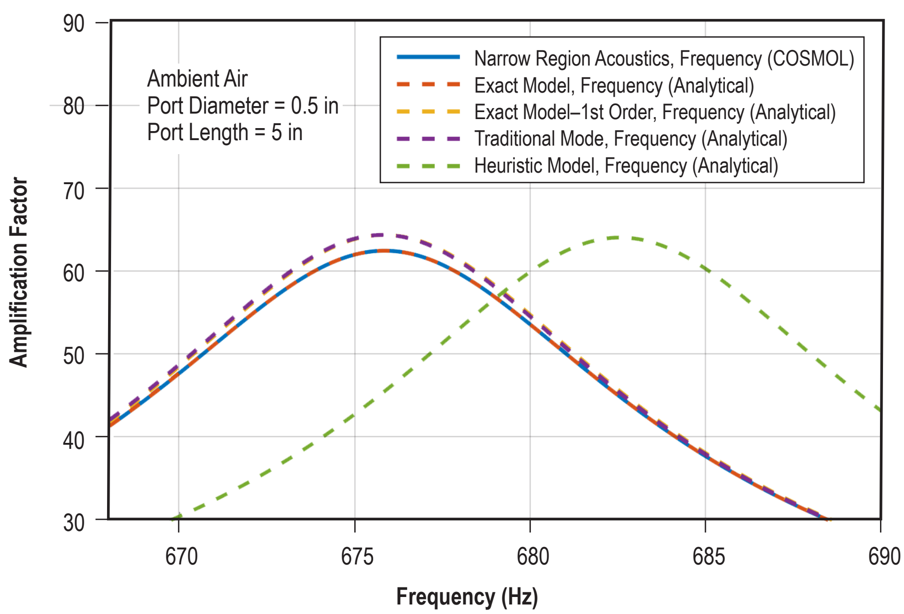

Figure 18. Thermoviscous response for a sensor port—analytical models, detailed view.

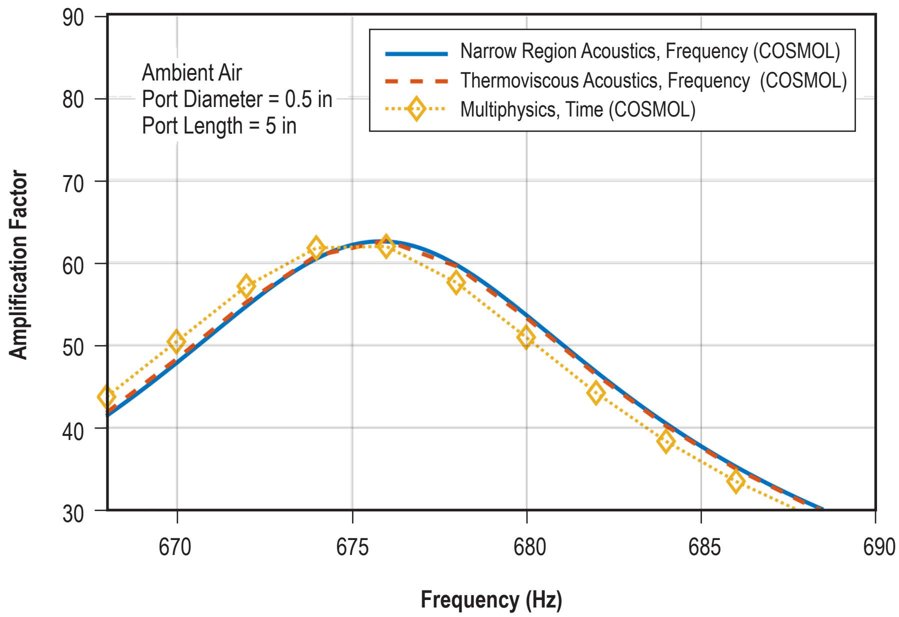

Figure 19. Thermoviscous response for a sensor port—computational models, detailed view.

Figure 18 shows that the COMSOL Narrow Region Acoustics computational model and the analytical Exact model overlay exactly as expected since they both use an equivalent propagation constant. The Exact model with First-Order Approximation is very similar to the Traditional model. This is expected since the propagation constant between these models has only a small difference in phase speed. The gain for these models has a noticeable error when compared to the Exact model, though, and is associated with limiting the series expansion of the propagation constant to first order. This error is also present in the Heuristic model. Additionally, the physics associated with the Heuristic model does not capture the appropriate thermoviscous boundary layer phase velocity and the error in frequency is evident.

The computational models are compared in figure 19. The Narrow Region Acoustics model and the Thermoviscous Acoustics model compare very closely. However, there is a small but noticeable difference between the Multiphysics model and the other computational models. The Multiphysics model incorporates the most complete set of equations that describe the thermoviscous acoustics phenomena, i.e., solving the Navier-Stokes equations and an energy balance directly, and accounts for additional influences including corner effects and, since it is not linearized, accurate fluid properties for variations in state. In the Multiphysics model, the sinusoidal velocity driver has a peak amplitude of 3.28×10^{-5} ft/s (1×10^{-5} m/s), which is well within the acoustic regime as discussed later in section 3.3.6. Appendix L discusses the method used in extracting the amplitude values from the Multiphysics model time domain data. The Multiphysics model, while more computationally intensive, has a major advantage in that it can serve as a point of departure so more complex influences can be studied and understood, such as high-amplitude waves, considerations for liquids, and flow effects.

It has been observed that there is a larger error in amplification for shorter sensor ports (ports with larger aspect ratios) when using analytical models and the Narrow Region Acoustics model. While it is expected that the Thermoviscous Acoustics and Multiphysics models are more accurate, a systematic study has not been performed to investigate this particular error in amplification. The analytical models and the Narrow Region Acoustics model produce a lower amount of damping than the more accurate models for these shorter port cases. There is also a similar small shift in frequency observed in the Multiphysics model when compared to the Thermoviscous Acoustics model as seen in figure 19. The acoustic radiation effects for shorter sensor ports are understood where the radiation damping becomes dominant over the thermoviscous damping; however, possible causes to an increased thermoviscous damping for shorter ports could be related to transverse flow near corners or other nonuniform unsteady flow effects.

The absorption coefficient of a simple cylindrical port can be extracted using COMSOL simply by using equations (14) and (29) to obtain equation (78) where $\hat{p}$ is the complex total acoustic pressure and the subscripts refer to the locations:

$$\alpha_{\text{port}} = \Re\left[\frac{1}{L}\operatorname{sech}^{-1}\left(\frac{\hat{p}_{\text{back}}}{\hat{p}_{\text{inlet}}}\right)\right] . \tag{78}$$

Figure 20 shows a comparison of the absorption coefficients using several COMSOL and analytical models over a wide bandwidth and a detailed view near the resonant frequency. Note that for the numerical models, the absorption coefficient is the overall effective absorption coefficient for the model obtained using equations (13) and (14), and not the same as the analytical absorption coefficient, e.g., such as equation (46). There could be additional effects that are not necessarily captured in the analytic models. It should also be noted that the Thermoviscous Acoustics model does not reproduce the nonresonant sinusoidal effect on the absorption coefficient as proposed in reference 21 and implemented in an example in reference 9. This effect should not be included in thermoviscous analytic models. The Narrow Region Acoustics model compares identically with the Exact model as expected; however, there is a clear difference between these and the Traditional model. There is also a small difference observed in the more accurate Thermoviscous computational model.

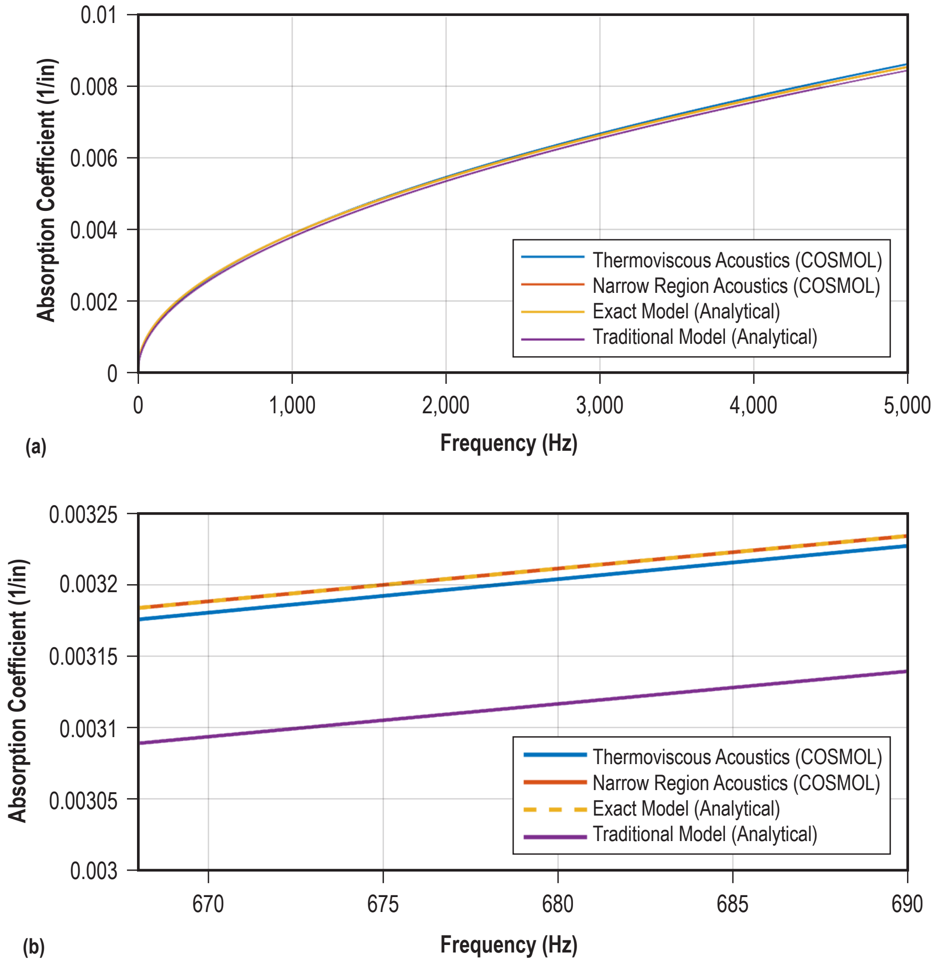

Figure 20. Absorption coefficient comparison: (a) Full bandwidth and (b) zoomed-in view (figure uses EE units).

The phase speed of the port, though, cannot be extracted directly using the arcsech function because it is restricted to the principal branch, which is $-\pi$ to π on the imaginary axis. This restriction results in branch cut discontinuities in the arcsech function.

As a final thermoviscous analysis, the viscous and thermal boundary layers are plotted at the port midpoint location (at 2.5 in). Figure 21 shows a zoomed-in view of the boundary layers near the port wall (at 0.25 in) showing acoustic velocity and temperature perturbations. The boundary layers are plotted every 1.18×10^{-4} s for 13 time steps, which is just over a full cycle at 676 Hz (the fundamental frequency). A similar plot showing the viscous boundary layer is described in reference 2, p. 230. The oscillatory boundary layers are produced due to the frictional shear force that is exerted on the fluid and the heat transfer that takes place between the fluid and surface.[1, p. 322] Viscous and thermal losses are present when there are gradients in the velocity field and temperature, respectively, as described in appendix C by the viscous shear diffusive loss terms in the momentum equation, equation (133), and thermal conduction diffusive loss term in the energy equation, equation (134).[17] The transition to the no-slip and isothermal conditions at the wall therefore produces the acoustic boundary layers as the fluctuations move through the port.[17]

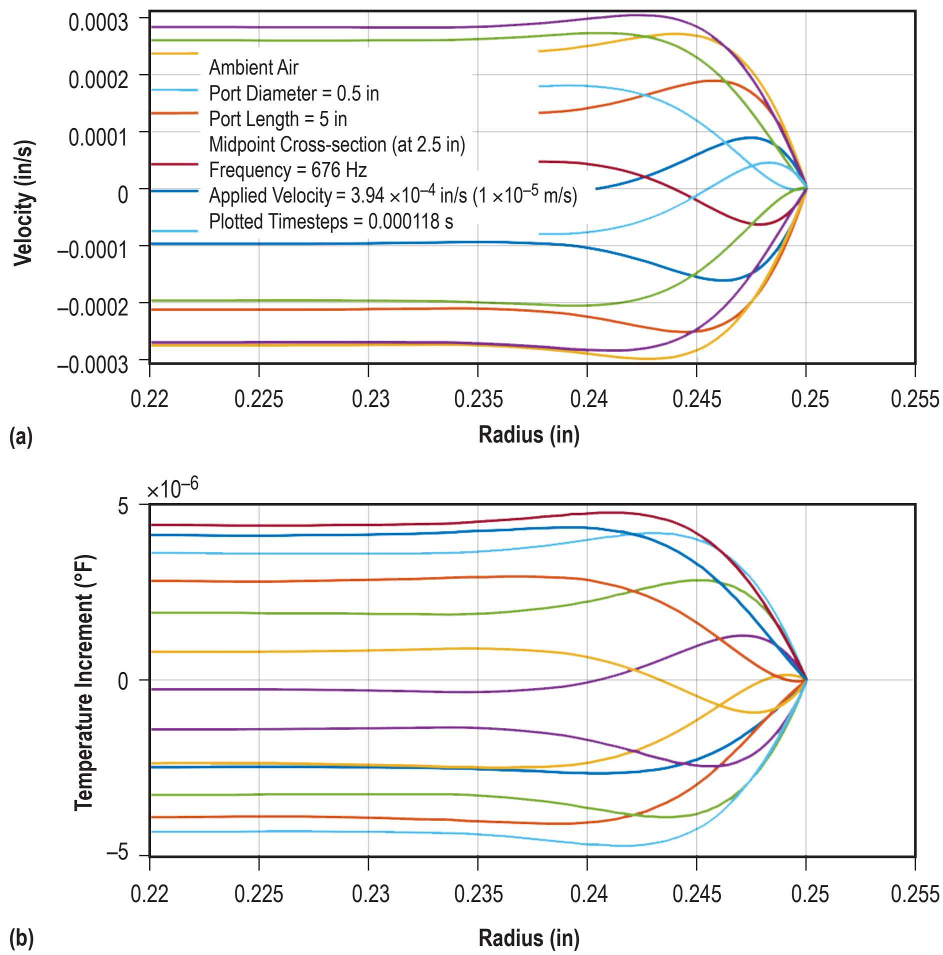

Figure 21. Boundary layers over one cycle: (a) Viscous and (b) thermal (figure uses EE units).

3.3.5 Modeling Liquids

In this section, a simple study is performed to examine any characteristics that may be important in modeling liquids. It has been noted that the absorption coefficient falls short in most common liquids.[2, p.218] To examine the damping characteristics of a liquid, simulation comparisons are made between the Narrow Region Acoustics, Thermoviscous Acoustics, Multiphysics, and analytic models. The Multiphysics model is the most complete model and contains all the relevant physics.

The response associated with a port of radius 0.25 in (0.00635 m) and length of 5 in (0.127 m) is numerically studied in ambient water at a temperature of 77 °F (298.15 K). Similar to the previous air simulations, the water density is described by a fourth-order constitutive equation of state as a function of pressure and temperature that is fit to real data from the REFPROP software.[20] Also similar to the approach used for air, for an equal comparison of the linearized models, the equilibrium sound speed is evaluated from the Thermoviscous Acoustics model solution, and then specified in the Narrow Region Acoustics model. The analytical models also similarly require additional fluid property inputs; for an equal comparison, all properties are evaluated directly from the Thermoviscous Acoustics model solution.

The traditional form of absorption coefficient, equation (46), contains the isentropic expansion factor, or specific heat ratio. This factor is an important characteristic related to the absorption due to heat transfer. An acoustic wave induces an adiabatic compression, in which the heat of the compression does not have enough time to escape the pressure pulse, and thus contributes to the pressure induced by the compression. For liquids, this contribution is small as $\gamma \to 1$ for both intrinsic[1, p. 313] and boundary layer absorption. However, studies have been performed where the parameter of nonlinearity,[2, p. 116; 22, pp. 25–29] represented as a ratio of coefficients, *B*/*A*, is substituted into the absorption coefficient equations. The parameter of nonlinearity substitution is achieved by replacing the specific heat ratio with a coefficient (also γ) using the following definition for an arbitrary fluid, $\gamma \equiv 1 + B/A$.[2, p. 116] The coefficient γ is effectively an empirical constant whose difference from unity measures the nonlinear relationship between acoustic pressure and acoustic density.[2, p. 116] For a perfect gas, the coefficient γ is equal to the specific heat ratio and $B/A = \gamma - 1$ (where γ in this equation is the specific heat ratio). Therefore, in a perfect gas, the absorption coefficients remain unchanged. However, for a liquid, the coefficient γ results in a higher value than the liquid specific heat ratio.[2, p. 116] Using the parameter of nonlinearity in an analytical model would therefore result in a higher damping associated with the thermal contribution. While the parameter is relevant to second order, weakly thermoviscous equations,[22, pp. 50–52] it is very important to note that reference 22, p. 52, shows that the typical application for the parameter of nonlinearity excludes the thermoviscous boundary layers and therefore would not apply in sensor port analysis. However, to understand any influence from higher order thermoviscous effects, analytical solutions with and without the parameter of nonlinearity are compared to the computational models.

The parameter of nonlinearity is a second-order correction,[2, p. 479; 22, pp. 26–27, 53] and as noted earlier, the COMSOL material property or constitutive equation of state is expanded to fourth order as a function of pressure and temperature, $\rho(p,T)$, by fitting real property data with a fourth order, least-square fit. This ensures that the higher-order thermoviscous effects are incorporated in the numerical analysis.

The same mesh and domain considerations were made as described previously in sections 3.3.2 and 3.3.3.

Figure 22 shows the comparisons of the Exact analytical model using the equation (51) propagation constant and the Narrow Region Acoustics computational model. For the analytical model without the parameter of nonlinearity, equation (46) is used directly in calculation of the equation (51) propagation constant. For the analytical model with the parameter of nonlinearity, $\gamma \equiv 1 + B/A$ is substituted into equation (46) first before calculation of the equation (51) propagation constant. Property data from REFPROP[20] is used to calculate the parameter of nonlinearity, $B/A = 5.0744$, using the equation for B/A described in reference 22, p. 27, equation (8). The Narrow Region Acoustics computational model is included in figure 22 to make a direct comparison to the computational models shown in figure 23.

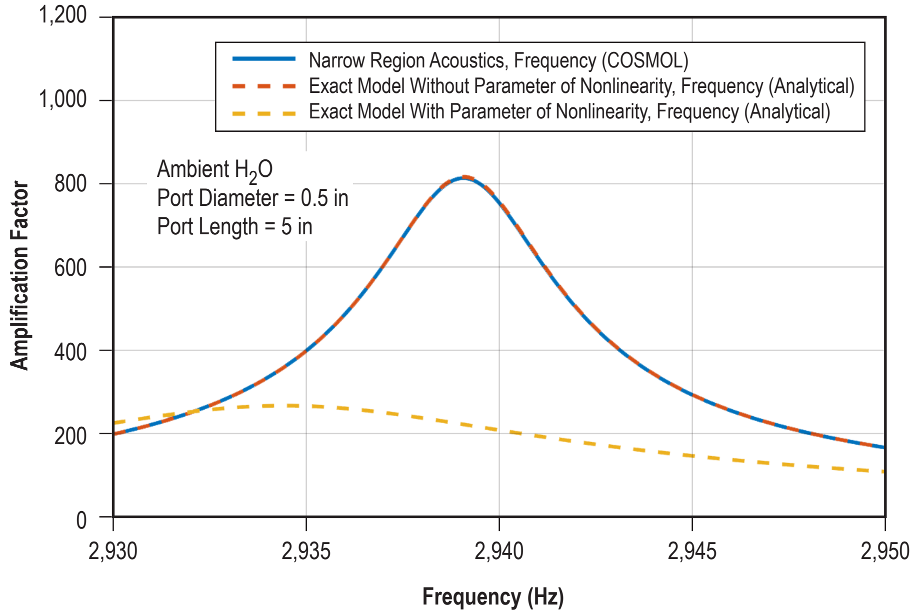

Figure 22. Thermoviscous response of liquid water—analytical models.

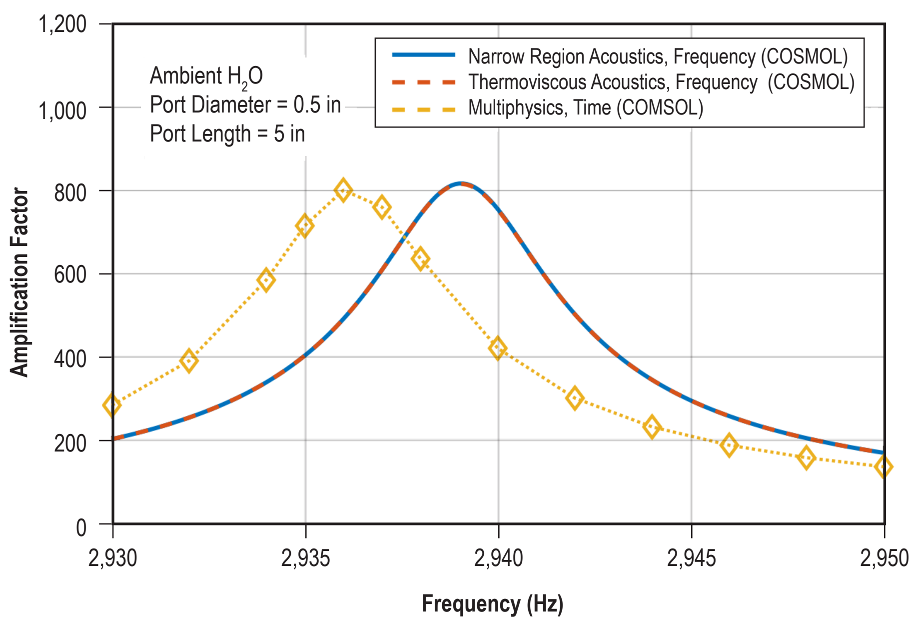

Figure 23. Thermoviscous response of liquid water—computational models.

The initial observation from figure 22 is that the parameter of nonlinearity has the effect of producing a substantial amount of damping. However, by examining figure 23, it is clear that it is inaccurate to use the parameter of nonlinearity in an analytical model, as the Multiphysics model does not show any dominant higher-order thermoviscous effects in the amount of damping. The

Multiphysics model does show a very small amount of additional damping compared to the other computational models, and a similar shift in frequency as was observed in the air Multiphysics simulation. A systematic study has not been done, but causes of these observations could be related to various effects including fluid properties for variations in state, transverse corner flow effects, or even higher-order thermoviscous effects.

While only water was studied in this example, it is recommended that equation (46) not be modified with the parameter of nonlinearity for analysis of liquids in sensor ports.

3.3.6 Modeling Thermoviscous Effects of Nonlinear Amplitudes

The example configuration in sections 3.3.1 through 3.3.4 was focused on the thermoviscous response from an acoustic wave. In this section, nonlinear or finite-amplitude waves are studied; however, the same example configuration is examined. For an unsteady oscillation, the small-signal approximation is satisfied with the following restrictions on acoustic pressure and particle velocity given in equations (79) and (80), respectively:[1, p. 36]

$$|p| \ll \bar{\rho}\bar{c}^2 \tag{79}$$

and

$$|u| \ll \bar{c}\ . \tag{80}$$

For air at the conditions in this example, the acoustic pressure and particle velocity amplitude must be much less than 20.6 psi (142,032 Pa) or 1,135 ft/s (346 m/s) to satisfy the small-signal approximation. These values seem large; however, considering that the ‘much less than’ inequality implies several orders of magnitude, an acoustic oscillation in air can be approximated roughly with less than 2 orders of magnitude or at no more than 0.2 psi and 11.4 ft/s (3.5 m/s). In this example, the response for three cases are compared. In the three cases, the sinusoidal velocity driver has a peak amplitude of 3.94×10^{-4} in/s (1×10^{-5} m/s), 196.85 in/s (5 m/s), and 393.70 in/s (10 m/s). The maximum peak pressure in these cases reaches a value of 5.95×10^{-7} psi (4.1×10^{-3} Pa), 0.331 psi (2,279 Pa), and 0.851 psi (5,866 Pa), respectively, at 676 Hz. It is observed that the highest amplitude case maintains a clear waveform distortion where the minimum pressure of the waveform only achieves a magnitude of 0.613 psi (4,229 Pa).

For nonlinear problems, numerical convergence can be more difficult. Additional solver characteristics may need to be considered. As noted earlier, the default damped Newton’s method solver uses a constant damping parameter method (where the baseline approach has no damping) and is adequate to prevent convergence errors for the acoustics models. Unfortunately, for nonlinear waves, this method may often be unsuccessful. One alternative is to use the automatic damped Newton’s method solver. This solver automatically determines a needed damping factor for every iteration to aid in resolving a root. In the examples studied, this increases the solution time substantially to over 20× longer than the baseline Multiphysics acoustics model described in section 3.3.3, but is often the only necessary step in resolving the solution. This method was used in providing solutions to nonlinear problems and verified by comparing results for the acoustics model. Another alternative is to use the baseline Multiphysics acoustics approach, but modifying the Jacobian update. By default, when using the baseline approach, the Jacobian is reused a minimal number of times whenever deemed possible; however, forcing the Jacobian to be computed once per time step or every iteration can also help overall convergence. These modifications also substantially increase solution time to over 20× and 40× longer than the baseline approach, respectively. As discussed in section 3.3.3, the generalized alpha time stepping is recommended for acoustics problems, and the BDF time-stepping solver is not recommended for acoustics problems since it may introduce a significant amount of damping into the results. In any case, a sensitivity analysis to understand the influence of the solver should always be performed. One verification approach is simply to ensure the acoustic solution is resolved correctly with a particular solver by comparing to the theoretical solution before attempting to use the solver in a nonlinear problem. Additionally, it may take longer to reach stationarity in the nonlinear problems where the peak amplitudes no longer change. In the current examples, this usually required a duration of approximately 100 periods, but at times required up to 400 periods.

Because nonlinearities may include harmonics and other nonlinear modulations through the complete spectrum, additional considerations must be made for the time-stepping solver and mesh. A sensitivity showed that the solver time steps should be at least 60× smaller than a single period for accurate amplitude resolution. This is also the recommended resolution by COMSOL. Depending on the amplitude level within the domain, a number of harmonics may be desired for an accurate representation of the nonlinear waveform. For the nonlinear example here, the fundamental and nine additional harmonics are desired. Ten total harmonic modes is adequate for an overall amplitude comparison as there is a progressive reduction in amplitude for higher harmonics. The example configuration in section 3.3.1 resulted in a peak amplitude at 676 Hz for air shown previously in figure 19. In the 676 Hz case with the additional harmonics, the highest frequency of interest is 6,760 Hz. With the highest frequency of interest equal to 10× the fundamental and considering the Nyquist frequency for data processing, a minimum output sampling rate of 20× shorter than the fundamental period is required. In addition, to accurately represent the amplitude at 10× the fundamental frequency, a time step of 60× shorter than the period of the highest frequency (6,760 Hz) is needed as noted earlier, which equates to a computational time step that is 600× shorter than the fundamental period (676 Hz). As discussed in section 3.3.3, this ensures the amplitude at the highest frequency can be resolved accurately. While the output sampling rate is given as a minimum needed for data processing to best manage file size, the computational time step must be much more resolved. This analysis is a prudent step; however, a sensitivity should always be done to ensure amplitude resolution.

To accurately account for this full bandwidth, the boundary layer thickness should be calculated at the maximum desired frequency, which is 6,760 Hz in the example. This ensures the smallest boundary layer is captured as discussed in section 3.3.3. Since the first layer is based on the boundary layer thickness, i.e., 0.2× the minimum boundary layer thickness in the example, the first layer will be smaller at the higher frequency. Although, the most important boundary layer feature is that there are enough elements to capture details from the smallest boundary layer, it is desired—but probably not necessary—to have an even distribution (with constant stretching factor) for boundary layers over the full range of frequencies (from 690 Hz to 6,900 Hz). Equation (77) can be used to develop a relationship that estimates the number of layer elements needed that preserves the boundary layer mesh length of the fundamental frequency, but considers the smaller boundary layer thickness at the highest frequency of interest. The relationship is given as equation (81), noting the ceiling brackets, and developed in appendix M:

$$n_h = \left\lceil \ln\left(\frac{f_h}{f_l} \cdot \left(\left(S^{n_l} - 1 \right) + \sqrt{\frac{f_l}{f_h}} \right)^2 \right) \Big/ \ln\left(S^2 \right) \right\rceil . \tag{81}$$

The subscripts *l* and *h* refer to the lower and higher frequency mesh parameters, respectively.

While 8 layers are used to obtain an initial boundary layer mesh for 676 Hz (which is approximately 3.3× the length of the minimum boundary layer thickness), equation (81) can be used to show that 14 layers are needed to obtain at least the same boundary layer length for 6,760 Hz when using the smaller initial layer thickness. This does increase the size of the overall mesh from the Multiphysics example in section 3.3.3, but it also produces a smooth transition over the full range of minimum boundary layer thicknesses. The overall mesh of this example includes 10,470 elements and 7,270 mesh vertices with tri elements in the interior and quad elements for the boundary layer.

A comparison showing the acoustic response and the two other finite-amplitude responses are shown in figure 24. This shows a clear damping effect with increased oscillation amplitude. Additionally, a peculiar response is evident in the response of the largest oscillation amplitude near 680 and 684 Hz. Further simulations were performed to help resolve the characteristics of the response near this bandwidth. This secondary resonance, which actually exceeds the primary resonance in amplification for the 393.70 in/s (10 m/s) case, is also noticeable in the 196.85 in/s (5 m/s) response case as a slight bulging in the same frequency range. It is not clear as to the cause of this nonlinear effect, although there are several additional factors that could play a role such as transverse flow near corners, finite-amplitude wave propagation speed and characteristics, or separate propagation regimes within the central region and near the boundary region.[22, pp. 44–47; 23, pp. 285–297] The complexity of the corner effects can be explored by examining the velocity vector field near the back corner of the port shown in figure 25. This particular velocity field snapshot occurs at a timestamp in the 100th period at time 0.14564 s for the 393.70 in/s (10 m/s) model at a driven frequency of 682.5 Hz. The pressure traces are the spatial average pressure across the inlet and across the back of the port. The waveform distortion, described earlier, can be readily observed in the figure. Note that the peak-to-peak amplitude at the driver location is only 2.5× the peak-to-peak amplitude at the back location. Because the amplitude of the harmonics are substantial and do not always fall on a resonance where the amplification factor can be near 1×, there can be significant contribution to the overall amplitude at both the driver and back locations.

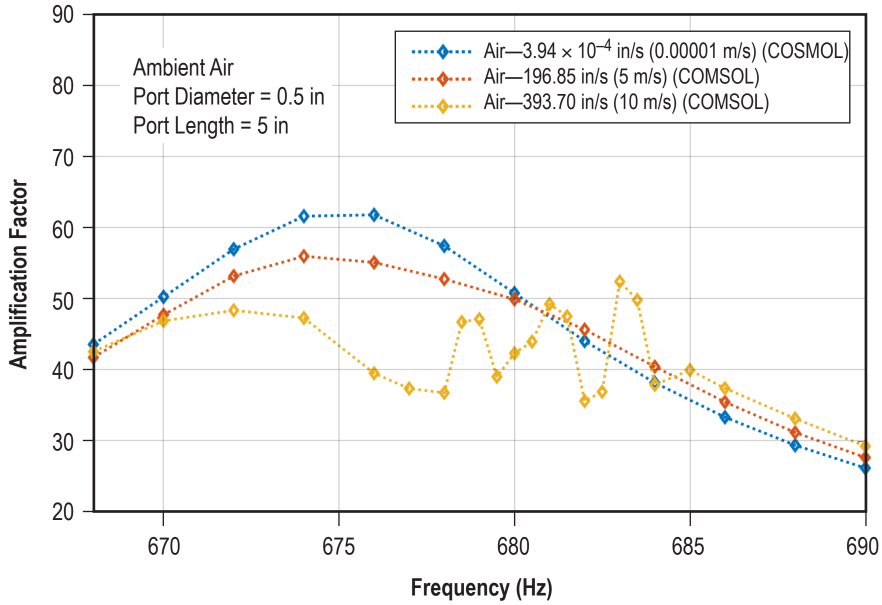

Figure 24. Thermoviscous response—nonlinear amplitude effects.

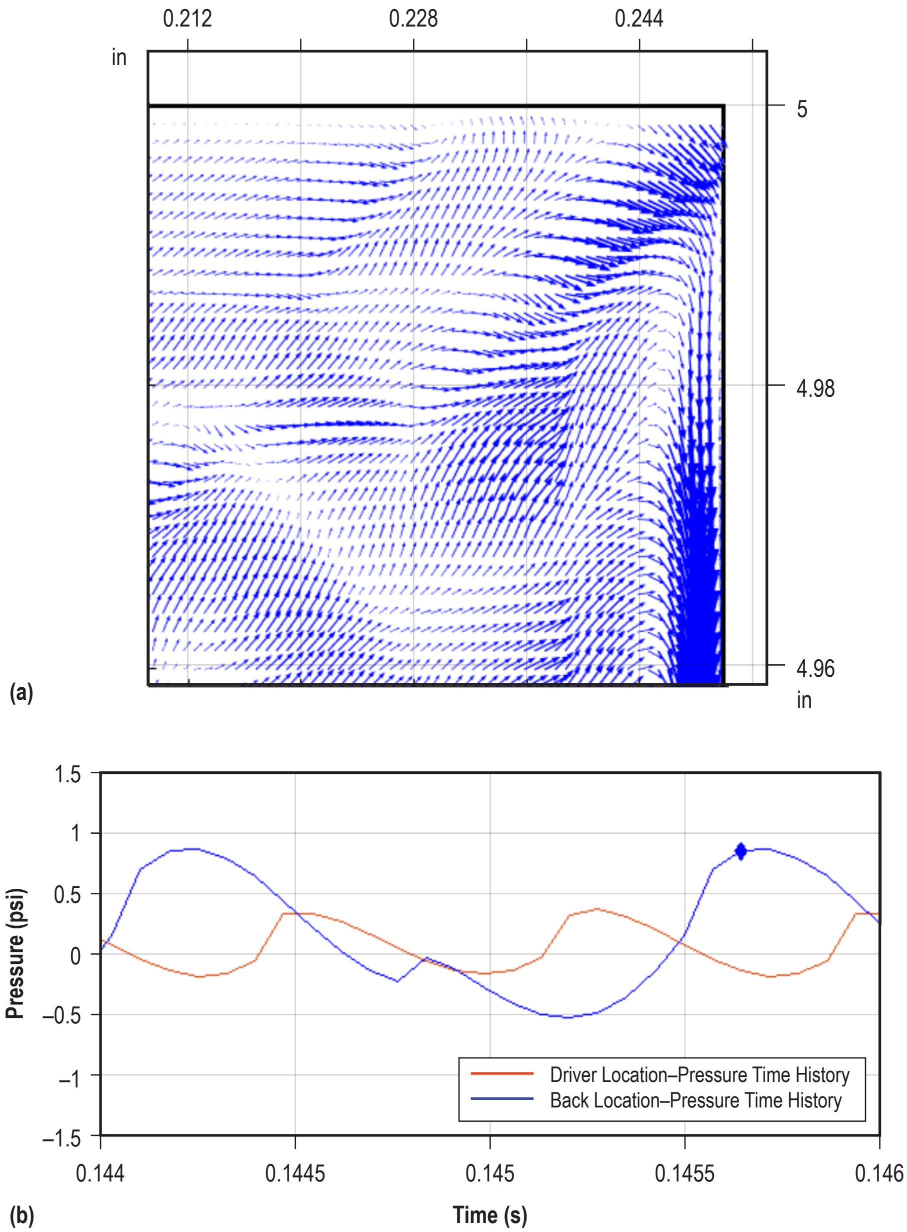

Figure 25. Sensor port is 5 in long and 0.25 in radius: (a) Velocity vector field in back corner at an instant and (b) nonlinear amplitude simulation pressure time history—marker shows instant (figure uses EE units).

The effects of an isothermal boundary condition at the acoustic driver location were explored at a frequency of 681 Hz. The influence of an isothermal boundary condition compared to the adiabatic boundary condition was extremely small.

3.4 Sensor Port Model

Two very important physical mechanisms are considered to model the acoustics in a sensor port. The radiation acoustics at the port opening and the thermoviscous dissipation along the walls of the port are studied in the previous two sections (secs. 3.2 and 3.3). In this section, a simple sensor port is modeled numerically in COMSOL and analytically using the framework described in section 2.3.3.

The sensor port model can be studied numerically using the COMSOL Pressure Acoustics, Frequency Domain interface. As noted in section 3.2, this interface is suited to model pressure variations for the propagation of acoustic waves in fluids at quiescent background conditions.[17] For the thermoviscous effects, the COMSOL Narrow Region Acoustics node is used rather than using the COMSOL Thermoviscous Acoustics interface. The error in using this thermoviscous model was shown previously to be very small and saves a large computational expense.

For comparisons to the numerical solution, the wave equation is solved analytically using an appropriate propagation constant for the thermoviscous dissipation and for the radiation acoustics. The two-line model, equation (37), is used so that both the propagation constant in the port, equation (51), and in the radiation acoustics region, equation (73), can be incorporated. The characteristic impedance used in the model is from equation (22). The thermoviscous effects are modeled over the length of the port and the radiation effects are modeled over the length of the end correction. Combining both effects in this manner results in a very accurate acoustic port response solution.

3.4.1 Example Sensor Port

An example using the COMSOL pressure acoustics model is described first and then compared to the analytical solution. The response associated with a port of radius 0.25 in (0.00635 m) and length of 1 in (0.0254 m) is studied in ambient air. The shorter length compared to previous examples is used to emphasize the effects of acoustic radiation. The air is at a temperature of 77 °F (298.15 K). The properties listed in table 2 are used for an equal comparison of the sensor port model computational and analytical models. While the resolution of the tabulated values seems excessive, small differences can produce minor but observable variances. The domain and mesh configuration is based on the previously verified piston function and thermoviscous models in sections 3.2 and 3.3, respectively.

Table 2. Properties for sensor port example (note units are SI).

Property	Units	Value
Dynamic viscosity	Pa • s	$1.838544078 \times 10^{-5}$
Specific heat ratio	–	1.399375426
Heat capacity at constant pressure	J/(kg • K)	1005.630524639
Density	kg/m^3	1.184121471
Thermal conductivity	W/(m • K)	0.026162083
Speed of sound	m/s	346.040793864

Similar to the flanged circular piston example described in section 3.2, the total domain radius is 7.5 in (0.1905 m), which is 30× the port radius, and includes a 0.375-in- (0.009525-m-) thick PML that behaves as an absorptive boundary. A grid refinement region is also defined at 10× the port radius near the far-field transition radius. The analysis is explored over the bandwidth through 10,000 Hz by increments of 1 Hz. The minimum wavelength of interest is therefore 1.3632 in (at 10,000 Hz).

3.4.2 Domain Setup

Figure 26 shows the baseline domain setup for modeling a sensor port. As discussed in section 3.1, an advantage of numerical analysis is that a direct comparison can easily be made by comparing solutions of the exact configuration with a sensor port and the desired configuration with no sensor port. A secondary domain consists of the exact same configuration except no sensor port. To automate this using COMSOL, a Parametric Sweep node can be added to the COMSOL Study.

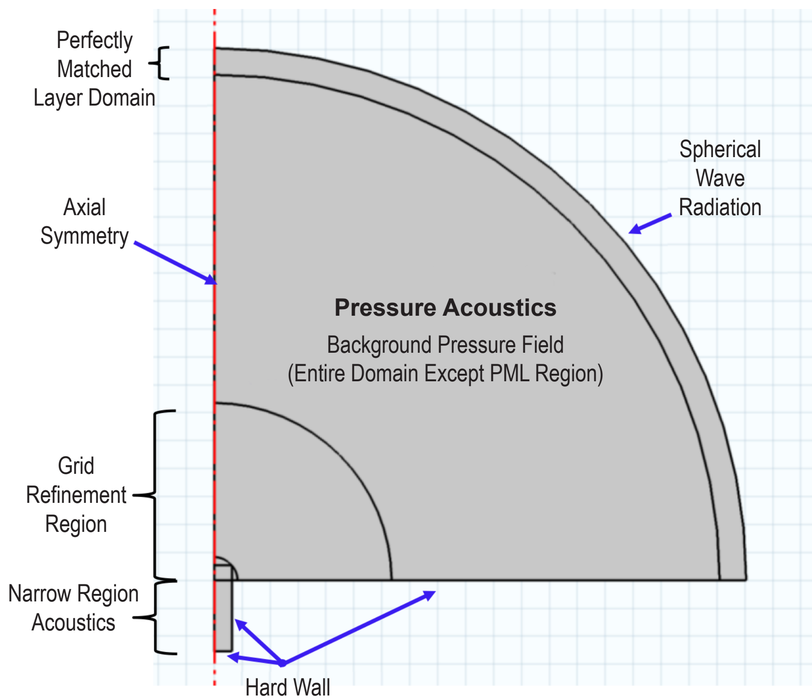

Figure 26. Modeling sensor port response—2-D axisymmetric baseline domain setup.

In the parametric sweep, the response is calculated without the port first and then subsequently with the port. This is performed in COMSOL within the Parametric Sweep node by varying the value of the port length parameter where the baseline length could be specified in the Parameters node.

The domain setup is very similar to the previous configuration from figure 9 shown in section 3.2.2. There is the additional port region where the Narrow Region Acoustics node is applied. In addition, another arc is defined at a radius equal to $R \cdot \sqrt{\frac{64}{9\pi^2}+1}$ based on equation (2) that encompasses the end correction entirely.

Finally, rather than driving a piston as in section 3.2.2, the port is simulated to be in the presence of a background acoustic field. To eliminate any directional dependence, a diffuse field can be created in the simulation. Note that COMSOL uses the scattered field formulation where the total acoustic pressure is the sum of the background acoustic pressure and the scattered acoustic pressure.[11, pp. 52–53, 75–76, 200–204] This formulation is convenient to study the effect of incident pressure waves and scattering problems. For the sensor port analysis, the Background Pressure Field node can be used to set an existing diffuse field by selecting a plane wave pressure field with a 0 unit vector. This simplifies the field such that it is spatially independent with a uniform sound pressure everywhere in the domain. For this linear analysis, the background acoustic pressure amplitude is set simply to 1 Pa. The total acoustic pressure field is the relevant acoustic variable for analysis, which is representative of a direct acoustic measurement in a sensor port configuration.

As a note in using COMSOL, the Parametric Sweep node allows the port length parameter to be varied by entering a list of values. For this sweep, the parameter values are simply 0 and the port length parameter value. To avoid geometric entities that have a 0 size, the port size is actually specified longer than the actual port by an additional length equal to the end correction, equation (2), overlapping into the plenum domain. Any additional length can be used to prevent a 0-size geometric entity; however, the end correction length is used so values at that location can be probed easily.

Additionally, it is useful to use the Geometry Programming node to provide if-then logic to help define the variation in geometry between the baseline and secondary domain. For example, in this example, the port is first defined as a rectangle Geometry node that includes the end correction, as just described. This allows the port to be varied from a range of 0 to the port length without producing 0-length errors. Following this definition, the if-then programming node is used to create another rectangle that is only the size of the port (without the end correction)—if the size of the port is not equal to zero. In this node, the new rectangle will be set to contribute to a Cumulative Selection. This process allows the Narrow Region Acoustics to be associated with the Cumulative Selection rather than the port domain. It is therefore not reset when the port geometry is set to a zero length. A Cumulative Selection is used also to help associate the full baseline and secondary domain with the Background Pressure Field and to associate point and boundary probes at the port entrance location.

3.4.3 Mesh Design

To ensure the physics were captured accurately, the model was first broken down into radiation acoustics described in section 3.2 and thermoviscous acoustics discussed in section 3.3. The mesh considerations discussed in sections 3.2.3 and 3.3.3 were applied here to ensure that these physics are captured accurately in the sensor port model. For simplicity, the mesh in the grid refinement region is extended into the port where the Narrow Region Acoustics node is applied.

3.4.4 Comparison of Numerical and Analytical Solution

In this section, the pressure transfer function is examined in the sensor port model and compared between the numerical and analytical solution. In general, the pressure amplification factor and relative phase are obtained from equations (10) and (11). Since the COMSOL simulation separately computes the complex pressure distribution for a case with the sensor port and a case without the sensor port, careful considerations must be made in computing the transfer function.

Computing the pressure amplification factor using the complex pressure from two separate simulations is straightforward. The complex total pressure is probed at the back of the sensor port (baseline domain with sensor port) and the projected location on the wall (secondary domain without sensor port) and ratioed as in equation (10). However, since the phase angle is not a measurement within a single simulation domain, a general form must be used to evaluate the relative phase angle between two complex numbers. Appendix N details this derivation. Equation (82) can be used to calculate the phase angle in the range $-\pi < \phi \leq \pi$, for complex vectors $\vec{a} = a_r + a_i i$ and $\vec{b} = b_r + b_i i$. The relative phase for the sensor port response can be computed by substituting the complex total acoustic pressure at the back of the sensor port (baseline domain with sensor port) and the projected location on the wall (secondary domain without the sensor port) into equation (82):

$$\phi = \tan2^{-1}\left(a_r b_i - a_i b_r,\ a_r b_r + a_i b_i\right) . \tag{82}$$

Figure 27 shows the comparison of the analytical model and numerical model. As noted earlier, equations (22), (37), (51), and (73) are used to plot the analytical solution while the numerical solution is obtained directly from COMSOL.

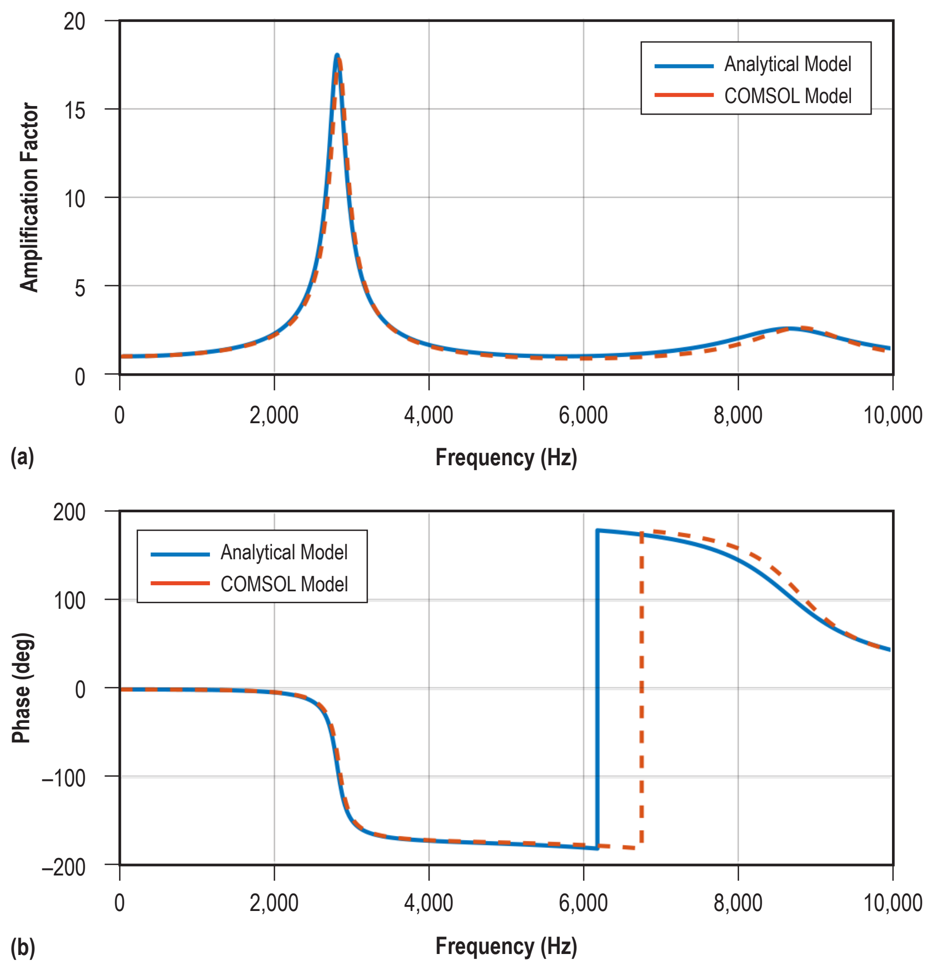

Figure 27. Sensor port response analytical and numerical comparison: (a) Amplification factor and (b) relative phase.

The results show a very good comparison and encompass the dissipation associated with both thermoviscous effects and radiation acoustics. A separate COMSOL simulation was also run considering just the thermoviscous effects in the port. A comparison of the senor port response to this solution would show the effect of attenuation associated with radiation acoustics. The resulting pressure amplification curve is not shown, however, the peak amplification is found as 142.3× at 3,391 Hz for the port configuration without radiation acoustics. This can also be estimated using equations (29) and (51).[9] The dramatic reduction in amplification due to radiation acoustics to a peak amplification of 17.8× at 2,834 Hz is observed in figure 27. This emphasizes the importance of including radiation acoustics in a sensor port frequency response model.

Figure 28 shows a zoomed-in view of the fundamental quarter-wave response. The small discrepancy observed between the analytical solution and numerical simulation is due to assumptions in the analytical model. Most likely, the largest error results from modeling radiation acoustics using the piston model, which assumes a uniformly distributed flow field at the port opening. The reality is that there is a complex flow field near the port opening; however, a uniform flow field is a good approximation.

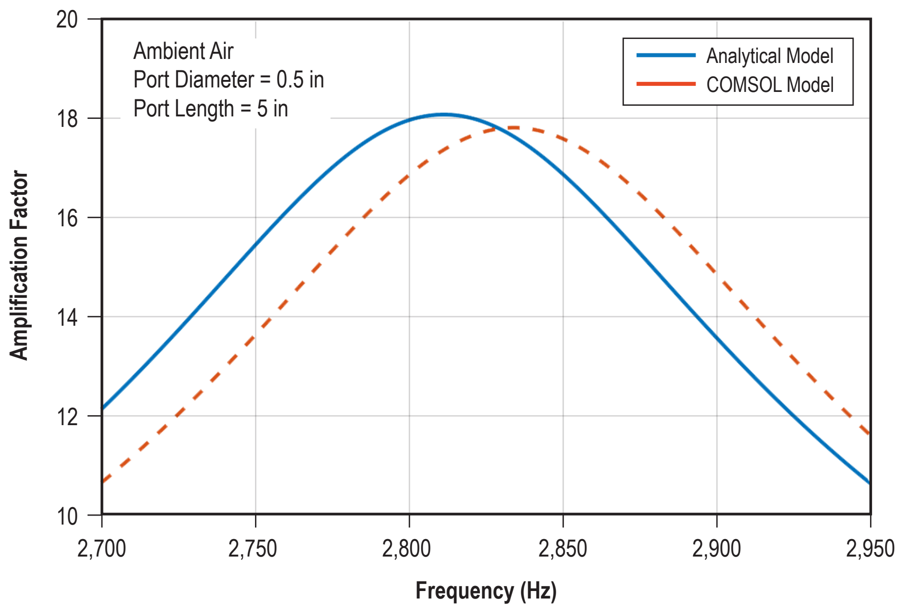

Figure 28. Sensor port response analytical and numerical comparison—zoomed.

Figure 29 shows a zoomed-in snapshot of the velocity vector field at the opening where the flange intersects the port. The snapshot is for the resonance condition at 2,834 Hz and it is clear that the instantaneous velocity field is not uniform across the entire opening. Recall that this particular simulation uses the Narrow Region Acoustics node where the dissipation is distributed evenly within the fluid, so boundary layers will not be evident in the velocity field. The boundary layer will further complicate the flow field at the opening.

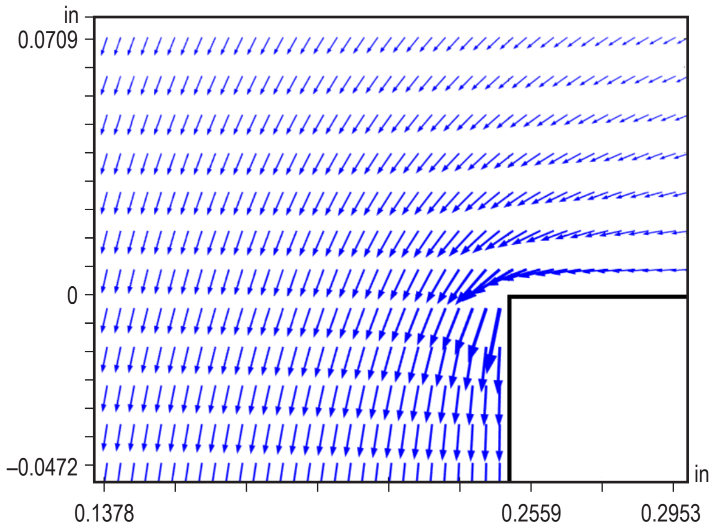

Figure 29. Velocity field at the opening (snapshot at resonance)—zoomed (figure uses EE units).

Figure 30 shows a contour plot of the total acoustic pressure field in and around the sensor port at the fundamental quarter-wave resonance (2,834 Hz) and the three-quarter-wave resonance (8,799 Hz). The pressure node lines for the quarter-wave mode are dark red and for the three-quarter-wave mode are light green. To discern the node line color, a simple gauge is to view the color in the plenum far from the port where the pressure response is effectively zero. The plots show the effect of the port opening on the spatial pressure field.

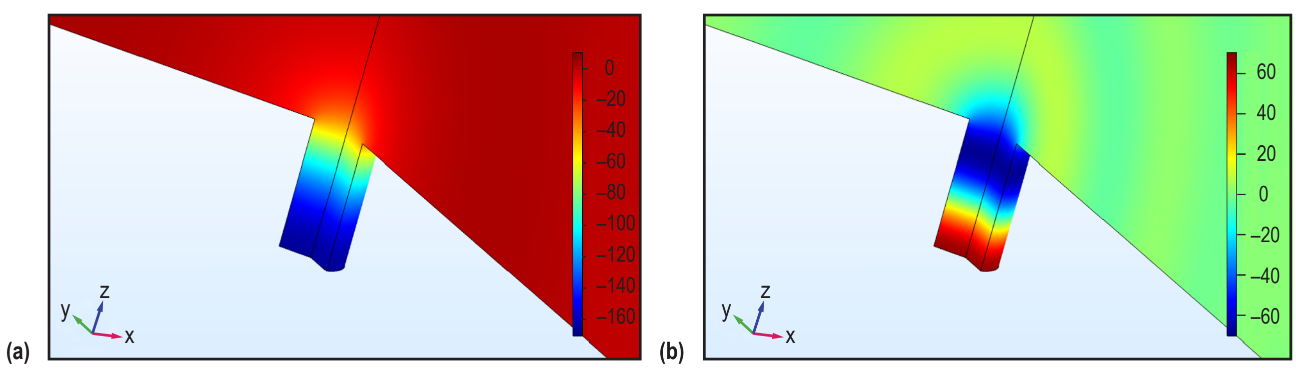

Figure 30. Total pressure contour plot: (a) Quarter-wave mode at 2,834 Hz and (b) three-quarter-wave mode at 8,799 Hz. Scales show units of Pa deviation from ambient.

As a note in using COMSOL, these calculations can be performed in the Results branch by defining a Join node within the Data Sets branch. The Parametric Sweep will produce independent Solution data sets and, in this example, the Join node can be used to combine the two Solution data sets. Conveniently, the back of the port in the baseline domain and the projection location where the port would be in the secondary domain use the same total acoustic pressure boundary probe. While the amplification factor can simply be created by using the Quotient combination method, the phase must use the General combination method. In the Join node, with the primary domain configuration set as Data 1 and the secondary domain configuration set as Data 2, the expression below can be used in COMSOL to compute the relative phase (in degrees). The Join node is a Data Set and can be recalled, for example, using a Global plot.

```
180/pi*atan2(imag(data1)*real(data2)-real(data1)*imag(data2),real(data1)*real(data2)+imag(data1)*imag(data2))
```

4. DATA ANALYSIS

4.1 Specialized Filter Design

A specialized filter is designed such that it can be applied to data and modify the data based on the sensor port transfer function. In most cases, a filter is used to pass certain frequencies and reject others, but, in general, a filter is a device that modifies certain frequencies relative to others.[24, p. 439] The transfer function shown in figure 27 can be modified and converted into a filter, and subsequently applied to the data. Example simulated data can be generated and the transfer function can be directly applied to the data to understand the effects of the port response. Alternatively, the inverse transfer function can be estimated and then applied to data to remove the sensor port effects. Note that the analytical sensor port response from figure 27 is used in this analysis, which has a peak resonance at 2,811 Hz and amplification factor of 18.1×.

The procedure to apply a filter based on the frequency response function is relatively straightforward. The software tool PC-SIGNAL[25] by AI Signal Research, Inc has the procedure entirely automated and is used to perform the analysis in this section. This software tool is a specialized dynamic signature analysis software package for rocket engine and rotating machinery health monitoring, fault detection, and diagnostics. It incorporates the conventional signal analysis capabilities as well as state-of-the-art signature analysis technologies that have been developed over years of research on dynamic data, particularly from the Space Shuttle main engine.

Conceptually, the procedure is very simple. The impulse response describing the transfer function must first be obtained. This is done by computing the inverse discrete Fourier transform of the transfer function. Then, by convolving the impulse response with the data signal, a modified time history is obtained. The convolution step allows the impulse response to be used effectively as a 'filter' where the filter characteristics are described by the features of the transfer function, i.e., the filter provides gain and phase characteristics as defined by the transfer function.

Verification can be performed that shows the specialized filter is free of signal artifacts associated with Gibbs phenomena by computing the frequency response function of the impulse response function while zero-padding. However, in general, the transfer function gain is relatively smooth compared to typical steep roll-off bandpass and band-stop filters. Typically, the concern occurs with wrapped phase angles where a sudden jump in phase occurs, yet, if necessary, the phase can be smoothed with minimal effect on the signal.

To correct data that are known to be contaminated by a sensor port response, the inverse transfer function has to be estimated. The inverse transfer function, equations (83) and (84), are analogous to the sensor port response given previously as equations (10) and (11):

$$\widehat{X}(f) = \left| \frac{\hat{p}_D}{\hat{p}_U} \right| \tag{83}$$

and

$$\widehat{\phi}(f) = \angle \left(\frac{\hat{p}_D}{\hat{p}_U} \right) . \tag{84}$$

For lack of nomenclature, the amplification factor and relative phase of the inverse transfer function will be referred to as the inverse sensor port response.

Using the example that produced figure 27 (the analytical model solution), the inverse sensor port response is shown in figure 31.

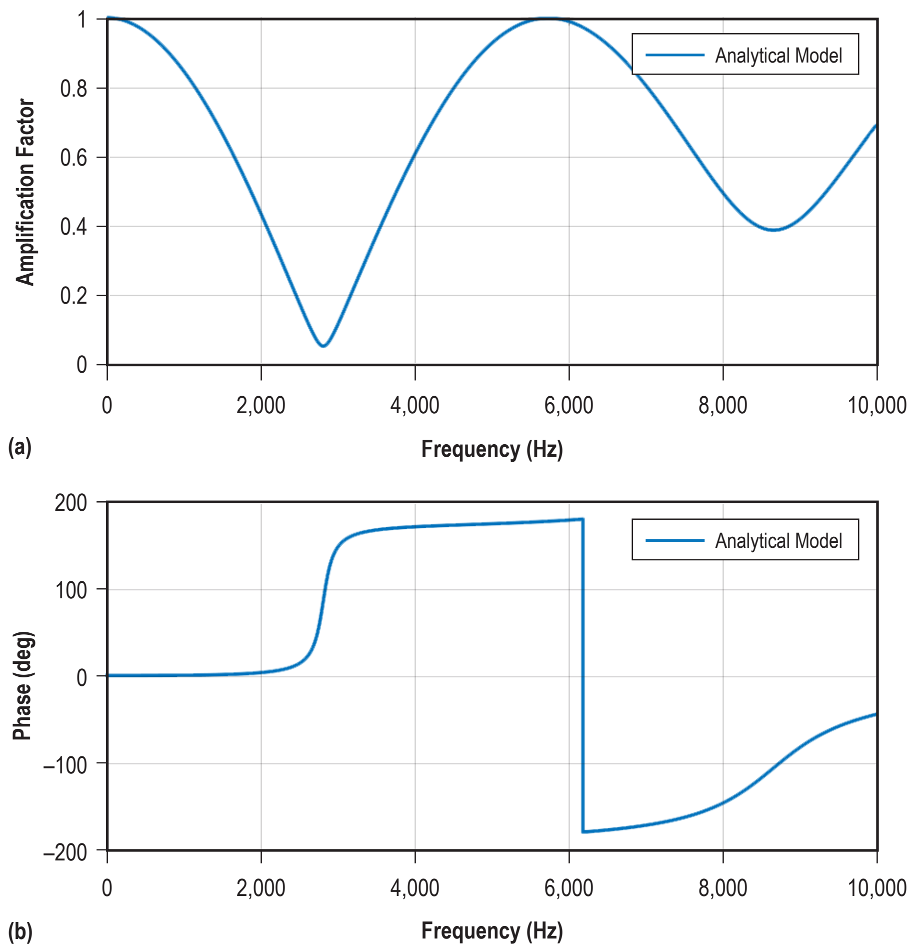

Figure 31. Inverse sensor port response: (a) Amplification factor and (b) relative phase.

The transfer function described in figure 31 is truncated at 10 kHz since this domain was determined to be the relevant data range for the example; however, an analytic model can be estimated over any frequency bandwidth. From 10 kHz to the Nyquist frequency of the simulated data (50 kHz), the amplification factor and phase are set at zero. In general, truncation in this fashion may not be an ideal approach in filter design as sudden changes can introduce Gibbs phenomena, and a smooth roll-off may be better suited; however, this was a simple modification and done for the example. To use the advantage of processes suited for power of 2, the number of points that make up the transfer function is set to 16,385 points which gives the transfer function a frequency resolution of 3.0518 Hz. The impulse response of the transfer function is obtained by estimating the inverse discrete Fourier transform and subsequently applying a half block time delay to the result using a circular shift. This introduces a known time delay that is later corrected, but most importantly, it centers the impulse response function to help minimize discontinuities. The filter order of the impulse response is 32,768 points; a zoomed-in section near the center is shown in figure 32. The impulse response function contains all the information necessary to describe the transfer function and can be used as a specialized filter.

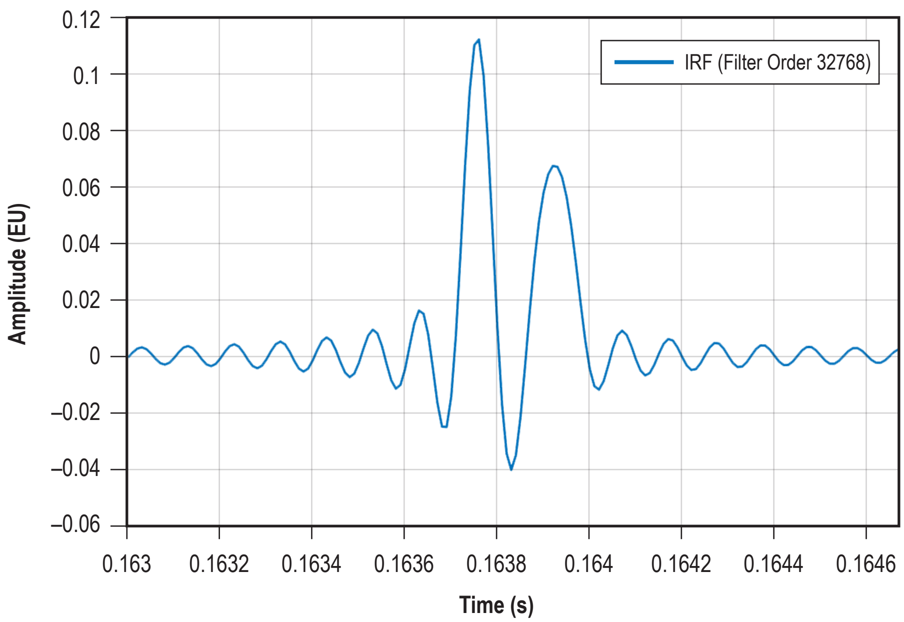

Figure 32. Impulse response function—zoomed.

To investigate the effect of the specialized filter on real data, two sets of simulated data are first generated at 100,000 sps shown in figure 33. A 10-s time series is generated that contains uniformly distributed random numbers in the open interval from –1 to 1. Another 10-s time series is generated that is simply a sinusoid at 2,811 Hz. This frequency occurs at the resonance of the sensor port response (the analytical model solution) or antiresonance of the inverse sensor report response shown in figure 31.

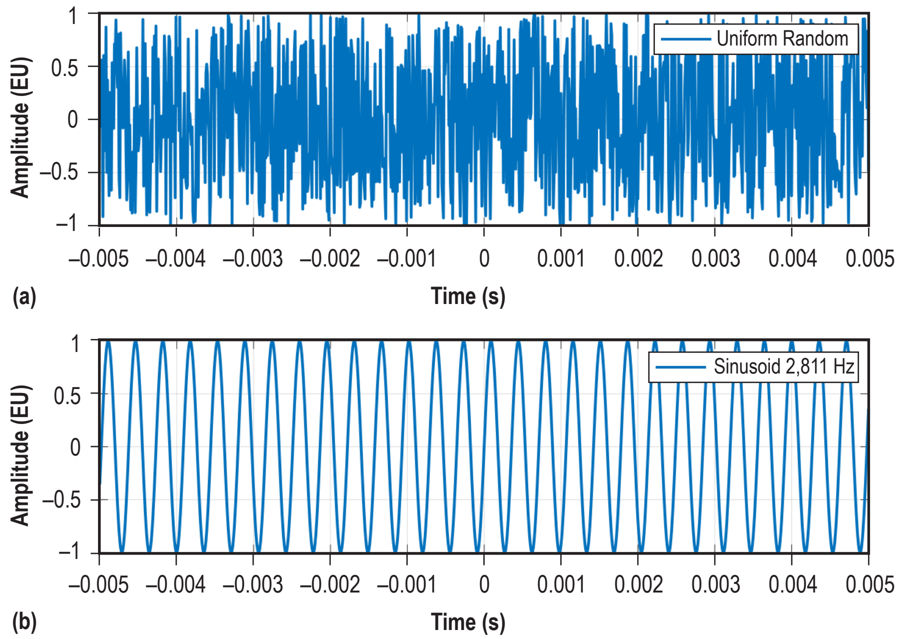

Figure 33. Simulated time series: (a) Uniform random and (b) 2,811 Hz sinusoid.

As noted earlier, the impulse response is subsequently convolved with the original simulated data to produce the filtered data time series. Figure 34 shows a power spectral density (PSD) overlay plot of the original uniform random data and the newly filtered data. The original uniform random data are constant over all frequencies for a PSD, which makes it a useful data set for examining filter effects.

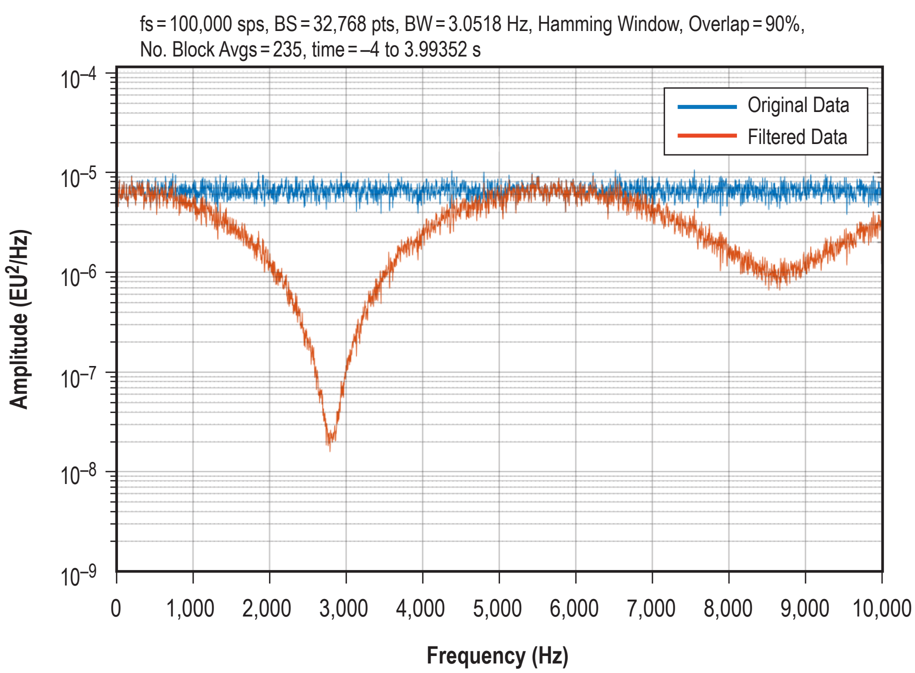

Figure 34. Power spectral density plot—original uniform random data and filtered data.

A transfer function estimate can be made by computing the ratio of the cross PSD and reference PSD.[26, pp. 78–81, 105] The two signals for the estimated transfer function are the original simulated uniform random data and the filtered uniform random data, i.e., filtered using the specialized filter. A data block size of 32,768 points is selected to process the transfer function since it will result in the same frequency resolution of 3.0518 Hz for the 100,000 sps data. This data block size is not necessary, but will produce a point-to-point comparison to the initial transfer function filter. A comparison of the initial transfer function filter to the estimated transfer function using the uniform random data is shown in figure 35. In fact, the comparison is so close that the frequency axis is shown through 11 kHz to emphasize the computed transfer function estimate actually uses the data. The transfer function estimate attempts to produce zero values for the amplitude at frequencies higher than 10 kHz to match the initial truncated transfer function specification. This results in an extremely small amplitude close to zero and a random phase.

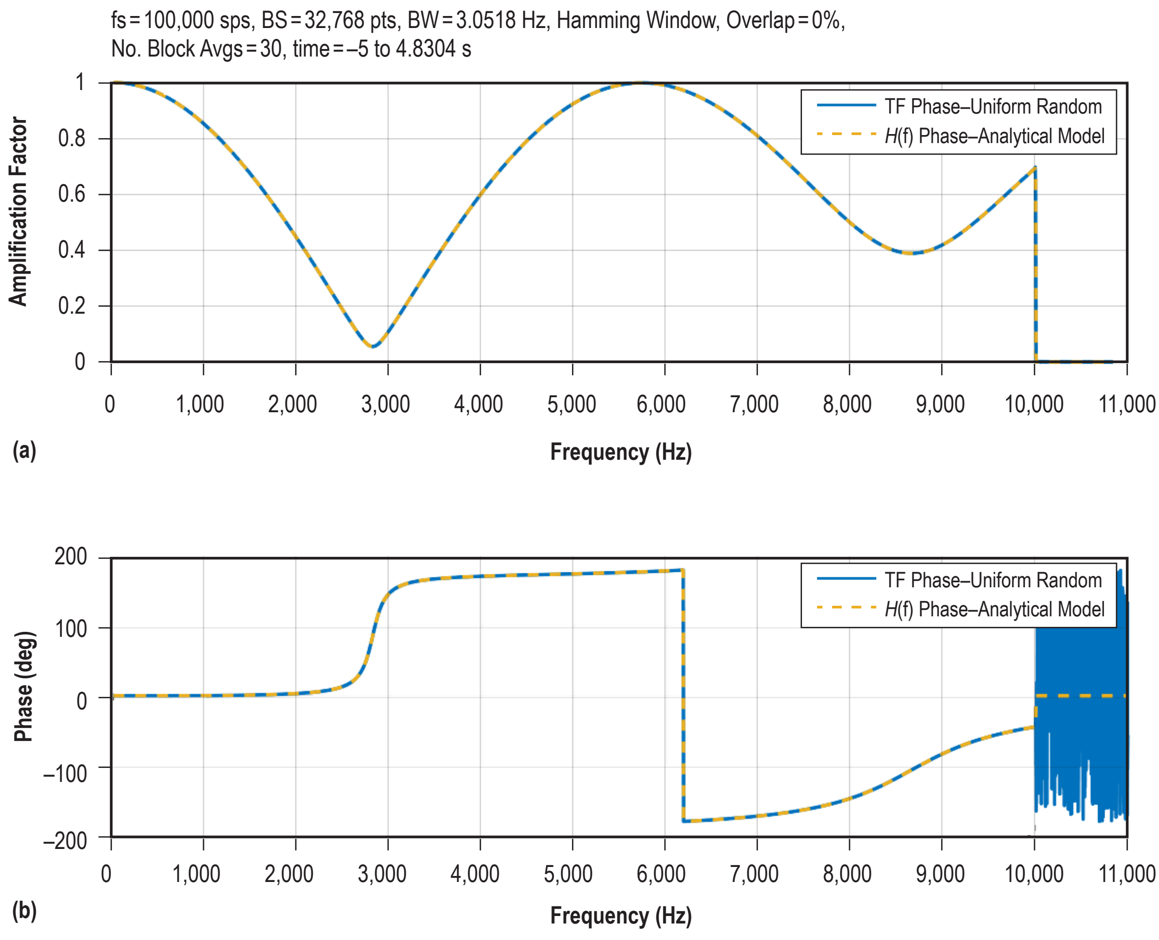

Figure 35. Inverse sensor port response—transfer function comparison using uniform random data: (a) Amplification factor and (b) relative phase.

Finally, the same filter is applied to the simulated sinusoidal data. The original data and the filtered data are overlaid and zoomed in figure 36 to show the amplitude reduction of 18.1× and the phase shift of 86°, recalling that a positive phase shift shifts a sinusoid in the negative direction. The amplification reduction and relative phase compares exactly to the values selected at the resonance frequency (2,811 Hz) directly from the inverse transfer function in figure 31. This indicates that the filtered data were appropriately represented based on the inverse transfer function.

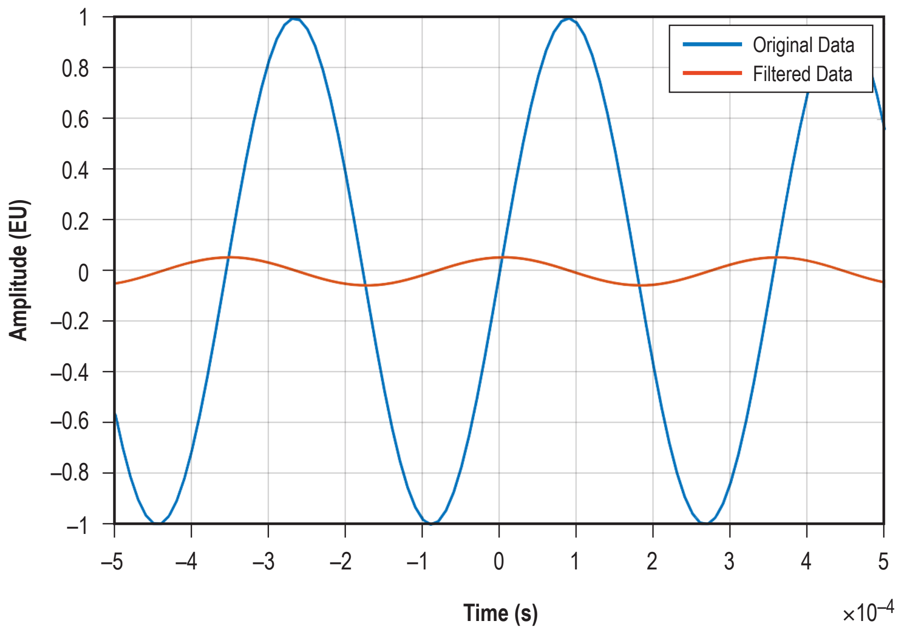

Figure 36. Sinusoidal comparison (2,811 Hz).

This filtering procedure is very powerful and can be used to predict the effect of a sensor port on data or to make corrections to data that are influenced by sensor ports.

5. SUMMARY

A sensor port is part of the system being measured, but it is not part of the system that is intended to be measured. Even a short sensor port may have an adverse contribution to collected data. Surprisingly, limited analysis has been described on the determination of the overall frequency response of a recessed acoustic cavity, where models in the literature using lumped acoustic elements fall short due to their extreme assumptions.[2, p. 283] The acoustic resonance within the sensor port produces a frequency-dependent amplification and phase deviation that directly affects the data collected.

Traditional design criteria for recess length are based on an undamped forced oscillator frequency response model. This model is improved in this TP to directly incorporate an end user's acceptable error. While this model provides a guide for a sensor port design, it does not produce a representative frequency response, and breaks down in many cases such as at frequencies closer to the resonance or in multiport designs. Estimates that are more accurate may even allow the recess to be lengthened, e.g., so a more accurate estimate may be desired. Additionally, an accurate estimate could be useful for correcting data.

As an advancement to the undamped SDOF model used classically for sensor port analysis, a theory is developed for obtaining the actual acoustic frequency response of a sensor port. Three critical advancements were necessary to extend the classic acoustic theory into a practical sensor port frequency response model. The application of a distributed acoustic model rather than the classic lumped acoustic elements was necessary to capture the higher frequency effects. The development of a practical form of the exact solution to the thermoviscous wave equation was necessary for use in the propagation constant model. The reformulation of acoustic radiation impedance as an acoustic propagation constant was also necessary for use in the propagation constant model. Two dissipation mechanisms are required for an accurate sensor port analysis, i.e., thermoviscous effects and radiation acoustics. The distributed acoustic model framework can incorporate these effects for a constant diameter sensor port by applying a two-line model. An analytic form is derived for the two-line model so that the response can be predicted quickly, easily, and accurately. Pseudocode is also presented for a multiline model so the frequency response of more complex sensor ports can be modeled.

A primary advantage of a computer simulation, or numerical modeling, is to tackle problems that are too complex for analytical solutions. A major advantage, aside from the ability to model sophisticated physical problems and a 3-D geometry, is that the models are deterministic. This is an advantage since a direct comparison can easily be made by numerically comparing the solutions of the exact configuration (with a sensor port) and the desired configuration (usually with no sensor port). Simulating the exact configuration and the desired configuration separately using all of the identical simulation conditions, e.g., same excitation source and same boundary conditions, allows pertinent quantities of interest between the two configurations to be obtained very precisely and compared. Using this procedure, an accurate transfer function can be obtained for any sensor port system. The theory for this comparative analysis is developed and described throughout. The innovative yet very basic procedure is remarkably powerful when combining solutions from deterministic numerical simulations.

As part of the verification procedure for the sensor port simulation, piston functions and thermoviscous responses are modeled separately. Comparing to known analytical results allows confidence in the sensor port domain and mesh design since the sensor port response encompasses the same dissipation processes. Piston functions, which are the basis for the radiation acoustics model, are simulated numerically and compared to analytic models with exact reproduction. The added length, or end correction of a port, is studied numerically as well, showing that there is a significant frequency dependence.

Thermoviscous effects are simulated and compared to analytic models, also with exact reproduction. Simulations using more sophisticated thermoviscous models are also performed, including applying the linearized Navier-Stokes or more advanced multiphysics simulations. These models are executed to help understand physics associated with deviations from the simpler models. An example multiphysics simulation is applied to a liquid and compared to the analytical model showing good comparison. The thermoviscous responses associated with nonlinear amplitudes are described showing a clear damping effect with increased oscillation amplitude, however, also producing secondary resonances.

A sensor port is modeled numerically and compared to the newly developed analytic theory. The results show a very good comparison and encompass the dissipation associated with both thermoviscous effects and radiation acoustics. The transfer function, equations (10) and (11); characteristic impedance, equation (22); transfer equation, equation (37); and propagation constants, equations (51) and (73), can be used to plot the analytical solution of a constant diameter sensor port response. The pseudocode described in the text can be used for more complex systems. A MATLAB® script is given in appendix P.

A specialized filter is designed such that it can be applied to data and modify the data based on the sensor port transfer function. The filter is applied to simulated data to show the influence on data. This filter procedure is very powerful and can be used to predict the effect of a sensor port on data or to make corrections to data that is influenced by sensor ports.

Corrections to the reference 27 summary have been made in this TP.

APPENDIX A—DEVELOPMENT OF TRANSFER EQUATIONS

The development of the spatial transfer equations begins by recognizing the time-harmonic solution form of the wave equation. The wave equation can be transformed simply by assuming a time-harmonic signal, resulting in the Helmholtz equation.[1, pp. 44–46] The solution to the wave equation can then be characterized as having separate spatial and temporal functions.[1, pp. 298–300; 7, p. 291]

To maintain consistency with the acoustical-electrical analogy, pressure and volume velocity are used in the formulation. By extending the time-harmonic solution, equation (12), for both an outgoing and incoming wave, the pressure solution can be represented as equation (85):

$$p' = \left(\bar{P}_+ e^{-\hat{\gamma}x} + \bar{P}_- e^{\hat{\gamma}x}\right) e^{i\omega t} \quad . \tag{85}$$

Similarly, the volume velocity, can be written in terms of particle velocity and represented as equation (86):

$$q' = Au' = \left(\bar{Q}_+ e^{-\hat{\gamma}x} + \bar{Q}_- e^{\hat{\gamma}x}\right) e^{i\omega t} \quad . \tag{86}$$

The first step in deriving useful transfer equations is to put the constants in equations (86) in terms of the constants in equation (85). This can be done by examining a relationship between pressure and velocity derived by combining the linearized form of the continuity equation and equation of state.[1, p. 38] Note that the constant of proportionality, g_c, a unit conversion factor used to convert mass to force, is not included in the equations. In many cases, density can be replaced as $\rho \rightarrow \rho / g_c$ when using English Engineering Units, however, unit checks are always prudent.

The values of $\bar{Q}$ in terms of $\bar{P}$ can then be obtained by substituting equations (85) and (86) into equation (87) which uses partial derivative notation:

$$p'_t + \bar{\rho}\bar{c}^2 u'_x = 0 \, . \tag{87}$$

It can also be obtained similarly by using the linearized momentum equation, not shown here.[1, p. 37] These relationships are shown as equations (88) and (89):

$$\bar{Q}_+ = \frac{Ai\omega}{\bar{\rho}\bar{c}^2\hat{\gamma}} \bar{P}_+ \tag{88}$$

and

$$\bar{Q}_- = \frac{Ai\omega}{\bar{\rho}\bar{c}^2\hat{\gamma}} \bar{P}_- \quad . \tag{89}$$

Using equations (88) and (89), equation (86) can be written as equation (90):

$$q' = -\frac{Ai\omega}{\bar{\rho}\bar{c}^2\hat{\gamma}}\left(\bar{P}_+ e^{-\hat{\gamma}x} - \bar{P}_- e^{\hat{\gamma}x}\right)e^{i\omega t} \quad . \tag{90}$$

A characteristic impedance can now be defined for an outgoing wave. This can be obtained by examination of the ratio of the first term in equation (85) and first term in equation (90). This definition is shown as equation (91):

$$Z_C \equiv \left(\frac{p'}{q'}\right)_+ = \frac{\bar{\rho}\bar{c}^2\hat{\gamma}}{Ai\omega} = -\frac{\bar{\rho}\bar{c}^2\hat{\gamma}}{A\omega}i \quad . \tag{91}$$

Note for the lossless wave equation, the propagation constant is given by $\hat{\gamma} = ik = i\omega / \bar{c}$ and the characteristic impedance simplifies to the well-known form for propagation through a pipe, $Z_C = \bar{\rho}\bar{c}/A$ (or in the form of specific acoustic impedance, $z_C = \bar{\rho}\bar{c}$).[2, p.126, 288] Also note that for an incoming wave, the characteristic impedance can be regarded as $-Z_C$. The volume velocity can be rewritten as equation (92):

$$q' = \frac{1}{Z_C}\left(\bar{P}_+ e^{-\hat{\gamma}x} - \bar{P}_- e^{\hat{\gamma}x}\right)e^{i\omega t} \quad . \tag{92}$$

Equations (85) and (92) can be written in terms of the spatial distribution and temporal distribution as equations (93) and (94), respectively:

$$p' = \tilde{p}(x)e^{i\omega t} \tag{93}$$

and

$$q' = \tilde{q}(x)e^{i\omega t} . \tag{94}$$

Transfer equations, $\tilde{p}(x)$ and $\tilde{q}(x)$, can be extracted by considering only the spatial component in a length of ‘pipe’.

The solution is time-independent and describes only the spatial distribution. However, by inspection of equations (85) and (92), the spatial distribution for pressure and volume velocity can be written as equations (95) and (96):

$$\tilde{p}(x) = \bar{P}_+ e^{-\hat{\gamma}x} + \bar{P}_- e^{\hat{\gamma}x} \tag{95}$$

and

$$\tilde{q}(x) = \frac{1}{Z_C}\left(\bar{P}_+ e^{-\hat{\gamma}x} - \bar{P}_- e^{\hat{\gamma}x}\right) . \tag{96}$$

By examining the pipe section shown in figure 3 and applying the boundary condition at the upstream location where $\tilde{p}(0) = p_U$ and $\tilde{q}(0) = q_U$, the constants $\bar{P}_+$ and $\bar{P}_-$ can be found. The solution as a function of axial position can then be found by substituting these into equations (95) and (96) and converting the exponentials to hyberbolic trigonometric functions. The final form is shown as equations (97) and (98):[7, pp. 289–293]

$$\tilde{p}(x) = p_U \cosh(\hat{\gamma}x) - Z_C q_U \sinh(\hat{\gamma}x) \tag{97}$$

and

$$\tilde{q}(x) = -\frac{p_U}{Z_C}\sinh(\hat{\gamma}x) + q_U \cosh(\hat{\gamma}x) \ . \tag{98}$$

Equations (97) and (98) are the solution to the Helmholtz equation or spatial solutions to the wave equation in terms of pressure and volume velocity, and referred to as transfer equations. They simply describe the spatial distribution within a pipe section. These equations provide a useful framework that is applicable, in general, to propagation through a dissipative fluid in pipe systems and waveguides.

APPENDIX B—ABSORPTION IN FLUIDS: ABSORPTION COEFFICIENT AND PHASE SPEED

There are several modes of acoustic absorption in fluids. Boundary layer absorption is the dominant mode for evaluation of a sensor port response. While the exact form for boundary layer absorption is recommended, equations (52) and (53), the other boundary layer absorption models are discussed in this section. Other modes of absorption include intrinsic absorption associated with propagation in an open fluid, and molecular relaxation where there is a relaxation time associated with molecular motion to reach thermodynamic equilibrium. Moreover, for reference, the classic intrinsic absorption model for propagation in an open fluid is also discussed. Molecular relaxation is discussed further in reference 1, p. 315–322, 513–518.

Specific formulations for α and β can be derived for a given physical process, by substituting equation (15) into its governing wave equation. At times in this section, complex wave number is used in the derivation rather than propagation constant for consistency with reference 1, pp. 324–325. Note also that various forms of the propagation constant are discussed in literature.[8]

B.1 Boundary Layer Absorption—Traditional Model

The traditional model for boundary layer absorption was discussed previously in section 2.4.1, and can be derived in multiple ways. One approach is to examine the impedance due to viscosity that is presented to the force of a propagating wave, and to examine the thermal diffusion process near the wall and associated energy loss.[2, pp. 230–234] The most direct approach is to begin with the boundary layer absorption wave equation, equation (43), which is developed using similar considerations, i.e., considering the drag force on a fluid and heat transfer from the wall.[1, pp. 519–525] As discussed in section 2.4, a propagation constant can be obtained from the wave equation and linearized to obtain the traditional model.[1, pp. 324–325]

As noted in section 2.3.1, the absorption coefficients and phase speed are obtained from the complex wave number or complex propagation constant. Substituting the solution form, equation (12), into the wave equation, equation (43), rewritten here as equation (99) using partial derivative notation, results in the exact form of the complex propagation constant for boundary layer absorption:

$$p_{xx} - \frac{1}{\bar{c}^2} p_{tt} = \frac{2}{R} \cdot \sqrt{\frac{\mu}{\bar{\rho}\pi}} \left(1 + \frac{\gamma - 1}{\sqrt{\mathrm{Pr}}}\right) \cdot \int_0^\infty \frac{p_{xx}(x, t-\tau)}{\sqrt{\tau}} d\tau \ . \tag{99}$$

This is written as the complex wave number in equation (44) and rewritten here as equation (100):

$$\hat{k}_{\mathrm{BL}} = \frac{\omega / \bar{c}}{\sqrt{1 - \frac{2}{R}\sqrt{\frac{\mu}{i\omega\bar{\rho}}}\left(1 + \frac{\gamma - 1}{\sqrt{\mathrm{Pr}}}\right)}} \ . \tag{100}$$

The traditional form of absorption coefficients and phase speed, though, can be obtained by first linearizing the exact complex wave number using a series expansion. For example, the series expansion in equation (101) to first order can be used to obtain equation (102) from equation (100):

$$\frac{1}{\sqrt{1-X}} = 1 + \frac{X}{2} + \frac{3}{8}X^2 + \cdots \tag{101}$$

and

$$\hat{k}_{\text{BL,series}} = \frac{\omega}{\bar{c}}\left(1 + \frac{1}{R}\sqrt{\frac{\mu}{i\omega\bar{\rho}}}\left(1 + \frac{\gamma-1}{\sqrt{\text{Pr}}}\right)\right) . \tag{102}$$

Using the relationship $\sqrt{2/i} = 1-i$, equation (102) can be expanded as equation (103):

$$\hat{k}_{\text{BL,series}} = \frac{\omega}{\bar{c}}\left(1 + (1-i)\frac{1}{R}\sqrt{\frac{\mu}{2\omega\bar{\rho}}}\left(1 + \frac{\gamma-1}{\sqrt{\text{Pr}}}\right)\right) . \tag{103}$$

The imaginary part of equation (103) is the traditional absorption coefficient and given as equation (104):

$$\alpha_{\mu\kappa} = \frac{1}{\bar{c}R} \cdot \sqrt{\frac{\mu\omega}{2\,\bar{\rho}}}\left(1 + \frac{\gamma-1}{\sqrt{\text{Pr}}}\right) . \tag{104}$$

This is the traditional form of the absorption coefficient and is a linearized form of the exact solution. It is written previously as equation (46).

The phase shift parameter can be approximated from the real part of equation (103) given as equation (105):

$$\beta_{\text{BL,series}} = \frac{\omega}{\bar{c}}\left(1 + \frac{1}{R}\sqrt{\frac{\mu}{2\omega\bar{\rho}}}\left(1 + \frac{\gamma-1}{\sqrt{\text{Pr}}}\right)\right) . \tag{105}$$

The phase speed can then be approximated using equation (16) and equation (105) and written as equation (106):

$$c_{p,\text{BL,series}} = \frac{\bar{c}}{1 + \frac{1}{R}\sqrt{\frac{\mu}{2\omega\bar{\rho}}}\left(1 + \frac{\gamma-1}{\sqrt{\text{Pr}}}\right)} . \tag{106}$$

Finally, to obtain the traditional form of phase speed, equation (106) is linearized. The series expansion in equation (107) to first order can be used to obtain equation (108):

$$\frac{1}{\sqrt{1+X}} = 1 - \frac{X}{2} + \frac{3}{8}X^2 - \cdots \tag{107}$$

and

$$c_{p,\mu\kappa} = \bar{c} - \frac{\bar{c}}{R}\sqrt{\frac{\mu}{2\omega\bar{\rho}}}\left(1 + \frac{\gamma-1}{\sqrt{\mathrm{Pr}}}\right) . \tag{108}$$

Equation (108) is the traditional form of the phase speed written previously as equation (48).

The traditional propagation is reconstructed as equation (49) and rewritten here as equation (109):

$$\hat{\gamma}_{\mu\kappa} = \frac{1}{\bar{c}R}\cdot\sqrt{\frac{\mu\omega}{2\bar{\rho}}}\left(1+\frac{\gamma-1}{\sqrt{\mathrm{Pr}}}\right) + i\cdot\frac{\omega}{\bar{c}}\cdot\left(1-\frac{1}{R}\sqrt{\frac{\mu}{2\omega\bar{\rho}}}\left(1+\frac{\gamma-1}{\sqrt{\mathrm{Pr}}}\right)\right)^{-1} . \tag{109}$$

B.2 Boundary Layer Absorption—Exact First-Order Model

In section 2.4.1, the traditional model for boundary layer absorption is discussed and in section 2.4.2, the exact model for boundary layer absorption is discussed. Here, a first-order series approximation to the exact form, different from the traditional model, is derived that is occasionally used in analyses. For conciseness, the exact complex wave number, equation (100), can be written in terms of the traditional boundary layer absorption coefficient, equation (104). This is written as equation (50) and rewritten here as equation (110):

$$\hat{k}_{\mathrm{BL}} = \frac{\omega / \bar{c}}{\sqrt{\left(1-\frac{2\bar{c}}{\omega}\alpha_{\mu\kappa}\right) + i\cdot\frac{2\bar{c}}{\omega}\alpha_{\mu\kappa}}} . \tag{110}$$

The derivation of the first-order model approximation is very similar to the approach used in appendix B.1 and described briefly here. Expanding equation (110) into a series and collecting first-order terms, as described in appendix B.1, gives the complex wave number shown as equation (111):

$$\hat{k}_{\mathrm{BL,series}} = \left(\frac{\omega}{\bar{c}} + \alpha_{\mu\kappa}\right) - i\cdot\alpha_{\mu\kappa} . \tag{111}$$

This is equivalent to equation (103), but written in terms of traditional absorption coefficient. By inspection and comparing equation (111) to equation (13), note that the absorption coefficient is equal to the traditional absorption coefficient described by equation (104). Using equations (13) and (16) to obtain phase speed from equation (111) gives the first-order series expansion solution as equation (112):

$$c_{p,\mathrm{BL,series}} = \bar{c}\left(1+\frac{\bar{c}}{\omega}\alpha_{\mu\kappa}\right)^{-1} \quad . \tag{112}$$

This is equivalent to equation (106). While another linearization step is taken in appendix B.1 to obtain the traditional form of the phase speed, this model does not take this additional step and uses equation (112) directly. The exact propagation constant to first order is reconstructed as equation (113) and expanded as equation (114):

$$\hat{\gamma}_{\mathrm{BL,series}} = \alpha_{\mu\kappa} + i\left(\frac{\omega}{\bar{c}}+\alpha_{\mu\kappa}\right) \tag{113}$$

and

$$\hat{\gamma}_{\mathrm{BL,series}} = \frac{1}{\bar{c}R}\cdot\sqrt{\frac{\mu\omega}{2\bar{\rho}}}\left(1+\frac{\gamma-1}{\sqrt{\mathrm{Pr}}}\right)+i\cdot\frac{\omega}{\bar{c}}\cdot\left(1+\frac{1}{R}\sqrt{\frac{\mu}{2\omega\bar{\rho}}}\left(1+\frac{\gamma-1}{\sqrt{\mathrm{Pr}}}\right)\right). \tag{114}$$

This form is occasionally used in analysis and is a slight improvement over the traditional form.

B.3 Boundary Layer Absorption—Heuristic Model

The heuristic model is based on linearizing a steady flow-based wall friction model and then applying it to thermoviscous boundary layer absorption. It uses steady flow-based wall friction at low frequency as a basis for losses.[7, pp. 289–293; 9, pp. 3–5; 10, pp. 13–17]

The lossy wave equation can be obtained from the linearized momentum equation written in a lossy form,[1, p. 37] equation (115), and the linearized continuity equation,[1, p. 38] equation (116), both using partial derivative notation:

$$p'_x + \bar{\rho}u'_t + \frac{R_{L,p/u}}{L}u' = 0 \tag{115}$$

and

$$p'_t + \bar{\rho}\bar{c}^2 u'_x = 0 \quad . \tag{116}$$

The lossy form contains a third term derived by considering steady flow-based wall friction.[7, pp. 20–23, 33, 289–290] This term contains the pressure-velocity form of linearized resistance, however, note that it is not a true acoustic resistance since it does not relate pressure to volume velocity. Equation (116) was given previously as equation (87).[1, pp. 27–39; 2, pp. 121–124] Note that these equations are similar to the acoustic form of the telegrapher's equations, which are used as the basis for lumped parameter models through piping systems. This is described in appendix O.

Another common form of linearized resistance is in a pressure-mass flow rate framework and the resistance relationship is simply given as equation (117), however, again note this is not a true acoustic resistance.

$$R_{L,\,p/u} = \bar{\rho} A \cdot R_{L,\,p/\dot{m}} \ . \tag{117}$$

The linearized resistance calculation for steady flow is described in references 7, p. 290; 9, p. 5; and 28, p. 135; however, the resistance is retained generically in the equations for use in approximating damping behavior for any model in a phenomenological fashion.[7, p. 290]

The wave equation can be written by appropriately combining equations (115) and (116):

$$p'_{xx} - \frac{R_{L,\,p/\dot{m}} A}{\bar{c}^2 L} p'_t - \frac{1}{\bar{c}^2} p'_{tt} = 0 \ . \tag{118}$$

The wave equation can also be written with a spatial absorption coefficient considering that the pressure drop per unit length is associated with thermoviscous effects:[9, pp. 3–5; 10, pp. 13–17]

$$p'_{xx} - \frac{2\alpha}{\bar{c}} p'_t - \frac{1}{\bar{c}^2} p'_{tt} = 0 \ . \tag{119}$$

The spatial absorption coefficient can then be related to the pressure-mass flow rate form of linearized resistance by comparing equation (118) and equation (119).[9, p. 6] The absorption coefficient here is known a priori and the traditional absorption coefficient can be substituted into equation (120):

$$R_{L,\,p/\dot{m}} = \frac{2L\bar{c}}{A} \alpha \ . \tag{120}$$

The propagation constant using this model is given as equation (121):[7, pp. 289–293; 10, p. 17]

$$\hat{\gamma}_{\text{heuristic}} = \sqrt{-\left(\frac{\omega}{\bar{c}}\right)^2 + \frac{2\alpha\omega}{\bar{c}} i} \ . \tag{121}$$

It is simplest to numerically compute the real and imaginary part of equation (121) to obtain the absorption coefficient and derive the phase speed; however, a similar approach, as discussed in appendix D, can be used to obtain the absorption parameters analytically.

This is not an exact model for boundary layer dissipation or based on the boundary layer physics, however, provides a reasonable estimate.

B.4 Intrinsic Absorption

Absorption due to intrinsic mechanisms are usually negligible for sensor port analysis; however, the intrinsic thermoviscous models may be needed in certain scenarios. These classical absorption models are important in an open fluid over long distances.

The wave equation describing intrinsic viscous effects is developed using the Navier-Stokes,[1, pp. 303–306; 2, pp. 211–213] and is given in terms of a relaxation time, $\tau = \left(4/3\mu + \mu_B\right)/\rho\bar{c}^2$ as equation (122), shown using partial derivative notation:[2, p. 212]

$$p'_{xx} + \tau p'_{xxt} = \frac{1}{\bar{c}^2} p'_{xxt} \quad . \tag{122}$$

The intrinsic viscous absorption coefficient, α_{v}, and phase speed, $c_{p,\mathrm{v}}$, are obtained from the propagation constant as described in reference 2, p. 212. By using the approximation that $\omega\tau \ll 1$, a series expansion of the functions $\alpha_{\mathrm{v}}(\omega\tau)$ and $c_{p,\mathrm{v}}(\omega\tau)$ can be used to obtain expanded forms of the absorption coefficient and phase speed, given as equations (123) and (124), respectively:

$$\alpha_{\mathrm{v}} = \frac{\omega^2 \mu}{2\rho\bar{c}^3}\left(\frac{4}{3} + \frac{\mu_B}{\mu}\right) \tag{123}$$

and

$$c_{p,\mathrm{v}} = \bar{c}\left(1 + \frac{3}{2}\left(\frac{\alpha_{\mathrm{v}}\bar{c}}{\omega}\right)^2\right) \quad . \tag{124}$$

Also with this assumption, the wave equation, while no longer exact, can be written in terms of the intrinsic viscous absorption coefficient:

$$p'_{xx} + \frac{2\alpha_{\mathrm{v}}\bar{c}}{\omega^2} p'_{xxt} = \frac{1}{\bar{c}^2} p'_{tt} \quad . \tag{125}$$

The wave equation for intrinsic thermal conduction is given by equation (126) by considering conservation of energy.[1, pp. 306–313] With some manipulation of the linearized continuity equation, linear momentum equation, and linearized conservation of energy equation, the acoustic density and particle velocity can be eliminated and the wave equation can be written in terms of acoustic pressure:

$$\frac{\mu}{\mathrm{Pr}}\left[p_{xx} - \frac{\gamma}{\bar{c}^2} p_{tt}\right]_{xx} - \left[p_{xx} - \frac{1}{\bar{c}^2} p_{tt}\right]_t = 0 \quad . \tag{126}$$

It is reduced by considering that the first bracketed term has a very small effect and a zero-order approximation can be applied in this term, $p_{xx} = p_{tt}/\bar{c}^2$.[1, p. 313] The resulting approximate equation is given as equation (127) and the intrinsic thermal absorption coefficient is given as equation (128):[1, p. 313]

$$p'_{xx} + \frac{2\alpha_{\text{th}}\bar{c}}{\omega^2} p'_{xxt} = \frac{1}{\bar{c}^2} p'_{tt} \tag{127}$$

and

$$\alpha_{\text{th}} = \frac{\omega^2 \mu}{2\rho\bar{c}^3}\left(\frac{\gamma-1}{\text{Pr}}\right) . \tag{128}$$

Note that the wave equation form is similar to that of equation (125).

Similar to the intrinsic viscous model, the intrinsic thermal phase speed is given by equation (129):

$$c_{p,\text{th}} = \bar{c}\left(1+\frac{3}{2}\left(\frac{\alpha_{\text{th}}\bar{c}}{\omega}\right)^2\right) . \tag{129}$$

Combining equations (123) and (128) gives the classical absorption coefficient:

$$\alpha_c = \frac{\omega^2 \mu}{2\rho\bar{c}^3}\left(\frac{4}{3}+\frac{\gamma-1}{\text{Pr}}\right) . \tag{130}$$

Combining equations (124) and (129) gives the combined phase speed as equation (131):

$$c_{p,c} = \bar{c}\left(2+\frac{3}{2}\left(\frac{\bar{c}}{\omega}\right)^2\left(\alpha_{\text{th}}^2+\alpha_{\text{v}}^2\right)\right) . \tag{131}$$

Additional details of this absorption mode is discussed in reference 1, pp. 303–315; 2, pp. 211–218.

APPENDIX C—GENERAL THERMOVISCOUS MODEL

The motion of a viscous compressible Newtonian fluid, including an energy equation, is governed by equations (132) through (137) shown using vector notation.[11, p. 500] The dependent variables are pressure, p, velocity, u, temperature, T, and density, ρ. Equations (132) through equations (134) are the continuity equation, momentum equation (Navier-Stokes equation), and energy equation, respectively:

$$\frac{D\rho}{Dt} + \rho(\nabla \cdot \vec{u}) = 0\,, \tag{132}$$

$$\rho \frac{D\vec{u}}{Dt} = (\nabla \cdot \boldsymbol{\sigma}) + \vec{F}\,, \tag{133}$$

and

$$\rho C_p \frac{DT}{Dt} - \alpha_p T \frac{Dp}{Dt} = -\nabla \cdot \vec{q} + \phi + Q\,. \tag{134}$$

Equations (135) through (137) are constitutive equations that define the total stress tensor through the Stokes expression, $\boldsymbol{\sigma}$, the Fourier heat conduction law (with heat flux, q), and an equation of state, respectively:

$$\boldsymbol{\sigma} = -p\mathbf{I} + \mu\left(\nabla\vec{u} + \left(\nabla\vec{u}\right)^T\right) - \left(\frac{2}{3}\mu - \mu_B\right)(\nabla \cdot \vec{u})\mathbf{I}\,, \tag{135}$$

$$\vec{q} = -k\nabla T\,, \tag{136}$$

and

$$\rho = \rho(p,T)\,. \tag{137}$$

The properties of the fluid include the dynamic viscosity, μ, thermal conductivity, k, bulk viscosity, μ_B, specific heat at constant pressure, C_p, and isobaric coefficient of volumetric thermal expansion, α_p. The coefficient of volumetric thermal expansion is given as equation (138):[11, p. 501]

$$\alpha_p = -\frac{1}{\rho}\left.\frac{d\rho}{dT}\right|_p\,. \tag{138}$$

Equation (134) is a form of the energy equation and discussed further in appendix K.[19, pp. 333–338] Also, to keep the momentum equation, equation (135), concise for numerical analysis and separate from the constitutive equation, the viscous stress tensor is expanded and includes matrix notation. The viscous dissipation function, ϕ, a volume force, F, or a heat source, Q, are not considered for thermoviscous problems but included in the equation set for completeness.

APPENDIX D—REAL AND IMAGINARY PARTS OF EXACT PROPAGATION CONSTANT

Equation (50) gives the exact wave number for the boundary layer and is rewritten here as equation (139):

$$\hat{k}_{\text{BL}} = \frac{\omega / \overline{c}}{\sqrt{\left(1 - \frac{2\overline{c}}{\omega}\alpha_{\mu\kappa}\right) + i \cdot \frac{2\overline{c}}{\omega}\alpha_{\mu\kappa}}} \; . \tag{139}$$

An analytic expression for the propagation constant can be obtained in an exact manner by first splitting the complex wave number, equation (139), into the real and imaginary part. The complication arises because of the difficulty in obtaining the real and imaginary part of a square root term. This can be addressed by recognizing that the principal square root is defined as equation (140):

$$\sqrt{z} = e^{1/2\,\ln(z)} = e^{1/2\,\ln(|z|) + i\,1/2\,\arg(z)} \; . \tag{140}$$

The real and imaginary parts of the square root function in the denominator of equation (139) can be found by first applying and simplifying equation (140) as equations (141) and (142), respectively:

$$\Re\left(\sqrt{z}\right) = \sqrt{|z|}\cos\left(\frac{\arg(z)}{2}\right) \tag{141}$$

and

$$\Im\left(\sqrt{z}\right) = \sqrt{|z|}\sin\left(\frac{\arg(z)}{2}\right) \; . \tag{142}$$

After defining z as the radicand in the denominator of equation (139), and also by replacing the argument function with the two-argument arctangent function, the real and imaginary parts can then be written as equations (143) and (144):

$$R_{\text{den}} = \Re\left(\sqrt{z}\right) = \sqrt[4]{\left(\left(1 - \frac{2\overline{c}}{\omega}\alpha_{\mu\kappa}\right)^2 + \left(\frac{2\overline{c}}{\omega}\alpha_{\mu\kappa}\right)^2\right)} \cdot \cos\left(\frac{1}{2}\tan 2^{-1}\left(\frac{2\overline{c}}{\omega}\alpha_{\mu\kappa},\, 1 - \frac{2\overline{c}}{\omega}\alpha_{\mu\kappa}\right)\right) \tag{143}$$

and

$$I_{\text{den}} = \Im\left(\sqrt{z}\right) = \sqrt[4]{\left(\left(1 - \frac{2\overline{c}}{\omega}\alpha_{\mu\kappa}\right)^2 + \left(\frac{2\overline{c}}{\omega}\alpha_{\mu\kappa}\right)^2\right)} \cdot \sin\left(\frac{1}{2}\tan 2^{-1}\left(\frac{2\overline{c}}{\omega}\alpha_{\mu\kappa},\, 1 - \frac{2\overline{c}}{\omega}\alpha_{\mu\kappa}\right)\right) \; . \tag{144}$$

Note that the radical represents the fourth root of its radicand.

Now that the real and imaginary part of the denominator are found, equation (139) can be written concisely as equation (145):

$$\hat{k}_{\mathrm{BL}} = \frac{\omega / \bar{c}}{R_{\mathrm{den}} + i \cdot I_{\mathrm{den}}} \ . \tag{145}$$

The real and imaginary part of equation (145) can now be split easily and the complex wave number can simply be written as equation (146):

$$\hat{k}_{\mathrm{BL}} = \left(\frac{\omega}{\bar{c}} \cdot \frac{R_{\mathrm{den}}}{\left(R_{\mathrm{den}}\right)^2 + \left(I_{\mathrm{den}}\right)^2} \right) - i \cdot \left(\frac{\omega}{\bar{c}} \cdot \frac{I_{\mathrm{den}}}{\left(R_{\mathrm{den}}\right)^2 + \left(I_{\mathrm{den}}\right)^2} \right). \tag{146}$$

Using equations (13) and (14), the complex propagation constant is given by equation (147) where the real and imaginary parts can be described using equations (143) and (144):

$$\hat{\gamma}_{\mathrm{BL}} = \left(\frac{\omega}{\bar{c}} \cdot \frac{I_{\mathrm{den}}}{\left(R_{\mathrm{den}}\right)^2 + \left(I_{\mathrm{den}}\right)^2} \right) + i \cdot \left(\frac{\omega}{\bar{c}} \cdot \frac{R_{\mathrm{den}}}{\left(R_{\mathrm{den}}\right)^2 + \left(I_{\mathrm{den}}\right)^2} \right). \tag{147}$$

APPENDIX E—OVERALL EFFECTIVE PARAMETERS

An effective absorption coefficient that describes the system absorption can be developed. Since the domains of the thermoviscous physics and the radiation acoustics are separate, the absorption coefficients cannot simply be added as described in equation (45). The procedure in developing an effective absorption coefficient is shown here for the two-lined model, so that both thermoviscous and radiation effects can be effectively combined. The total geometric length, L_T, is the most obvious characteristic length that would be used to define an effective parameter. Equation (29) can be used to represent the effective parameters as it considers a single overall length. For the two-line model, equation (29) can be equated to equation (37):

$$\operatorname{sech}\left(\hat{\gamma}_{\text{eff}} L_T\right) = \left(\cosh\left(\hat{\gamma}_{\text{A}} L_{\text{A}}\right)\cosh\left(\hat{\gamma}_{\text{B}} L_{\text{B}}\right) + \frac{Z_{C,\text{A}}}{Z_{C,\text{B}}}\sinh\left(\hat{\gamma}_{\text{A}} L_{\text{A}}\right)\sinh\left(\hat{\gamma}_{\text{B}} L_{\text{B}}\right)\right)^{-1} . \tag{148}$$

From equations (14) and (16), an effective sound speed and effective absorption coefficient can be obtained first by solving for the effective propagation constant, $\hat{\gamma}_{\text{eff}}$. Solving equation (148) first for the effective propagation constant gives equation (149):

$$\hat{\gamma}_{\text{eff}} = \frac{1}{L_T} \cdot \cosh^{-1}\left(\cosh\left(\hat{\gamma}_{\text{A}} L_{\text{A}}\right)\cosh\left(\hat{\gamma}_{\text{B}} L_{\text{B}}\right) + \frac{Z_{C,\text{A}}}{Z_{C,\text{B}}}\sinh\left(\hat{\gamma}_{\text{A}} L_{\text{A}}\right)\sinh\left(\hat{\gamma}_{\text{B}} L_{\text{B}}\right)\right) . \tag{149}$$

An effective phase speed, can be written as equation (150) using equation (14) and equation (16).

$$c_{\text{eff}} = \frac{\omega}{\Im\left(\hat{\gamma}_{\text{eff}}\right)} . \tag{150}$$

An effective spatial absorption coefficient can be written as equation (151) using equation (14).

$$\alpha_{\text{eff}} = \Re\left(\hat{\gamma}_{\text{eff}}\right) . \tag{151}$$

The procedure can be extended to multiline models for more complex geometries.

APPENDIX F—ANALYTICAL EXPRESSION FOR A TERMINATION IMPEDANCE IN A SENSOR PORT CONFIGURATION

Section 2.5 discusses the radiation impedance based on a piston model. However, instead of estimating radiation impedance in this manner, it can be estimated by considering a general termination impedance and an expression that describes planar wave propagation through a port. The diagram in figure 37 shows a port of length, L. It is driven at one end by a source and there is a general termination impedance, Z_R, at the other end. The general termination impedance can be regarded as the radiation impedance.The input impedance (driving-point impedance), Z_{in}, is obtained at the location of the input source. The propagation constant, or complex wave number, is for the port domain. A coordinate transformation shown in the figure is made for simplification where $d = L - x$.[1, pp. 130–134; 2, pp. 272–273]

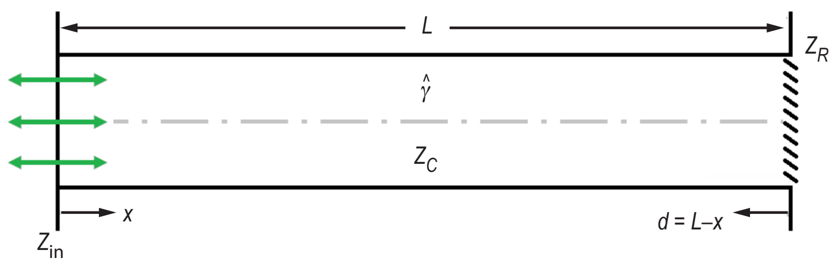

Figure 37. Port with a driver and general termination impedance.

In this scenario, the pressure amplitude solution to the Helmholtz equation can be written as equation (152) and the velocity amplitude can be written as equation (153):

$$\tilde{p}(d) = \bar{P}_{L+} e^{i\hat{k}d} + \bar{P}_{L-} e^{-i\hat{k}d} \tag{152}$$

and

$$\tilde{q}(d) = \frac{1}{Z_C}\left(\bar{P}_{L+} e^{i\hat{k}d} - \bar{P}_{L-} e^{-i\hat{k}d}\right) . \tag{153}$$

Using the complex wave number, these are equivalent to equation (95), and equation (96) in this different frame of reference, $d = L - x$, where the incident and reflected wave amplitudes can be represented as $\bar{P}_{L+} = \bar{P}_{+} e^{-i\hat{k}L}$ and $\bar{P}_{L-} = \bar{P}_{-} e^{i\hat{k}L}$. Note that now the incident wave phasor is associated with the positive exponent and the reflected wave phasor is associated with the negative exponent.

The impedance along the port can be written directly from equations (152) and (153):[2, pp. 272–273]

$$Z(d) = Z_C \frac{\bar{P}_{L+} e^{i\hat{k}d} + \bar{P}_{L-} e^{-i\hat{k}d}}{\bar{P}_{L+} e^{i\hat{k}d} - \bar{P}_{L-} e^{-i\hat{k}d}} \ . \tag{154}$$

The boundary condition for $d=0$ is $Z(0)=Z_R$ and for $d=L$ is $Z(L)=Z_{\mathrm{in}}$. Substituting these conditions into equation (154) gives equations (155) and (156), respectively:

$$Z_R = Z_C \frac{\bar{P}_{L+} + \bar{P}_{L-}}{\bar{P}_{L+} - \bar{P}_{L-}} \tag{155}$$

and

$$Z_{\mathrm{in}} = Z_C \frac{\bar{P}_{L+} e^{i\hat{k}L} + \bar{P}_{L-} e^{-i\hat{k}L}}{\bar{P}_{L+} e^{i\hat{k}L} - \bar{P}_{L-} e^{-i\hat{k}L}} \ . \tag{156}$$

Equations (155) and (156) can be combined to eliminate $\bar{P}_{L+}$ and $\bar{P}_{L-}$ to give equation (157).[2, pp. 51, 272–273] One algebraic approach is as follows: (1) solve for $\bar{P}_{L+}$ in equation (155), (2) substitute it into equation (156), and then solve the new formula for $\bar{P}_{L-}$, (3) eliminate $\bar{P}_{L+}$ and $\bar{P}_{L-}$ by substituting the newly found formulas into equation (156) and then solve for Z_R, (4) collect exponential terms with like coefficients in the numerator and separately in the denominator, (5) multiply the numerator by $1\Big/\left(Z_C \cdot \left(e^{i\hat{k}L} + e^{-i\hat{k}L}\right)\right)$ and convert exponential functions to the tangent function, and then multiply the denominator by $1\Big/\left(Z_C \cdot \left(e^{i\hat{k}L} + e^{-i\hat{k}L}\right)\right)$ and convert exponential functions to the tangent function:

$$Z_R = \frac{Z_{\mathrm{in}} - i \cdot Z_C \tan\left(\hat{k}L\right)}{1 - i \cdot \dfrac{Z_{\mathrm{in}}}{Z_C} \tan\left(\hat{k}L\right)} \ . \tag{157}$$

Using the relationship $\hat{k} = -i\hat{\gamma}$, equation (157) can be rewritten in terms of hyperbolic tangent and propagation constant as equation (158):

$$Z_R = \frac{Z_{\mathrm{in}} - Z_C \tanh\left(\hat{\gamma}L\right)}{1 - \dfrac{Z_{\mathrm{in}}}{Z_C} \tanh\left(\hat{\gamma}L\right)} \ . \tag{158}$$

This form is commonly used in distributed element models where the dimensions of the system are not small compared to the wavelength.[2, pp. 287–288] This particular transfer equation is often convenient since it relates the impedance at the downstream end in terms of the upstream end. A form of equation (158) is previously given as equation (26) where the impedance at the upstream end is in terms of the downstream end. Modeling distributed elements is often referred to as transmission line analysis since the analogy is to modeling high-frequency current along a transmission line. Transmission line analysis is used commonly in flow-acoustic modeling such as for combustion stability,[5, pp. 242, 273] pogo,[29, app. D, p. 13] and hydraulics.[7, p. 294]

An alternate form of equation (158) that is useful in analysis can also be expressed.[1, pp. 140–141; 30]

This form used in literature is given as equation (159):[30]

$$Z_{\text{in}} = i \cdot Z_C \tan\left(\hat{k}L + \tan^{-1}\left(\frac{Z_R}{i \cdot Z_C} \right) \right) . \tag{159}$$

Equation (160) is the alternate form of equation (158) and results after substituting $\hat{\gamma} = i\hat{k}$ into equation (159) and solving for the general termination impedance. This can be regarded as the radiation impedance in terms of the input impedance:

$$Z_R = i \cdot Z_C \tan\left(i\hat{\gamma}L + \tan^{-1}\left(\frac{Z_{\text{in}}}{i \cdot Z_C} \right) \right) . \tag{160}$$

While the form of equations (158) and (160) appear to be significantly different, they are in fact identical. This can be verified by applying the identity shown in equation (161) to equation (160), which can then be simplified to reproduce equation (158):

$$\tan(a+b) = \frac{\tan(a) + \tan(b)}{1 - \tan(a)\tan(b)} . \tag{161}$$

Given the input impedance, which can be obtained from a numeric simulation, either equation (158) or equation (160) can be used to remove the contribution of the port. This results in the radiation impedance for a port configuration. An example is described in appendix G.

APPENDIX G—RADIATION IMPEDANCE COMPARISON OF A FLANGED PISTON TO A FLANGED SENSOR PORT

A comparison of the normalized radiation impedance for a 0.5-in- (0.0127-m-) diameter piston in an infinite baffle and an analogous port configuration is shown in figure 38. The port has a 0.5 in (0.0127 m) diameter and is 1 in (0.0254 m) long. The radiation impedance for the piston in an infinite baffle is simply the driving point impedance of that system. The piston radiation impedance curves are computed using equations (74) and (75) and are identical to those shown in figure 11. However, to obtain the radiation impedance for a port configuration, the effect of the line has to be removed. This can be accomplished by examining the input impedance of a sensor port configuration with a general termination impedance at the opposite end, i.e., applying the distributed element representation given by equation (158). Appendix F provides the derivation of the radiation impedance for a port in the presence of a source at one end. Given the input impedance at the back end of the port from a COMSOL simulation, the real and imaginary parts of the equation (158) analytical solution can be used to plot the termination impedance (radiation impedance), which effectively removes the port contribution.

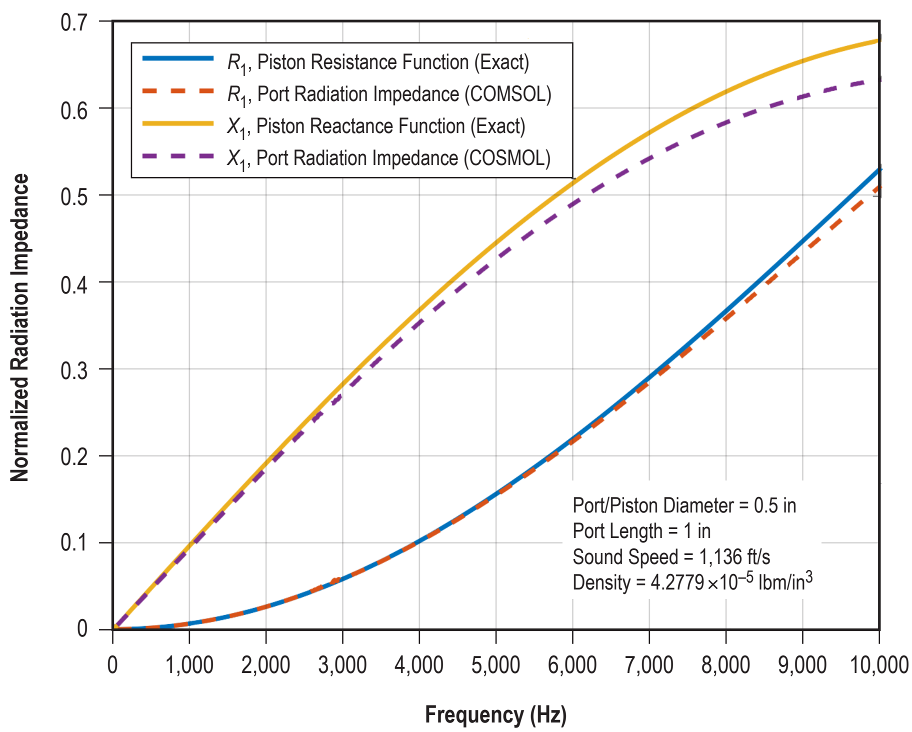

Figure 38. Radiation impedance for piston and a port.

Interestingly, the solution produces slightly different radiation impedance curves.[31] The propagating planar wave through the port affects the radiation impedance slightly differently than from an oscillatory piston located at the port exit location. An incident wave at an opening is affected by the dynamic state of the resonator and not simply enforced as in the piston model.[14, p. 332]

APPENDIX H—END CORRECTION FOR A SENSOR PORT

Two different approaches can be used to deduce the end correction of a sensor port. The first approach is to obtain the port radiation impedance from the system input impedance as described in appendix G. The radiation reactance contribution (imaginary part) can be used to estimate the end correction. The second approach compares the input impedance of a port that has a pressure release boundary to the input impedance of a port that has a termination impedance (app. F). An end correction can be derived from this comparison. Figure 37 in appendix F can be used for reference.

In the first approach, the input impedance can first be estimated simply by using a COMSOL simulation, i.e., by applying a frequency-dependent source at the back end of the port and obtaining the impedance at the source application location. From this input impedance, the radiation impedance can be determined using equation (160). Noting that equation (160) is acoustic impedance (described by eq. (17)), equation (57) can be used to obtain an effective mass and end correction from the radiation reactance, similar to the approach used in the piston model. The end correction using this approach is given as equation (162) where the input impedance of the system can be obtained from a numerical simulation.

$$\Delta L = \frac{A}{\bar{\rho}\omega} \cdot \Im\left[i \cdot Z_C \tan\left(i\hat{\gamma}L + \tan^{-1}\left(\frac{Z_{\mathrm{in}}}{i \cdot Z_C} \right) \right) \right] . \tag{162}$$

The second approach examines the input impedance of a pressure release system. The input impedance of a port with a pressure release at one end is given as equation (163):[1, p. 136]

$$Z_{\mathrm{in}} = i \cdot Z_C \tan\left(\hat{k}L \right) . \tag{163}$$

Since the input impedance with termination impedance, equation (159), and input impedance with pressure release condition, equation (163), are similar in form, an end correction can be deduced by comparison. The length in the pressure release model, equation (163), can be regarded as an effective length, $L' = L + \Delta L$, as used in the equation (3) model. After replacing the length by the effective length, a direct comparison can be made to deduce the end correction written as equation (164):

$$\Delta L = \frac{i}{\hat{\gamma}} \tan^{-1}\left(\frac{Z_R}{i \cdot Z_C} \right) . \tag{164}$$

The radiation impedance is computed using equation (160) where a COMSOL simulation is used to estimate input impedance.

This end correction can be used with simple hand calculations as it produces resonant conditions consistent with the effective length modification described in equation (3). However, the end correction here is a complex valued expression because it inherently includes both radiation resistance and reactance constituents. As $\hat{k}$ and ΔL are complex, it is described by reference 30 that the analogy holds only when the imaginary parts are small. Equation (164) can be written in terms of the input impedance as equation (165), after substituting equation (160) and taking the real part:

$$\Delta L = -\Im\left[\frac{1}{\hat{\gamma}}\tan^{-1}\left(\tan\left(i\hat{\gamma}L + \tan^{-1}\left(\frac{Z_{\text{in}}}{i \cdot Z_C}\right)\right)\right)\right] . \tag{165}$$

Note that $\tan^{-1}(\tan(x)) \neq x$ for all x, and cannot be further simplified. Also note that $\Re(i \cdot \hat{x}) = -\Im(\hat{x})$.

The first method, equation (162), and the second method, equation (165), appear to have a similar form, but are not the same. A plot of the two methods is shown in figure 39 along with effective height estimates for a piston. For the effective height estimates, equation (62) is used for the exact solution, equation (76) is used for the COMSOL solution, and equation (2) is used for the approximate solution. A true port end correction is also extracted from a COMSOL sensor port frequency response.

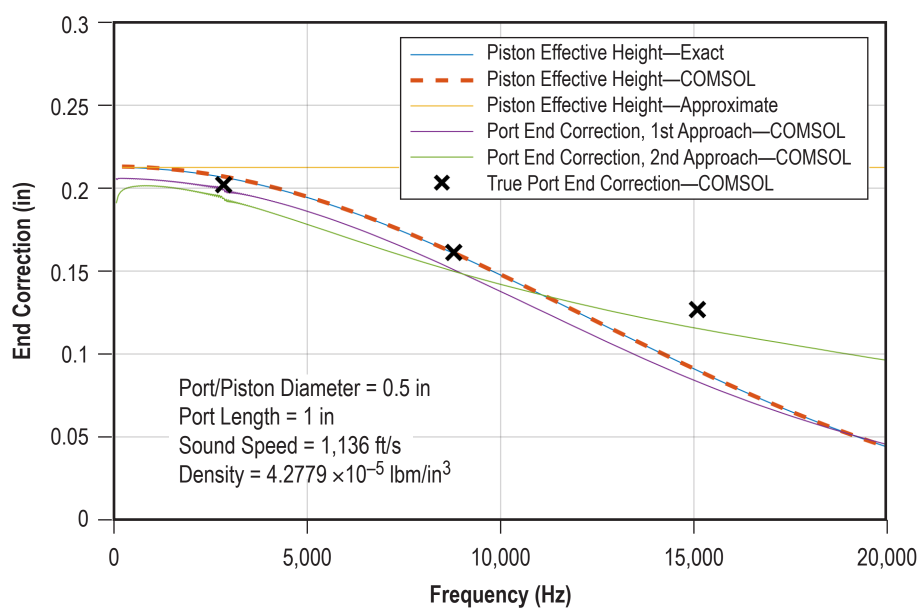

Figure 39. Piston effective height or port end correction (figure uses EE units).

The COMSOL sensor port response simulation is used to obtain the true port end correction.The frequencies where the amplification factor has maxima are selected e.g., maxima shown in figure 27. The frequencies 2,834 Hz, 8,801 Hz, and 15,117 Hz are used in equation (3) or the appropriate integer harmonic form to obtain the true end correction. The same COMSOL model is used to extract input impedance as is used to obtain amplification factor, except that the input impedance model requires the driver at the sensor port back. The error in the end correction models is therefore associated with the best possible representation associated with the equation (3) model analogy. The best model appears to be equation (165); however, all the representations of the end correction only approximate the frequency of the true resonance using the simple form of equation (3).

APPENDIX I—POWER SERIES EXPANSIONS FOR PISTON FUNCTIONS

There are several ways to describe the power series given in equations (59) and (60). Examples are given in terms of the gamma function, factorial, and double factorial (not a repeated factorial). Note that either the gamma function, fractional factorials, product notation, or double factorials must be used for evaluation. The alternate forms were provided in an effort to aid in different methods of computation, as large values of m become exceedingly difficult to compute because of limitations of most computer processors:

$$R_1(x) = 1 - \frac{2J_1(x)}{x} = \sum_{m=0}^{\infty} \frac{(-1)^m}{\Gamma(m+2)\Gamma(m+3)} \left(\frac{x}{2}\right)^{2m+2} = \sum_{m=0}^{\infty} \frac{(-1)^m}{(m+1)!(m+2)!} \left(\frac{x}{2}\right)^{2m+2}$$

$$= \frac{1}{2} \sum_{m=0}^{\infty} \frac{(-1)^m}{\prod_{k=0}^{m}(k+1) \prod_{k=0}^{m}(k+2)} \left(\frac{x}{2}\right)^{2m+1} = 2 \sum_{m=0}^{\infty} \frac{(-1)^m \cdot (2m+4)}{((2m+4)!!)^2} x^{2m+2} \qquad (166)$$

and

$$X_1(x) = \frac{2H_1(x)}{x} = \sum_{m=0}^{\infty} \frac{(-1)^m}{\Gamma\left(m+\frac{3}{2}\right)\Gamma\left(m+\frac{5}{2}\right)} \left(\frac{x}{2}\right)^{2m+1} = \sum_{m=0}^{\infty} \frac{(-1)^m}{\left(m+\frac{1}{2}\right)!\left(m+\frac{3}{2}\right)!} \left(\frac{x}{2}\right)^{2m+1}$$

$$= \frac{2}{\pi} \sum_{m=0}^{\infty} \frac{(-1)^m}{\prod_{k=0}^{m}\left(k+\frac{1}{2}\right) \prod_{k=0}^{m}\left(k+\frac{3}{2}\right)} \left(\frac{x}{2}\right)^{2m+1} = \frac{4}{\pi} \sum_{m=0}^{\infty} \frac{(-1)^m (2m+3)}{((2m+3)!!)^2} x^{2m+1} \quad . \qquad (167)$$

APPENDIX J—PSEUDOCODE FOR CALCULATION OF THE STRUVE FUNCTION

The formal series expansion of the first-order Struve function is given as equation (168):

$$H_1(x) = \sum_{m=0}^{\infty} \frac{(-1)^m}{\Gamma\left(m+\frac{3}{2}\right)\Gamma\left(m+\frac{5}{2}\right)}\left(\frac{x}{2}\right)^{2m+2} = \sum_{m=0}^{\infty} \frac{(-1)^m}{\left(m+\frac{1}{2}\right)!\left(m+\frac{3}{2}\right)!}\left(\frac{x}{2}\right)^{2m+2}$$

$$= \frac{2}{\pi}\sum_{m=0}^{\infty} \frac{(-1)^m}{\prod_{k=0}^{m}\left(k+\frac{1}{2}\right)\prod_{k=0}^{m}\left(k+\frac{3}{2}\right)}\left(\frac{x}{2}\right)^{2m+2} = \frac{2}{\pi}\sum_{m=0}^{\infty} \frac{(-1)^m(2m+3)}{((2m+3)!!)^2}x^{2m+2} \ . \quad (168)$$

This is slightly different from equation (167), which has an additional factor.

This series can be used to approximate the exact first-order Struve function. References 15 and 16 also discuss efficient approximations for the Struve function, which may be necessary to achieve a small relative error. The following pseudocode provides an algorithm to calculate this function. One section of code provides exception handling for the algorithm. The exception handling helps ensure the approximation is not used outside of its bounds. For example, the power series expansion of equation (168) through $m = 100$ terms gives the relative error to within 1×10^{-7}% at $x = 10$, 4×10^{-6}% at $x = 20$, 0.04% at $x = 30$, and drops to 1% at $x = 33$. In this example, for higher frequencies, an improved estimate of the first-order Struve function using additional terms should be used. Note that numerically calculating the first-order Struve function using the series expansion becomes difficult with many terms. The series expansion term number is in both a power and factorial calculation and may quickly reach the computing size limit.

Pseudocode to obtain Struve function

```
Input: fmax // maximum frequency expected for analysis
Input: xmax // maximum wave number for a given relative error (obtain by comparing to exact
solution)
Input: D // line segment diameter
Input: c // line segment sound speed
Input: k_n // wave number for each frequency

// Define nondimensional variable used in 1st order Struve function
x_n = D × k_n

// Exception handling ensures the maximum frequency does not exceed a known relative error.
if fmax > c × xmax / (2 × pi ×D)) then
       fmax = floor(c × xmax / (2 × pi × D)));
       disp 'fmax reduced to ', fmax, ' Hz - to preserve Struve function accuracy'
end if
```

```
// 1st Order Struve Function
HNew = 0
for m = 0 to 100 by +1 do
       HOld_m = (-1)^m / gamma(m + 1.5) × gamma(m + 2.5)) × (x_n / 2)^(2 × m + 2)
       HNew_m = HOld_m + HNew_m
end for

// display 1st Order Struve function
disp HNew_m

end
```

APPENDIX K—ENERGY CHANGE EQUATION FOR A FLUID AND PRESSURE WORK CONTRIBUTION IN THERMOVISCOUS ACOUSTIC MULTIPHYSICS MODEL

The most useful form of energy equation for thermoviscous problems is one in the form of temperature. The objective of this section is to derive and understand the components of equation (134), the temperature formulation of the First Law of Thermodynamics, but also to recognize the contributions that are very important for thermoviscous problems. To obtain an energy framework with a temperature variable, the total energy equation must first be manipulated such that it describes the internal energy, and subsequently reformulated in terms of enthalpy. From equilibrium thermodynamics, the enthalpy equation can be simplified in a form with a temperature variable. This procedure is discussed further in references 19, pp. 333–338; 32, pp. 106–112; and 33, pp. 9–14. Note that reference 19 does not use the typical sign convention for the viscous work term and viscous stresses. Vector notation is used in this section.

The total energy equation is written as equation (169), i.e., the combination of the absolute thermodynamic internal energy and the kinetic energy:

$$\frac{\partial}{\partial t}\left[\rho\left(\frac{u_m^2}{2}+U\right)\right]+\nabla\cdot\left[\rho\vec{u}\left(\frac{u_m^2}{2}+U\right)\right]=-\nabla\cdot\vec{q}-\nabla\cdot p\vec{u}+\nabla\cdot\left(\vec{\vec{\tau}}\cdot\vec{u}\right)+\rho\vec{u}\cdot\vec{F}\ . \tag{169}$$

This is the First Law of Thermodynamics in differential form.[34, p.108] The terms are the following: rate of increase of energy (per unit volume), rate of energy addition by convective transport (per unit volume), rate of energy addition by conduction heat transfer (per unit volume), rate of work done on the fluid by pressure forces (per unit volume), rate of work done on the fluid by viscous forces (per unit volume), and rate of work done on the fluid by external forces (per unit volume). The variables are: density, ρ; velocity magnitude, u_m; velocity vector, $\vec{u}$; specific internal energy, U; conductive heat flux vector, $\vec{q}$; pressure, p; viscous stress tensor, $\vec{\vec{\tau}}$; and body force per unit mass (volume force), $\vec{F}$.

Recalling for future simplification, the pressure work term and viscous work terms can be split using the chain rule as equations (170) and (171), respectively:

$$\nabla\cdot p\vec{u}=p\nabla\cdot\vec{u}+\vec{u}\cdot\nabla p \tag{170}$$

and

$$\nabla\cdot\left(\vec{\vec{\tau}}\cdot\vec{u}\right)=\vec{\vec{\tau}}:\nabla\vec{u}+\vec{u}\cdot\left(\nabla\cdot\vec{\vec{\tau}}\right)\ . \tag{171}$$

The pressure work term represents the reversible work and the viscous work term represents the irreversible work. The colon operator is the double dot product.

The total energy equation is manipulated by subtracting the kinetic energy equation giving what is referred to as the thermal energy equation. The kinetic energy equation can first be obtained by taking the dot product of the velocity vector, $\vec{u}$, with the momentum equation, and is written as equation (172):

$$\frac{\partial}{\partial t}\left(\rho\frac{u_m^2}{2}\right)+\nabla\cdot\left(\rho\vec{u}\frac{u_m^2}{2}\right)=-\vec{u}\cdot\nabla p+\vec{u}\cdot\left(\nabla\cdot\vec{\vec{\tau}}\right)+\rho\vec{u}\cdot\vec{F} \quad . \tag{172}$$

Equation (173) shows the substitution of equation (171) into equation (172) and subtraction of the result from equation (169):

$$\frac{\partial}{\partial t}(\rho U)+\nabla\cdot(\rho\vec{u}U)=\left(-\nabla\cdot\vec{q}-\nabla\cdot p\vec{u}+\left[\vec{\vec{\tau}}:\nabla\vec{u}+\cancel{\vec{u}\cdot\left(\nabla\cdot\vec{\vec{\tau}}\right)}\right]+\cancel{\rho\vec{u}\cdot\vec{F}}\right)$$

$$-\left(-\vec{u}\cdot\nabla p+\cancel{\vec{u}\cdot\left(\nabla\cdot\vec{\vec{\tau}}\right)}+\cancel{\rho\vec{u}\cdot\vec{F}}\right) \quad . \tag{173}$$

Substituting equation (170) simplifies equation (173) to equation (174):

$$\frac{\partial}{\partial t}\left(\rho U\right)+\nabla\cdot\left(\rho\vec{u}\,U\right)=-\nabla\cdot\vec{q}-p\nabla\cdot\vec{u}+\vec{\vec{\tau}}:\nabla\vec{u} \quad . \tag{174}$$

Equation (174) is the thermal energy equation, also referred to as the heat equation. The equation denotes that internal energy increases because of convergence of heat, volume compression, and heating due to viscous dissipation.[34, p.108]

In general, there can be internal heat generation, Q, due to other modes of energy transfer and this contribution is included in equation (175):

$$\frac{\partial}{\partial t}\left(\rho U\right)+\nabla\cdot\left(\rho\vec{u}\,U\right)=-\nabla\cdot\vec{q}-p\nabla\cdot\vec{u}+\vec{\vec{\tau}}:\nabla\vec{u}+Q \quad . \tag{175}$$

In order to represent the thermal energy equation in terms of specific enthalpy, the thermodynamic definition, $U = H - p/\rho$, is used in equation (175) giving equation (176):

$$\frac{\partial}{\partial t}\left(\rho H\right)+\nabla\cdot\left(\rho\vec{u}H\right)=\frac{\partial p}{\partial t}+\nabla\cdot\left(p\vec{u}\right)-\nabla\cdot\vec{q}-p\nabla\cdot\vec{u}+\vec{\vec{\tau}}:\nabla\vec{u}+Q \quad . \tag{176}$$

Substituting equation (170) into equation (176) gives a simplified conservative form of the enthalpy equation, equation (177):

$$\frac{\partial}{\partial t}(\rho H)+\nabla\cdot(\rho\vec{u}H)=\frac{\partial p}{\partial t}+\vec{u}\cdot\nabla p-\nabla\cdot\vec{q}+\vec{\vec{\tau}}:\nabla\vec{u}+Q \ . \tag{177}$$

Using the chain rule, the left-hand side of equation (177) can be expanded into nonconservative form as equation (178):

$$\frac{\partial}{\partial t}(\rho H)+\nabla\cdot(\rho\vec{u}H)=\rho\frac{\partial H}{\partial t}+H\frac{\partial \rho}{\partial t}+\rho\vec{u}\cdot\nabla H+H\nabla\cdot(\rho\vec{u}) \ . \tag{178}$$

Equation (178) can be simplified to equation (179) using the continuity equation:

$$\frac{\partial}{\partial t}(\rho H)+\nabla\cdot(\rho\vec{u}H)=H\left(\cancel{\frac{\partial \rho}{\partial t}+\nabla\cdot\rho\vec{u}}\right)+\rho\left(\frac{\partial H}{\partial t}+\vec{u}\cdot\nabla H\right) \ . \tag{179}$$

Substituting equation (179) back into the left-hand side of equation (177) gives equation (180):

$$\rho\left(\frac{\partial H}{\partial t}+\vec{u}\cdot\nabla H\right)=\frac{\partial p}{\partial t}+\vec{u}\cdot\nabla p-\nabla\cdot\vec{q}+\vec{\vec{\tau}}:\nabla\vec{u}+Q \ . \tag{180}$$

The nonconservative form of the enthalpy equation can be written as equation (181) by substituting the material derivative:

$$\rho\frac{DH}{Dt}-\frac{Dp}{Dt}=-\nabla\cdot\vec{q}+\vec{\vec{\tau}}:\nabla\vec{u}+Q \ . \tag{181}$$

A thermodynamic relation can be used to express the energy equation in terms of temperature. An enthalpy, temperature, pressure relationship is given by equation (182) with specific volume, v:[33, p. 13; 35, pp. 188–193]

$$dH=C_p\,dT+\left(v-T\left.\frac{\partial v}{\partial T}\right|_p\right)dp \ . \tag{182}$$

The first term on the left-hand side of equation (181) can be simplified using the thermodynamic relationship given in equation (182), resulting in equation (183):

$$\rho\frac{DH}{Dt}=\rho C_p\frac{DT}{Dt}+\rho\left(\frac{1}{\rho}-T\left.\frac{\partial}{\partial t}\left(\frac{1}{\rho}\right)\right|_p\right)\frac{Dp}{Dt} \ . \tag{183}$$

This can be simplified to equation (184):

$$\rho \frac{DH}{Dt} = \rho C_p \frac{DT}{Dt} + \left(1 + \frac{T}{\rho} \frac{\partial \rho}{\partial T}\bigg|_p \right) \frac{Dp}{Dt} \ . \tag{184}$$

The coefficient of thermal expansion is given as equation (185) and can be substituted into equation (184), resulting in equation (186):

$$\alpha_p = -\frac{1}{\rho} \frac{\partial \rho}{\partial T}\bigg|_p \tag{185}$$

and

$$\rho \frac{DH}{Dt} = \rho C_p \frac{DT}{Dt} + \frac{Dp}{Dt} - \alpha_p T \frac{Dp}{Dt} \ . \tag{186}$$

The expansion of the first term on the left-hand side of equation (181), given as equation (186), can be substituted back into equation (181), resulting in equation (187):

$$\rho C_p \frac{DT}{Dt} - \alpha_p T \frac{Dp}{Dt} = -\nabla \cdot \vec{q} + \vec{\vec{\tau}} : \nabla \vec{u} + Q \ . \tag{187}$$

Equation (187) is the temperature formulation of the thermal energy equation given previously as equation (134). The total enthalpy equation used in many finite volume method solvers is prone to numerical oscillations that reduce numerical accuracy. The finite element method allows for the solution of the temperature equation and still conserves total energy, which is a much more robust and accurate approach.

In COMSOL, the second term on the left-hand side of equation (187) is referred to as the pressure work term and defined as equation (188):

$$Q_p \equiv \alpha_p T \frac{Dp}{Dt} \ . \tag{188}$$

This contribution, often neglected in traditional analyses, is very important for thermoviscous problems. The term represents the work done by pressure changes and can be described as having a thermal compressibility influence.

APPENDIX L—INSTANTANEOUS FREQUENCY TRACKING

An instantaneous frequency (IF) tracking method was used to obtain a signal amplitude from the COMSOL time domain simulations. The amplitude of the frequency of interest can therefore be plotted versus time and stationarity can be assured before the amplitude is selected. One powerful approach used to estimate instantaneous amplitude is based on the Hilbert transform. This approach is a frequency modulation demodulator and applies a synchronous receiver algorithm.[36; 37 p. 442]

The software tool PC-Signal®[25] by AI Signal Research, Inc has the instantaneous tracking procedure entirely automated and is used to perform the analysis in this TP. This software tool is a specialized dynamic signature analysis software package for rocket engine and rotating machinery health monitoring, fault detection, and diagnostics. It incorporates the conventional signal analysis capabilities as well as state-of-the-art signature analysis technologies that have been developed over years of research on dynamic data, particularly from the Space Shuttle main engine.

A narrow band random process can be modeled as a sinusoid with varying amplitude and phase and represented by equation (189):

$$x(t) = A(t) \cdot \cos\left(2\pi f_c t + \phi(t)\right) \ . \tag{189}$$

A complex demodulation of $x(t)$ is performed to estimate $A(t)$ and $\phi(t)$, which are the instantaneous amplitude and instantaneous phase, respectively. The instantaneous frequency is related to the time derivative of instantaneous phase. This time domain complex demodulation approach in estimating the Hilbert transform eliminates numerical artifacts associated with a direct approach, i.e., estimating Hilbert transform using fast Fourier transform (FFT) and inverse FFT. In the complex demodulation approach, phase shifting is applied to the signal by multiplying the signal separately by a sine and cosine signal at the frequency of interest. This effectively results in centering the bandwidth of interest on the zero frequency (and 2× the center frequency). Since all the required information is centered on the zero frequency, a low-pass filter is applied to the demodulated signal. This time domain technique does not rely on FFT blocks that often produce discontinuities between FFT blocks.

An alternate IF tracking method does use the frequency domain, but applies multiple hamming window applications so that the window is narrowed to within a small time resolution in the center of the block. An appropriate overlap associated with the multiple window application is used to ensure the data are fully captured. The chirp z-transform is used for efficiency as it is applied over a very small-frequency range of interest, but its algorithm also improves frequency resolution significantly. An integration in the frequency domain is performed to estimate amplitude, where the integration window changes for each instantaneous frequency. This method is not used here, but is a good alternative.

APPENDIX M—BOUNDARY LAYER MESH ELEMENTS FOR SMOOTH TRANSITION

Equation (77) is rewritten here as equation (190) where the parameters are the total length of the boundary layer mesh, L_{BL}; the thickness of the first layer element, h; the layer stretching factor, S, and the number of layer elements, n:

$$L_{\mathrm{BL}} = h\frac{S^n - 1}{S - 1} \ . \tag{190}$$

A relationship between parameters at the lower fundamental frequency and the highest harmonic frequency of interest can be obtained by first comparing equation (190) using lower frequency parameters and higher frequency parameters:

$$\frac{L_{h,\mathrm{BL}}}{L_{l,\mathrm{BL}}} = h_h \frac{S_h^{n_h} - 1}{S_h - 1} \bigg/ h_l \frac{S_l^{n_l} - 1}{S_l - 1} \ . \tag{191}$$

The stretching factor is maintained between the higher and lower frequency, $S_h = S_l = S$, and the overall mesh length is retained, $L_{h,\mathrm{BL}} / L_{l,\mathrm{BL}} = 1$. Also, to ensure the physical characteristics are accurately computed, the thickness of the first layer element is selected based on a percentage of the boundary layer thickness. The first layer element is therefore proportional to the boundary layer thickness, $h \sim \delta$. A relationship between parameters at the lower fundamental frequency and the highest harmonic frequency of interest can be obtained by first comparing either equation (39) or equation (40), which gives $h_h / h_l = \delta_h / \delta_l = \sqrt{f_l / f_h}$. With these simplifications, equation (191) becomes equation (192):

$$1 = \sqrt{\frac{f_l}{f_h}} \frac{S^{n_h} - 1}{S - 1} \bigg/ \frac{S^{n_l} - 1}{S - 1} \ . \tag{192}$$

Solving equation (192) for the number of elements needed for the higher frequency, followed by some simplification including the use of the ceiling function to ensure an integer number of layers, gives equation (193):

$$n_h = \left\lceil \ln\left(\frac{f_h}{f_l} \cdot \left(\left(S^{n_l} - 1 \right) + \sqrt{\frac{f_l}{f_h}} \right)^2 \right) \bigg/ \ln\left(S^2 \right) \right\rceil \ . \tag{193}$$

This relationship gives the number of element layers needed to obtain at least the same boundary layer length as the fundamental frequency, but when using the smaller initial layer thickness (for the highest harmonic frequency of interest). It considers that the stretching factor is maintained for a smooth transition over the range of frequencies.

APPENDIX N—ANGLE BETWEEN TWO COMPLEX NUMBERS

The angle between a vector, $\vec{z} = x + yi$, and the positive x-axis is given as the argument of the vector as described generally in equation (194) where, by convention, the argument is within the range $-\pi < \theta \le \pi$:[38, p. A-33]

$$\theta = \arg(\vec{z}) = \tan2^{-1}(y,x) \quad . \tag{194}$$

The angle between two vectors, $\vec{z}_1 = x_1 + y_1 i$ and $\vec{z}_2 = x_2 + y_2 i$, each with angles ϕ_1 and ϕ_2, respectively, is found from equation (195):

$$\phi = \phi_2 - \phi_1 \quad . \tag{195}$$

This can be written also as equation (196):

$$\tan(\phi) = \tan(\phi_2 - \phi_1) \quad . \tag{196}$$

The tangent angle difference identity is described as equation (197) and can be applied to equation (196):

$$\tan(\phi_2 - \phi_1) = \frac{\tan(\phi_2) - \tan(\phi_1)}{1 + \tan(\phi_1)\tan(\phi_2)} \quad . \tag{197}$$

Applying equation (197) to equation (196), and then substituting the two-argument arctangent function from equation (194) into equation (197) for each angle gives equaton (198):

$$\tan(\phi) = \frac{\tan\left(\tan2^{-1}(y_2,x_2)\right) - \tan\left(\tan2^{-1}(y_1,x_1)\right)}{1 + \tan\left(\tan2^{-1}(y_1,x_1)\right)\tan\left(\tan2^{-1}(y_2,x_2)\right)} \quad . \tag{198}$$

This can be simplified for all x and y using the following relationship in equation (199):

$$\tan\left(\tan2^{-1}(y,x)\right) = \frac{y}{x} \quad . \tag{199}$$

After simplification, equation (198) can be written as equation (200):

$$\tan(\phi) = \frac{\frac{y_2}{x_2} - \frac{y_1}{x_1}}{1 + \frac{y_1}{x_1}\frac{y_2}{x_2}} = \frac{x_1 y_2 - y_1 x_2}{x_1 x_2 + y_1 y_2} \ . \tag{200}$$

The two-argument arctangent function can then be used to find the angle in the range $-\pi < \theta \le \pi$ as equation (201):

$$\phi = \tan2^{-1}\left(x_1 y_2 - y_1 x_2,\ x_1 x_2 + y_1 y_2\right) \ . \tag{201}$$

This can be generalized to more than two dimensions and written in vector notation as equation (202):

$$\phi = \tan2^{-1}\left(\left|\vec{z}_1 \times \vec{z}_2\right|,\ \vec{z}_1 \cdot \vec{z}_2\right) \ . \tag{202}$$

APPENDIX O—LUMPED PARAMETER MODELS

The equations of motion for fluid transients can be written using the momentum and continuity equations, equations (115) and (116), and rearranged and rewritten in pressure-volume velocity form using partial derivative notation, where l is used for length to distinguish from inertance, L:

$$-p'_x = \frac{\bar{\rho}}{A} q'_t + \frac{R_{L,p/q}}{l} q' \tag{203}$$

and

$$-q'_x = \frac{A}{\bar{\rho} \cdot \bar{c}^2} p'_t \ . \tag{204}$$

Equations (203) and (204) are the acoustic form of the telegrapher's equations. To place these in a typical lumped parameter form, the definition of a derivative described in reference 1, pp. 18–22, and a discretization convention, one of which is described in figure 40, are needed. Using pressure and volume velocity, figure 40 also demonstrates that an acoustic system can be modeled as an analogous electrical circuit, where R' is resistance per unit length, L' is inertance per unit length, and C' is compliance per unit length. A string of incremental series resistances and inertances, with shunt compliances, can be used to model the acoustic system.

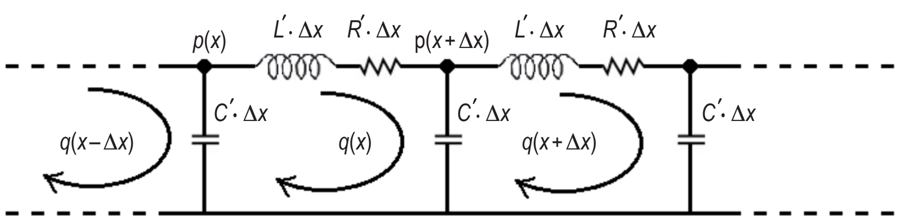

Figure 40. Acoustic transmission line—pressure and volume velocity.

A discretized form of equations (203) and (204) can be written using the discretization convention from figure 40 and lumped element length, Δx. These are given as equations (205) and (206):[1, pp. 18–22; 39, pp. 20–21]

$$p'(x) - p'(x+\Delta x) = \frac{\bar{\rho} \cdot \Delta x}{A} q'_t(x) + \frac{R_{L,p/q}}{l} \cdot \Delta x \cdot q'(x) \tag{205}$$

and

$$q'(x) - q'(x + \Delta x) = \frac{A \Delta x}{\bar{\rho}\,\bar{c}^2}\, p_t'(x + \Delta x) \ . \tag{206}$$

Various numerical schemes and grid conventions can be used to solve a lumped parameter system. Because the system is analogous to an electrical circuit, the coefficients are often written as an RLC circuit where the line parameters are given in equations (207)–(209), where the line parameters are resistance, R, inertance, L, and compliance, C:

$$R = R' \cdot \Delta x = \frac{R_{L,p/q}}{l} \cdot \Delta x \ , \tag{207}$$

$$L = L' \cdot \Delta x = \frac{\bar{\rho} \cdot \Delta x}{A} \ , \tag{208}$$

and

$$C = C' \cdot \Delta x = \frac{A \cdot \Delta x}{\bar{\rho}\,\bar{c}^2} \ . \tag{209}$$

While the inertance and compliance are obtained from the geometry and properties of the fluid, linearized resistance can be obtained by linearizing flow relationships described by pressure and volume velocity.

Additional information on the acoustical-electrical analogy, acoustic elements, and state space lumped parameter modeling can be found in reference 40.

APPENDIX P—MATLAB® SCRIPT: SENSOR PORT RESPONSE MODEL

```
%% Sensor Port Response Model
% This script predicts the sensor port frequency response in the form of an
% amplification factor and relative phase.
%
% Matt Casiano
% NASA Marshall Space Flight Center
% Fluid Dynamics
%
% Notes:
% The prediction gives the response at the back of a sensor port relative
% to the response at the wall of a configuration with no sensor port.  The
% acoustic resonance within a sensor port produces a frequency-dependent
% amplification and phase deviation that directly affects data collected.
%
% The model framework uses transfer equations to model the acoustics, and
% incorporates propagation constants for thermoviscous acoustics and
% radiation acoustics.
%
% The script uses 2-dimensional arrays.  The first index is necessary to
% account for multi-line sensor ports with differing diameters and
% properties.  The first row is for the domain or boundary closest to the
% sensor port back, with increasing rows moving towards the opening. The
% second index is necessary to account for frequency-dependent functions,
% with increasing column corresponding to increasing frequency.
%
% Model inputs are in English Engineering (EE) units.
%

%% Initialize
close all
clear

%% Inputs
%%% Geometry inputs
% Line and diameter inputs are needed for the sensor port.  Note that this
% is the physical geometry and does not expect input for the radiation domain.
% Recall the first index is the port line segment closest to the sensor face.
lenLine=    [0.5; 0.5];     % physical length of a line segment - list as a column vector (in)
diamLine=   [0.5; 0.5];     % physical diameter for each line segment - list as a column vector (in)
nlines=length(lenLine);     % number of physical line segments - excludes radiation domain (#)

%%% Property inputs
% The example values are extracted from the COMSOL linearized thermoviscous
% acoustic model for air at T=536.67 degR and P=14.69595 psia.  Note for
% constant properties, multiply by the unit column vector using the 'ones'
% function.  Also, note that sound speed and density need an additional row
% for the ambient conditions outside of the sensor port (used for radiation
% acoustics).
%
% Note for conversions from SI to EE units
% For sound speed:          1 in = 0.0254 m [exact]
% For density:              1 lbm/in^3 = 0.45359237/0.0254^3 kg/m^3 [exact]
% For dynamic viscosity:    1 lbm/(in*s) = 0.45359237/0.0254 Pa*s [exact]
% For thermal conductivity: 1 lbf/(s*degR) = (9/5)*0.45359237*9.80665 W/(m*K) [exact]

c=      13623.65330172398       *ones(nlines+1,1);  % sound speed (in/s)
rho=    0.427791021536526e-4    *ones(nlines+1,1);  % density (lbm/in^3)
mu=     0.102953715010188e-5    *ones(nlines,1);    % dynamic viscosity (lbm/(in*s))
kappa=  0.003267483479579       *ones(nlines,1);    % thermal conductivity (lbf/(s*degR))
Pr=     0.706708267546419       *ones(nlines,1);    % Prandtl # (-)
gamSHR= 1.399375425618002       *ones(nlines,1);    % specific heat ratio (-)

%%% Bandwidth inputs
% Note that the radiation acoustics model uses piston vibration theory.  At
% very high frequencies, the oscillatory flow at the opening is not uniform
% like a vibrating piston and additional error may be present.  It is
% recommended that the maximum frequency does not exceed several harmonics.
fmax=   10000;          % frequency max (Hz)
fres=   0.1;            % frequency resolution (Hz)

%% Constants and Calculations from Inputs
freq=0:fres:fmax;       % frequency variable (Hz)
omega=2*pi*freq;        % angular frequency variable (rad/sec)
kRad=omega/c(end);      % wavenumber variable (rad/in) - for radiation acoustics domain
gc=386.0874;            % conversion constant (lbm*in/(lbf*s^2)) [exact]

%% Exception Handling
% The exception handling ensures fmax does not exceed a value where the 1st
% order Struve function relative error is less than 0.05%.  The power
% series expansion of H1(x), through m=100 terms, maintains this accuracy
```

```matlab
% for x<=30. For higher frequencies (or higher Struve argument x), an
% improved estimate (m>100) of the 1st order Struve function should be
% used. For m=100, the error is within 1e-7% at x=10, 0.000004% at x=20,
% 0.04% at x=30, and drops to 1% at x=33.
xStruve=30;             % Struve function argument - preset based on error analysis (rad)
mStruve=100;            % series truncation order - preset based on error analysis (-)
maxDiamLine=max(diamLine);                        % max line diameter (in)
if fmax>c*xStruve/(2*pi*maxDiamLine)            % test ensuring xStruve>2*kmax*radius
    fmax=floor(c*xStruve/(2*pi*maxDiamLine));   % redefine fmax (Hz)
    disp(['fmax reduced to ', num2str(fmax),' Hz - to preserve Struve function accuracy'])
end

%% End Correction
% The exact end correction is calculated using the 1st Order Struve
% function.  It is represented with a power series expansion.
x=kRad*diamLine(end);       % Struve function argument - uses diameter at opening (rad)
Hnew=0;                     % initialize the series
for m=0:mStruve             % loop to obtain the series expansion
    Hold=(-1)^m/(gamma(m+1.5)*gamma(m+2.5))*(x/2).^(2*m+2);
    Hnew=Hold+Hnew;
end

% End correction
dLeffExact=Hnew./kRad.^2/(diamLine(end)/2);    % exact end correction - a function of frequency (in)
dLeffApprox=4*diamLine(end)/(3*pi);            % approx. end correction - used in plot text (in)

%% Thermoviscous Absorption - Traditional
% Computes traditional thermoviscous absorption coefficients
for n=1:nlines
    alphaMU(n,:)=1/c(n)/(diamLine(n)/2)...              % viscous losses (1/in)
        *sqrt(mu(n)*omega(1,:)/2/rho(n));
    alphaKAPPA(n,:)=1/c(n)/(diamLine(n)/2)...           % thermal losses (1/in)
        *sqrt(mu(n)*omega(1,:)/2/rho(n))...
        *((gamSHR(n)-1)/sqrt(Pr(n)));
    alphaTHERMVISC(n,:)=alphaMU(n,:)+alphaKAPPA(n,:);   % combined losses (1/in)
end

%% Thermoviscous Absorption - Exact
% Computes exact thermoviscous absorption coefficient and propagation constant
for n=1:nlines
    % The exact thermoviscous complex wave number has a sqrt term in the
    % denominator.  This finds the real and imag parts of the sqrt term.
    ConstA(n,:)=2*c(n)*alphaTHERMVISC(n,:)./omega(1,:);         % sqrt term A (-)
    ConstB(n,:)=nthroot((1-ConstA(n,:)).^2+ConstA(n,:).^2,4);   % sqrt term B (-)
    ConstC(n,:)=atan2(ConstA(n,:),1-ConstA(n,:));               % sqrt term C (rad)
    RealS(n,:)=ConstB(n,:).*cos(ConstC(n,:)/2);                 % sqrt real part (-)
    ImagS(n,:)=ConstB(n,:).*sin(ConstC(n,:)/2);                 % sqrt imag part (-)

    % Real and imag parts of the thermoviscous complex wave number
    Rek(n,:)=omega(1,:)/c(n).*(RealS(n,:)...    % thermoviscous complex wave number real part (1/in)
        ./(RealS(n,:).^2+ImagS(n,:).^2));
    Imk(n,:)=-omega(1,:)/c(n).*(ImagS(n,:)...   % thermoviscous complex wave number imag part (1/in)
        ./(RealS(n,:).^2+ImagS(n,:).^2));

    % Components of the thermoviscous propagation constant
    alphaTV(n,:)=-Imk(n,:);                             % thermoviscous spatial absorption coefficient (1/in)
    betaTV(n,:)=Rek(n,:);                               % thermoviscous phase shift parameter (1/in)
    cPhaseTHERMVISC(n,:)=omega(1,:)./betaTV(n,:);       % thermoviscous phase speed (in/s)
    gamPortTHERMVISC(n,:)=alphaTV(n,:)+betaTV(n,:)*i;   % thermoviscous propagation constant (1/in)
end

%% Acoustic Radiation Absorption
% Computes radiation absorption coefficient and propagation constant
alphaRAD=1/2./dLeffExact...                             % radiation absorption coefficient (1/in)
    .*(1-besselj(1,kRad*diamLine(end))...
    ./(kRad*diamLine(end)/2));
%alphaRADApprox=3*diamLine(end)/2*pi/32*omega.^2/c(end)^2;   % approx. radiation absorption coefficient (1/in)
cPhaseRAD=c(end);                                       % radiation phase speed (in/s)
betaRAD=omega/cPhaseRAD;                                % radiation phase shift parameter (1/in)
gamPortRAD=alphaRAD+betaRAD*i;                          % radiation propagation constant (1/in)

%% Characteristic Impedance
% Computes the characteristic impedance for each thermoviscous and
% radiation domain.  Impedance has the form, Z=p/q (pressure-to-volume velocity).
for n=1:nlines
    ZcTHERMVISC(n,:)=gamPortTHERMVISC(n,:)...                               % thermoviscous char. impedance (lbf*s/in^5)
        /(gc/c(n)^2)./(i*omega(1,:))*rho(n)/(pi*diamLine(n)^2/4);
end
ZcRAD=gamPortRAD/(gc/c(end)^2)./(i*omega)*rho(end)/(pi*diamLine(end)^2/4);  % radiation char. impedance (lbf*s/in^5)

%% Multiple Line Sensor Port Response
% Computes the sensor port response for multiple lines using the transfer
% equation framework. Acoustic impedance has the form Z=p/q (pressure-to-volume velocity).
n=nlines+1;     % number of domains (n>=2): n-1 thermoviscous domains and 1 radiation domain
Zc=[ZcTHERMVISC;ZcRAD];                             % characteristic impedance array (lbf*s/in^5)
gam=[alphaTHERMVISC+omega./cPhaseTHERMVISC*i;...        % propagation constant array (1/in)
    alphaRAD+omega/cPhaseRAD*i];
LineLength=[lenLine*ones(1,length(freq));dLeffExact];   % line length array (in)

% This loop obtains the boundary impedances from the sensor face to the
```

```
% boundary downstream of the acoustic radiation domain.  To include a real
% wall impedance, define Z(1,:), remove Z(2,:), and loop from k=2:n+1.
Z(1,:)=inf*ones(1,length(freq));                    % impedance at port back - infinite, boundary node 1 (lbf*s/in^5)
Z(2,:)=-Zc(1,:)./tanh(gam(1,:).*LineLength(1,:));   % impedance at boundary node 2 (lbf*s/in^5)
for k=3:n+1                                         % impedance at boundary node 3 to n+1 (lbf*s/in^5)
    Z(k,:)=(Z(k-1,:)-Zc(k-1,:).*tanh(gam(k-1,:).*LineLength(k-1,:)))...
        ./(1-Z(k-1,:).*tanh(gam(k-1,:).*LineLength(k-1,:))./Zc(k-1,:));
end

% This loop obtains transfer equations across domains, where the boundary
% node k varies from n to 1 by -1. The loop is necessary since transfer
% equations across multiple domains require transfer equations across the
% previous domains.  The transfer equations are estimated across domains
% with field variables specified at boundaries from q(n)/p(n+1) to
% q[1]/p[n+1] and from p[n]/p[n+1] to p[1]/p[n+1].  The sensor port
% response is given as p[1]/p[n+1].
qpn(n,:)=1./Zc(n,:).*sinh(gam(n,:).*LineLength(n,:))...     % transfer equation q[n]/p[n+1] (in^5/(lbf*s))
    +cosh(gam(n,:).*LineLength(n,:))./Z(n+1,:);
ppn(n,:)=cosh(gam(n,:).*LineLength(n,:))...                 % transfer equation p[n]/p[n+1] (-)
    +Zc(n,:)./Z(n+1,:).*sinh(gam(n,:).*LineLength(n,:));
for k=n-1:-1:1                          % transfer equations q[k]/p[n+1] (in^5/lbf-s) and p[k]/p[n+1] (-)
    qpn(k,:)=ppn(k+1,:)./Zc(k,:).*sinh(gam(k,:).*LineLength(k,:))...
        +qpn(k+1,:).*cosh(gam(k,:).*LineLength(k,:));
    ppn(k,:)=ppn(k+1,:).*cosh(gam(k,:).*LineLength(k,:))...
        +qpn(k+1,:).*Zc(k,:).*sinh(gam(k,:).*LineLength(k,:));
end

% Relationship for the pressure at the back (at the sensor face) to the
% pressure in the external environment (outside the port), and vice versa.
% This represents the response at the back of a sensor port relative to the
% response at the wall of a configuration with no sensor port, and vice versa.
pBack_pEnv=ppn(1,:);            % sensor port response function p[1]/p[n+1] (-)
pEnv_pBack=1./ppn(1,:);         % inverse sensor port response function p[n+1]/p[1] (-)

%% Transfer Equations and Inverse Transfer Equations
TF_Gain=abs(pBack_pEnv);                % amplification factor (-)
TF_Ang=angle(pBack_pEnv)*180/pi;        % relative phase (deg)
TF_Inv_Gain=abs(pEnv_pBack);            % inverse amplification factor (-)
TF_Inv_Ang=angle(pEnv_pBack)*180/pi;    % inverse relative phase (deg)

%% Resonance Frequency
% This section finds the peak frequency and natural frequency. To determine
% a search window, an approximate sound speed is first computed and used to
% estimate the resonance frequency.  A tractable search range with a single
% peak occurs in a range less than twice the estimated resonance frequency.
% This search window may not be applicable to complicated systems, and is
% intended for display on plot window.
meanc=sum(LineLength(1:n,2).*c(1:n))/sum(LineLength(1:n,2));    % approximate weighted average sound speed (in/s)
maxRangeIndex=min(floor((1/fres)*meanc/2/sum(lenLine))...       % estimate of the fundamental resonance is in this range (index)
    ,floor((1/fres)*fmax));
[peakVal,peakIndex]=max(abs(pBack_pEnv(1:maxRangeIndex)));      % find value and index - peak freq. (-,index)
fPeak=freq(peakIndex);                                          % peak freq. (Hz)
AmpPeak=abs(pBack_pEnv(peakIndex));                             % max amplification factor - at peak freq. (-)
% Natural frequency
[phaseVal,phaseIndex]=min(abs(angle(pBack_pEnv(1:maxRangeIndex))*180/pi+90)); % find value and index - natural freq. (deg,index)
fNat=freq(phaseIndex);                                          % natural freq. (Hz)
AngleNat=angle(pBack_pEnv(phaseIndex))*180/pi;                  % relative phase - at natural freq. (deg)

%% Plot Transfer Equation
% The settings listed set the default axes font size, figure handle, units
% to pts, figure size, figure name, figure title display, and background
% color
set(0,'defaultaxesfontsize',12)
s1001.fig=figure(1001);
    clf(s1001.fig);
    set(s1001.fig,'Units','points')
    set(s1001.fig,'Position', [300,150,960,540]);
    set(s1001.fig,'Name','Sensor Port Response');
    set(s1001.fig,'NumberTitle','off');
    set(s1001.fig,'Color','white','Inverthardcopy','off');

    % plot and settings for amplification factor
    subplot(2,1,1)
        plot(freq,TF_Gain,'LineWidth',1.5);
        hold on
            plot(fPeak,AmpPeak,'Marker','o');
        hold off
        axis([0 fmax 0 2*max(TF_Gain)])
        xlabel('Frequency (Hz)','FontSize', 14)
        ylabel('Amplification Factor (-)','FontSize', 14)
        title(['\fontsize{20} Sensor Port Response'])
        grid on
        % Replace legend with textbox by retaining legend size/location functionality
        meanDiam=sum(LineLength(1:n,2)...                                   % weighted diam. - for reference (in)
            .*[diamLine;diamLine(end)])/sum(LineLength(1:n,2));
        txtStr={['Total Port Length = ', num2str(sum(lenLine)), ' in'];...          % text string
            ['End Correction (approx.) = ', num2str(dLeffApprox), ' in'];...
            ['Weighted Diameter = ', num2str(meanDiam), ' in'];...
            ['Weighted Sound Speed = ', num2str(meanc/12,'%.0f'), ' ft/s'];...
            ['Num. of Port Line Segments = ', num2str(sum(nlines)) ]};
```

```matlab
        [val,ind]=max(strlength(txtStr));                                          % retain longest string for sizing legend
        hLeg=legend(txtStr(ind),'FontSize',11);                                   % legend based on longest string
        hTB=annotation('textbox','String',txtStr,'LineStyle','None','FontSize',11); % annotation box
        hTB.Position=hLeg.Position;                                               % use the legend size/position
        delete(hLeg);                                                             % remove legend
        % create arrow and annotation if there is space
        if fmax>1.5*fPeak
            pos=get(gca,'Position');
            ArwTail=[1.3*fPeak 1.3*AmpPeak];
            ArwTip=[fPeak AmpPeak];
            annotation('textarrow',...
                [(ArwTail(1)-min(xlim))/diff(xlim)*pos(3)+pos(1),...
                (ArwTip(1)-min(xlim))/diff(xlim)*pos(3)+pos(1)],...
                [(ArwTail(2)-min(ylim))/diff(ylim)*pos(4)+pos(2),...
                (ArwTip(2)-min(ylim))/diff(ylim)*pos(4)+pos(2)],...
                'String',{['$f_{pk} = $',num2str(fPeak,'%.0f'),'$ Hz$']...
                ,['$A = $',num2str(AmpPeak,'%.1f'),'$\times$']}...
                ,'horizontalalignment','left','FontSize',15,'Interpreter','latex');
        end

    % plot and settings for relative phase
    subplot(2,1,2)
        plot(freq,TF_Ang,'LineWidth',1.5);
        hold on
            plot(fNat,AngleNat,'Marker','o');
        hold off
        axis([0 fmax -200 200])
        xlabel('Frequency (Hz)','FontSize', 14)
        ylabel('Phase (deg)','FontSize', 14)
        grid on
        % create arrow and annotation if there is space
        if fmax>1.5*fPeak
            pos=get(gca,'Position');
            ArwTail=[1.3*fNat 0];
            ArwTip=[fNat AngleNat];
            annotation('textarrow',...
                [(ArwTail(1)-min(xlim))/diff(xlim)*pos(3)+pos(1),...
                (ArwTip(1)-min(xlim))/diff(xlim)*pos(3)+pos(1)],...
                [(ArwTail(2)-min(ylim))/diff(ylim)*pos(4)+pos(2),...
                (ArwTip(2)-min(ylim))/diff(ylim)*pos(4)+pos(2)],...
                'String',{['$f_{n} = $',num2str(fNat,'%.0f'),'$ Hz$']...
                ,['$\phi = $',num2str(AngleNat,'%.0f'),'$^{\circ}$']}...
                ,'horizontalalignment','left','FontSize',15,'Interpreter','latex');
        end

%% Plot Inverse Transfer Equation
% % The settings listed set the default axes font size, figure handle, units
% % to pts, figure size, figure name, figure title display, and background
% % color
% set(0,'defaultaxesfontsize',12)
% s2001.fig=figure(2001);
%     clf(s2001.fig);
%     set(s2001.fig,'Units','points')
%     set(s2001.fig,'Position', [400,100,960,540]);
%     set(s2001.fig,'Name','Inverse Sensor Port Response');
%     set(s2001.fig,'NumberTitle','off');
%     set(s2001.fig,'Color','white','Inverthardcopy','off');
%
%     subplot(2,1,1)          % plot and settings for inverse amplification factor
%         plot(freq,TF_Inv_Gain,'LineWidth',1.5);
%         axis([0 fmax 0 2*max(TF_Inv_Gain)])
%         xlabel('Frequency (Hz)','FontSize', 14)
%         ylabel('Amplification Factor (-)','FontSize', 14)
%         title('Inverse Sensor Port Response','FontSize', 20)
%         grid on
%     subplot(2,1,2)          % plot and settings for inverse relative phase
%         plot(freq,TF_Inv_Ang,'LineWidth',1.5);
%         axis([0 fmax -200 200])
%         xlabel('Frequency (Hz)','FontSize', 14)
%         ylabel('Phase (deg)','FontSize', 14)
%         grid on
```

REFERENCES

1. Blackstock, D.T.: *Fundamentals of Physical Acoustics*, John Wiley & Sons, Inc., New York, 2000.

2. Kinsler, L.E.; Frey, A.R.; Coppens, A.B.; and Sanders, J.V.: *Fundamentals of Acoustics*, John Wiley & Sons, Inc., New York, 2000.

3. Blevins, R.D.: *Formulas for Natural Frequency and Mode Shape*, Krieger Publishing Company, Malabar, FL, 2001.

4. Morse, P.M.; and Ingard, K.U.: *Theoretical Acoustics*, McGraw-Hill, Inc., New York, NY, 1968.

5. Harrje, D.T.; and Reardon, F.H.: "Liquid Propellant Rocket Combustion Instability," NASA-SP-194, NASA Headquarters, Washington, DC, 1972.

6. Thomas, J.P.; and Layton, J.P.: "Final Summary Technical Report on Transient Pressure Measuring Methods Research," AMS Report No. 595t, Guggenheim Laboratories for the Aerospace Propulsion Sciences, Princeton University, 1967.

7. Wylie, E.B.; and Streeter, V.L.: *Fluid Transients in Systems*, Prentice-Hall, Inc., Upper Saddle River, NJ, 1993.

8. Tijdeman, H.: "On the Propagation of Sound Waves in Cylindrical Tubes," *Journal of Sound and Vibration*, Vol. 39, Issue 1, pp. 1–33, March 8, 1975.

9. Casiano, M.J.; and Zoladz, T.F.: "Theoretical Consolidation of Acoustic Dissipation," NASA/TM—2012–217455, NASA Marshall Space Flight Center, Huntsville, AL, 2012.

10. Munjal, M.L.: *Acoustics of Ducts and Mufflers*, John Wiley & Sons, New York, 1987.

11. COMSOL Multiphysics®, "Acoustics Module User's Guide," version 5.4. COMSOL, Inc., <www.comsol.com>.

12. "Maple 2019," Maplesoft, a division of Waterloo Maple Inc., Waterloo, Ontario, 1981–2019.

13. Kinsler, L.E.; and Frey, A.R.: *Fundamentals of Acoustics*, 2nd ed., John Wiley & Sons, Inc., New York, 1962.

14. Pierce, A.D.: *Acoustics*: *An Introduction to its Physical Principles and Applications*, McGraw-Hill Book Company, New York, 1981.

15. Aarts, R.M.; and Janssen, A.J.E.M.: "Approximation of the Struve function H_1 occuring in impedance calculations," *The Journal of the Acoustical Society of America*, Vol. 113, Issue 5, pp. 2635–2637, May 2003.

16. Aarts, R.M.; and Janssen, A.J.E.M.: "Efficient approximation of the Struve functions H_n occurring in the calculation of sound radiation quantities," *The Journal of the Acoustical Society of America*, Vol. 140, Issue 6, pp. 4154–4160, December 2016.

17. COMSOL Multiphysics®, "Reference Manual," version 5.4, COMSOL, Inc., <www.comsol.com>.

18. Foote, K.G.: "Discriminating between the nearfield and farfield of acoustic transducers," *The Journal of the Acoustical Society of America*, Vol. 136, Issue 4, pp. 1511–1517, October 2014.

19. Bird, R.B.; Stewart, W.E.; and Lightfoot, E.N.: *Transport Phenomena,* Revised 2nd ed., John Wiley & Sons, Inc., New York, 2007.

20. Lemmon, E.W.; Huber, M.L.; and McLinden, M.O.: "NIST Standard Reference Database 23: Reference Fluid Thermodynamic and Transport Properties-REFPROP, Version 9.1," May 7, 2013.

21. Searby, G.; Nicole, A.; Habiballah, M.; and Laroche, E.: "Prediction of the Efficiency of Acoustic Damping Cavities," *Journal of Propulsion and Power*, Vol. 24, No. 3, pp. 516–523, May 2008.

22. Hamilton, M.F.; and Blackstock, D.T. (eds.): *Nonlinear Acoustics*, Academic Press, San Diego, CA, 1998.

23. Anderson, J.D.: *Modern Compressible Flow With Historical Perspective*, McGraw-Hill, Boston, 2003.

24. Oppenheim, A.V.; and Schafer, R.W.: *Discrete-Time Signal Processing*, 2nd ed., Prentice-Hall, Inc., Upper Saddle River, 1999.

25. "PC-Signal®," AI Signal Research, Inc, Huntsville, AL, 1993–2019.

26. Bendat, J.S.; and Piersol, A.G.: *Engineering Applications of Correlation and Spectral Analysis*, John Wiley & Sons, Inc., New York, 1993.

27. Casiano, M.J.: "Acoustic Analysis of Sensor Ports," 2019 JANNAF Meeting/11th Liquid Propulsion Subcommittee Meeting, Tampa, FL, December 9–13, 2019.

28. Casiano, M.J.: "Extensions to the Time Lag Models for Practical Application to Rocket Engine Stability Design," Dissertation, Mechanical Engineering, Doctor of Philosophy, The Pennsylvania State University, State College, PA, August 2010.

29. Meisenholder, S.G.; and Bickford, L.L.: "Pogo Analysis of the Saturn Propulsion System," AMDR 9635-037, Aerojet-General Corporation, Sacramento, CA, 1967.

30. Dalmont, J.P.; Nederveen, C.J.; and Joly, N.: "Radiation Impedance of Tubes with Different Flanges: Numerical and Experimental Investigations," *Journal of Sound and Vibration*, Vol. 244, Issue 3, pp. 505–534, July 12, 2001.

31. Silva, F.; Guillemain, P.; Kergomard, J.; et al.: "Approximation Formulae for the Acoustic Radiation Impedance of a Cylindrical Pipe," *Journal of Sound and Vibration*, Vol. 322, Issues 1–2, pp. 255–263, April 2009.

32. Panton, R.L.: *Incompressible Flow*, 2nd ed., John Wiley & Sons, Inc., New York, 1996.

33. Bejan, A.: *Convection Heat Transfer*, John Wiley & Sons, Inc., New York, 1995.

34. Kundu, P.K.; and Cohen, I.M.: *Fluid Mechanics*, 3rd ed., Elsevier Academic Press, London, 2004.

35. Bejan, A.: *Advanced Engineering Thermodynamics*, 2nd ed., John Wiley & Sons, Inc., New York, 1997.

36. Jong, J.; Coffin, T.; Jones, J.H.; et al.: "Correlation Identification between Spectral Components in Turbomachinery Measurements by Generalized Hypercoherence," in *Proceedings, 3rd International Machinery Monitoring and Diagnostic Conference*, Las Vegas, NV, December 9–12, 1991, pp. 243–248, 1991.

37. Thomas, J.B.: *An Introduction to Statistical Communication Theory*, John Wiley & Sons, Inc., New York, 1969.

38. Grossman, S.I.: *Calculus*, 5th ed., Saunders College Publishing, Fort Worth, 1992.

39. Moore, R.K.: *Traveling-Wave Engineering*, McGraw-Hill Book Company, Inc., New York, 1960.

40. Beranek, L.L.; and Mellow, T.J.: *Acoustics: Sound Fields and Transducers*, Elsevier Inc.-Academic Press, Oxford, UK, 2012.

REPORT DOCUMENTATION PAGE	*Form Approved* *OMB No. 0704-0188*

1. REPORT DATE *(DD-MM-YYYY)*
01–05–2021

2. REPORT TYPE
Technical Publication

3. DATES COVERED *(From - To)*

4. TITLE AND SUBTITLE
Analytical and Numerical Modeling of Sensor Port Acoustics

5a. CONTRACT NUMBER

5b. GRANT NUMBER

5c. PROGRAM ELEMENT NUMBER

6. AUTHOR(S)
M.J. Casiano and S.R. Fischbach, Editor

5d. PROJECT NUMBER

5e. TASK NUMBER

5f. WORK UNIT NUMBER

7. PERFORMING ORGANIZATION NAME(S) AND ADDRESS(ES)
George C. Marshall Space Flight Center
Huntsville, AL 35812

8. PERFORMING ORGANIZATION REPORT NUMBER
M–1515

9. SPONSORING/MONITORING AGENCY NAME(S) AND ADDRESS(ES)
National Aeronautics and Space Administration
Washington, DC 20546–0001

10. SPONSORING/MONITOR'S ACRONYM(S)
NASA

11. SPONSORING/MONITORING REPORT NUMBER
NASA/TP–20210000024

12. DISTRIBUTION/AVAILABILITY STATEMENT
Unclassified-Unlimited
Subject Category 71
Availability: NASA STI Information Desk (757–864–9658)

13. SUPPLEMENTARY NOTES
Prepared by the Propulsion, Structural, Thermal and Fluid Analysis Division, Engineering Directorate

14. ABSTRACT
The purpose of this Technical Publication (TP) is to provide background, relevant theory, and examples for acoustic response analysis of a sensor port. A new approach is devised theoretically and computationally that captures the true acoustic response of a sensor port. This TP summarizes the acoustics background, the port response theoretical development, and provides comparisons of a port acoustic response using an analytical model and computational acoustics. The effects of nonlinear acoustics and acoustic propagation in liquids is also examined. Additionally, this TP describes the design of a specialized filter using the predicted sensor port response that can be applied to data for correction.

15. SUBJECT TERMS
sensor port, sensor port acoustics, sensor port resonance, sensor port design, sensor port frequency response, sensor port analytic modeling, sensor port numerical modeling, sensor standoff, sensor offset, sensor recess

16. SECURITY CLASSIFICATION OF:			17. LIMITATION OF ABSTRACT	18. NUMBER OF PAGES	19a. NAME OF RESPONSIBLE PERSON
a. REPORT	b. ABSTRACT	c. THIS PAGE			STI Help Desk at email: help@sti.nasa.gov
U	U	U	UU	142	19b. TELEPHONE NUMBER *(Include area code)* STI Help Desk at: 757–864–9658

Standard Form 298 (Rev. 8-98)
Prescribed by ANSI Std. Z39-18

National Aeronautics and
Space Administration
IS02
George C. Marshall Space Flight Center
Huntsville, Alabama 35812